Summer 2012

Development and characterization of a finite element model of lung motion

Ryan Amelon
University of Iowa

DEVELOPMENT AND CHARACTERIZATION OF A FINITE ELEMENT MODEL OF LUNG MOTION

by

Ryan E. Amelon

An Abstract

Of a thesis submitted in partial fulfillment
of the requirements for the Doctor of
Philosophy degree in Biomedical Engineering
in the Graduate College of
The University of Iowa

July 2012

Thesis Supervisor: Professor Madhavan L. Raghavan

ABSTRACT

BACKGROUND: Finite element models of lung motion can aid in understanding mechanically driven lung deformation. Current finite element models consider each lung half as a continuum, lacking the ability to capture the displacement discontinuity at fissures caused by lobe sliding.

OBJECTIVE: The objective of this work was to develop and evaluate finite element models for simulating lung motion that incorporate the role of sliding at the lobe boundaries.

METHODS: Finite element models were developed from 4DCT of tidal breathing from five cancer subjects. To allow sliding, the lobes were modeled as independent bodies within a pleural cavity shell. Pleural cavity deformation was obtained from deformable image registration of the lung segmentations. Contact between the pleural cavity and lobes prevented penetration and allowed sliding at all interfaces. Lung parenchyma was modeled as a homogeneous, 2-parameter, Neo-Hookean finite elastic model. The parameters of the Neo-Hookean model, C1 and D1, were optimized by perturbation within realistic reported ranges; defined by the equivalent infinitesimal elasticity parameters: Young's modulus (from 0.7 kPa to 70 kPa) and ν (from 0.2 to 0.49). The frictional coefficient at fissures was perturbed between 0 (free sliding) and 1.5 (no sliding). 1,960 finite element analyses were performed across the five subjects. The optimal parameter ranges were evaluated by average landmark error and percentage of converged solutions.

The developed finite element method, using optimized material and friction parameters, was further evaluated in a data set of six healthy subjects with image pairs spanning functional residual capacity (FRC) to total lung capacity (TLC). The finite element predicted displacement field for lobe sliding finite element models and

continuum-based finite element models were compared using average landmark error and correlation with the lobe-by-lobe deformable image registration results.

RESULTS AND DISCUSSION: The optimal parameters for Young's modulus were 49 kPa to 70 kPa and Poisson's ratio were 0.2 to 0.4. Variation of inter-lobar frictional coefficients did change displacement field accuracy assessed by landmark error or correlation to lobe-by-lobe deformable image registration. Characteristics of sliding predicted by the lobe sliding finite element models were consistent with characteristics in sliding observed in deformable image registration results. Also, variations in regional ventilation, quantified at the lobe level, were predicted by the finite element models and were shown to be influenced by the amount of lobe sliding allowed by the models.

Abstract Approved: _____
Thesis Supervisor

_____
Title and Department

_____
Date

DEVELOPMENT AND CHARACTERIZATION OF A FINITE ELEMENT MODEL OF LUNG MOTION

by

Ryan E. Amelon

A thesis submitted in partial fulfillment
of the requirements for the Doctor of
Philosophy degree in Biomedical Engineering
in the Graduate College of
The University of Iowa

July 2012

Thesis Supervisor: Professor Madhavan L. Raghavan

Graduate College
The University of Iowa
Iowa City, Iowa

CERTIFICATE OF APPROVAL

_____

PH.D. THESIS

_____

This is to certify that the Ph.D. thesis of

Ryan E. Amelon

has been approved by the Examining Committee
for the thesis requirement for the Doctor of Philosophy
degree in Biomedical Engineering at the July 2012 graduation.

Thesis Committee: _____
Madhavan L. Raghavan, Thesis Supervisor

_____
Joseph Reinhardt

_____
Gary Christensen

_____
John Bayouth

_____
Jia Lu

To Mom, Dad and Emma

ACKNOWLEDGMENTS

I would like to thank my advisor Madhavan Raghavan for his guidance throughout my graduate studies. His support in this research project was vital. But what I most appreciate is the time he spent shaping me as a researcher and as a person. He has been a great advisor and a good friend. And for that I am thankful.

I would like to thank Joseph Reinhardt for his support and funding for my graduate work. His insights, guidance and critical evaluation of my work shaped the way I think about and conduct research for the better.

Kai Ding and Kunlin Cao provided the foundation for which this work was based. I would like to thank both of them for their hard work and support.

I would like to thank all my committee members: Gary Christensen, Jia Lu and John Bayouth. Their input was vital to shaping the success of this project.

I would like to thank all the members of the BioMOST lab at the University of Iowa.

And finally, I would like to thank the funding source for this work: NIH grant HL079406.

ABSTRACT

BACKGROUND: Finite element models of lung motion can aid in understanding mechanically driven lung deformation. Current finite element models consider each lung half as a continuum, lacking the ability to capture the displacement discontinuity at fissures caused by lobe sliding.

OBJECTIVE: The objective of this work was to develop and evaluate finite element models for simulating lung motion that incorporate the role of sliding at the lobe boundaries.

METHODS: Finite element models were developed from 4DCT of tidal breathing from five cancer subjects. To allow sliding, the lobes were modeled as independent bodies within a pleural cavity shell. Pleural cavity deformation was obtained from deformable image registration of the lung segmentations. Contact between the pleural cavity and lobes prevented penetration and allowed sliding at all interfaces. Lung parenchyma was modeled as a homogeneous, 2-parameter, Neo-Hookean finite elastic model. The parameters of the Neo-Hookean model, C1 and D1, were optimized by perturbation within realistic reported ranges; defined by the equivalent infinitesimal elasticity parameters: Young's modulus (from 0.7 kPa to 70 kPa) and ν (from 0.2 to 0.49). The frictional coefficient at fissures was perturbed between 0 (free sliding) and 1.5 (no sliding). 1,960 finite element analyses were performed across the five subjects. The optimal parameter ranges were evaluated by average landmark error and percentage of converged solutions.

The developed finite element method, using optimized material and friction parameters, was further evaluated in a data set of six healthy subjects with image pairs spanning functional residual capacity (FRC) to total lung capacity (TLC). The finite element predicted displacement field for lobe sliding finite element models and

continuum-based finite element models were compared using average landmark error and correlation with the lobe-by-lobe deformable image registration results.

RESULTS AND DISCUSSION: The optimal parameters for Young's modulus were 49 kPa to 70 kPa and Poisson's ratio were 0.2 to 0.4. Variation of inter-lobar frictional coefficients did change displacement field accuracy assessed by landmark error or correlation to lobe-by-lobe deformable image registration. Characteristics of sliding predicted by the lobe sliding finite element models were consistent with characteristics in sliding observed in deformable image registration results. Also, variations in regional ventilation, quantified at the lobe level, were predicted by the finite element models and were shown to be influenced by the amount of lobe sliding allowed by the models.

TABLE OF CONTENTS

LIST OF TABLES

LIST OF FIGURES

CHAPTER 1: BACKGROUND

1.1 Anatomy and Mechanics

The lung is divided into two halves, the right and left lungs, situated in thorax on either side of the heart. The trachea descends from the mouth and branches into the two main bronchi to supply air to either half of the lung. The pulmonary artery, coming from the heart, supplies blood for gas exchange. The lung itself is fine network of blood vessels and airways branching to around 23 generations [1]. A fibrous network of collagen and elastin comprise the interstitial portions of the lung and provide structural support. Bulk lung tissue, termed parenchyma, is the collection of minor airways, blood vessels and the underlying fibrous construct. For the purpose of this research 'parenchyma' and 'lung tissue' are synonymous.

Surrounding the lung is an airtight membrane called the pleural cavity. The pleural cavity is bordered by the chest wall on the sides and the diaphragm on the bottom. The space between the lung surface and the pleural cavity surface is termed the intrapleural space and is 5-25 μm wide [2]. This space contains pleural fluid which facilitates near frictionless sliding at this boundary. Negative pressure breathing (natural breathing) initiates when the diaphragm and chest wall move away from the lung, which enlarges the pleural cavity creating a net negative pressure on the lung surface. The negative pressure expands lung volume, dropping the internal pressure, allowing air to passively enter the lung. The negative pressure formed at the boundary of the lung surface is called the pleural pressure. There have been many attempts to characterize pleural pressure acting on the lung surface and it has been concluded that the pleural pressure during breathing has a gravitational dependence, possibly not in equilibrium, rendering modeling difficult [2, 3]. The pleural cavity boundary is well defined in CT images due to the high contrast between the lung and the surrounding soft tissue.

The two lung halves are subdivided into lobes with two lobes comprising the left lung and three lobes comprising the right lung. In the left lung an oblique fissure separates the upper and lower lobes. In the right lung an oblique fissure separates the upper and lower lobes while a

horizontal fissure separates the upper lobe from the middle lobe. The lobes are physically independent structures with independent airways and blood vessels. The internal structures converge at the two main bronchi and pulmonary artery/vein. During breathing the lobes slide relative to each other with maximum sliding on the order of 20mm; see Section 2.2 [4, 5].

There have been a variety of phenomenological discoveries concerning lung function. The lung has a non-linear pressure-volume relationship, Figure 1, indicating that the lung gets stiffer as it inflates [1]. This supports the notion that parenchymal material properties are also non-linear; further discussion in Section 1.3. There is a gravitational dependence to ventilation; i.e. more ventilation in regions closer to Earth's center [1]. Gravitational dependence may be partially attributed to the weight of the lung changing the internal pressure characteristics putting each region of the lung at a different point on the non-linear pressure-volume (P-V) curve, Figure 1. Hysteresis in the P-V curve, illustrated by different inhalation and exhalation paths, indicates that the lung is viscoelastic. This indicates that the lung deforms differently at different inflation rates. Additionally, the rate of inspiration during natural breathing is much different than the rate of expiration, Figure 2. During natural breathing inhale occurs at a slower, steadier rate while exhale occurs rapidly. There is a dead period between breaths where very little air enters or exits the lung. Rate dependent properties could become an important error source when concerned with dynamic image scans.

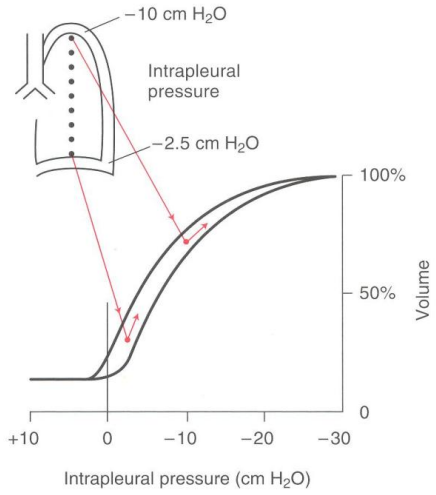

Figure 1 An idealized pressure-volume curve highlights that lung tissue is more compliant at lower volumes and pressures. Gravitational dependence explains the phenomenon that volume change in lower lung regions are at a lower intrapleural pressure compared to the upper lung and thus undergo more volume change. Image adopted from [1]

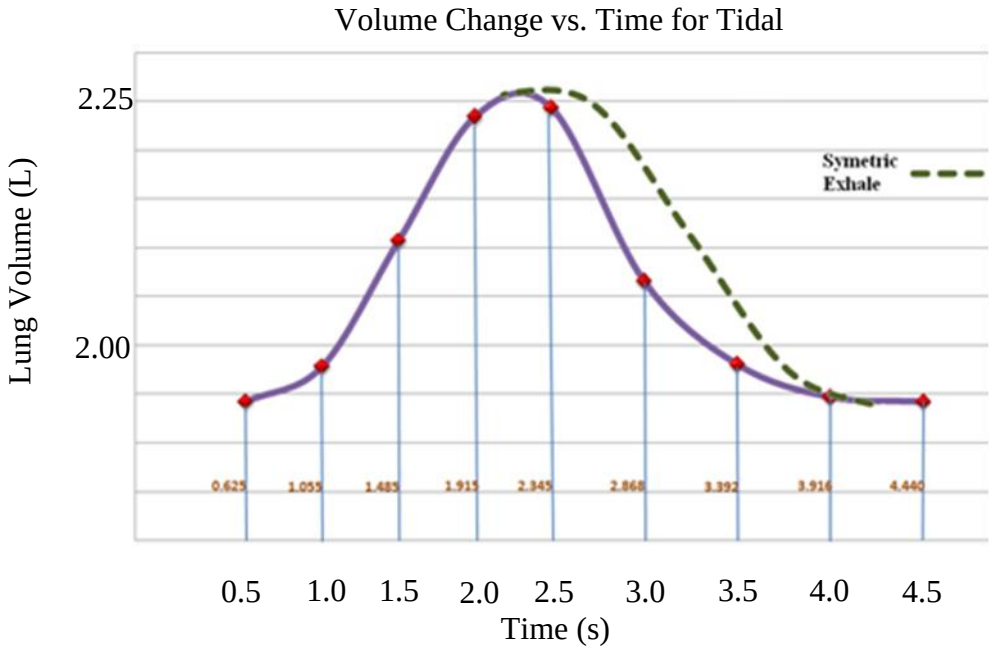

Figure 2 Idealized lung volume as a function of time for human tidal breathing.

1.2 Material Property Estimation of Parenchyma

Research has long sought material properties of lung tissue. Uniaxial extension/compression, biaxial extension and indentation tests have all been used to obtain material models. Lai-Fook *et al.* conducted uniaxial compression tests on entire excised dog lobes under the assumption of linearized elasticity [6]. They found the Young's modulus was about 1.5x internal pressure. Lai-Fook later conducted another uniaxial compression test on a 3x3x3 cm cube of lung parenchyma [7]. Young's modulus from this test ranged from 10 to 40 cmH_2O. Debes conducted uniaxial and biaxial extension tests on thin squares of lung parenchyma (roughly 4.2x4.2x0.36 mm) [8]. A linear stress/strain relationship with Young's modulus of about 20 cmH_2O was found for strains up to 0.25. Salerno *et al.* conducted uniaxial extension testing on guinea pig parenchyma [9]. A nonlinear stress/strain relationship was found, but the nonlinearity only manifested for strains exceeding 0.4.

Indentation tests have also been used to determine lung tissue properties. Lai-Fook was able to estimate an E and v from indentation tests and found results similar to their previous uniaxial tests (Poisson's ratio between 0.38 and 0.48 depending on internal pressure) [6].

Zeng et al. conducted biaxial tests on human lung specimen (3x3x0.4 cm) and found a clear nonlinear stress/strain behavior [10]. They fit the data to a Fung-type anisotropic and isotropic model. Naturally, the anisotropic model fit the data more accurately, but in many instances the isotropic model fit very well. Inspection of the stress/strain curve suggests that a linear model may fit well for strains under 0.4.

A variety of material models have been used for FEM lung applications. Werner *et al.* summarized reported E and v values from several groups, Table 1. E varied from 0.1 to 7.8 kPa and v varied from 0.2 to 0.45. Hyperelastic material properties have also been reported for use in lung FEM which further increases material property variability. Section 1.6 covers the significance of different material properties for lung FEM.

Table 1: Literature values of elasticity modulus and Poisson's ratio for lung tissue when modeling the lungs to be linearly elastic, homogenous, and isotropic.

Reference	Elasticity modulus E (kPa)	Poisson's ratio ν
Al-Mayah *et al.* [11]	7.8	0.43
Brock *et al.* [12]	5.0	0.45
De Wilde *et al.* [13]	0.73	0.3
Sundaram and Gee [14]	0.1	0.2
Villard *et al.* [15]	0.823	0.25–0.35
West and Mathews [16]	0.25	0.3
Zhang *et al.* [17]	4.0	0.35

Inverse finite element analysis has also been proposed to obtain an optimized hyperelastic material model for lung tissue obtained through the indentation test [18, 19]. Inverse finite element modeling is the process of duplicating a physical experiment using a finite element model in order to optimize the material parameters of the model to closely match the results of the physical experiment. Naini *et al.* demonstrated a fairly linear stress-strain relationship for strains under 0.2 [18]. Schwenninger *et al.* performed a similar test using an endoscope to apply a suction pressure inside the lung of a rat. The results were fit to a Neo-Hookean model with an optimized shear modulus of 4.25 kPa [19].

1.3 Lung Image Acquisition

Analysis of lung function is transitioning to regional measures with improvements in imaging and image processing. Lung imaging leverages improvements primarily in CT and MRI. CT scans have improved to a resolution of approximately 0.5 mm^3. CT images provide density information quantified by Hounsfield units (intensity of a voxel). CT scans reveal high contrast within the lung images due to the majority of volume occupied by air, differentiating it from internal blood and surrounding soft tissues, Figure 3. There are two main strategies for acquiring CT lung images. Static lung images are acquired during breath holds near total lung capacity (TLC) and functional residual capacity (FRC). TLC is when the subject forcibly inhales as much

air as possible. FRC is when the subject naturally exhales. TLC volume is generally 2-3 times more than FRC volume. Breath hold scans have high image quality because the lung is not moving during image acquisition. Dynamic CT scans (4DCT) are acquired while the subject is breathing. The scan is acquired over several breaths and the image at any time point can be retrospectively reconstructed. Typically end-inspiration (EI) and end-exhalation (EE) are the most reliable reconstruction points. EI volume is typically 1.2 times that of EE volume. These images tend to be less reliable as the lung is moving during acquisition and the final image is a combination of images acquired over several breaths, which need not fit together perfectly. Image processing techniques are used to improve the final output images. This dissertation uses static CT and 4DCT scans. Other image acquisition modes are possible and provide a basis to compare results, the two most applicable being Xenon-CT and MRI grid tagging.

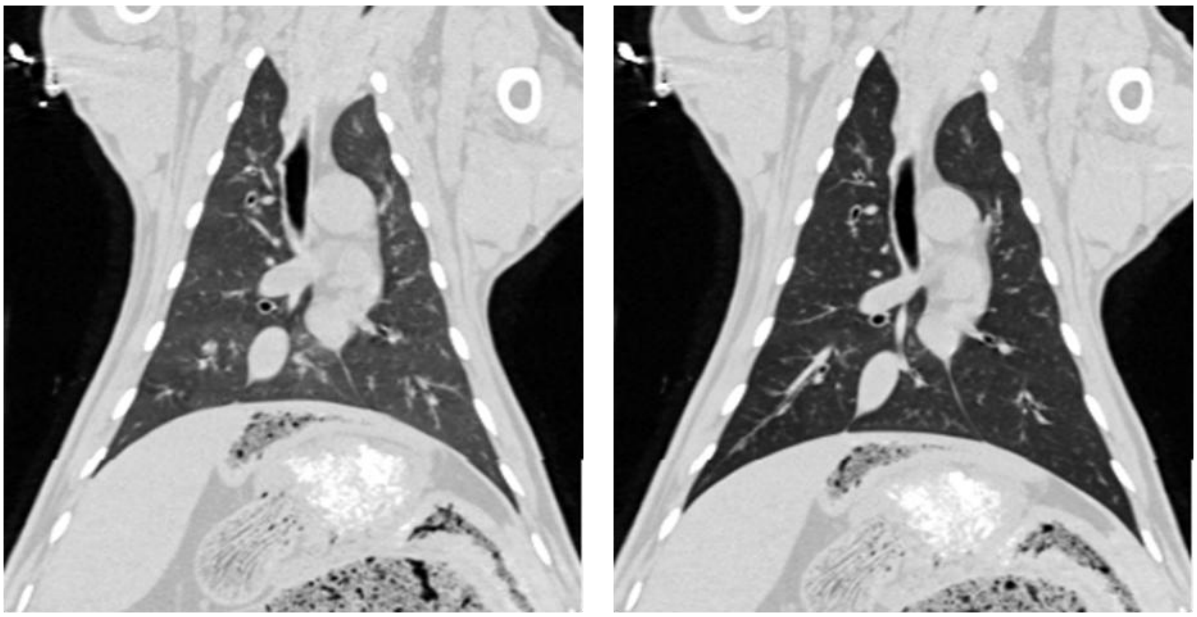

Figure 3: Sample CT scans for a lung at two different lung volumes.

Xenon CT is functional imaging form that shows ventilation distribution of inhaled Xenon gas. This technique measures the density change as the Xenon washes into and out of the lung. The end result is a ventilation map using a gas roughly 5x more dense than air. However, this technique is one of the only methods for acquiring experimental ventilation maps.

MRI grid tagging is a method of inhaling a hyperpolarized gas, such as He^3, and applying a radio induced grid [20], or the grid can be applied using spin inversion [21]. The grid can be tracked for one breathing cycle before the integrity breaks down. The result is a displacement value for each grid point. Methods are currently being developed to track 3D lung motion using MRI grid tagging [20-22]. MRI grid tagging is currently held back by poorer resolution compared to CT, but may serve as an important tool in future lung research. MRI grid tagging directly measures displacement of pockets of air, making it one of the only experimental methods for directly capturing displacement field data.

1.4 Image-based deformable image registration (DIR)

Image-based DIR, typically referred to simply as 'image registration', is an image processing tool for estimating voxel displacements between two images. Registration algorithms map one image space (moving image) to a corresponding image (target image). The general process is summarized in Figure 4. The transform deforms the moving image and the cost function evaluates the appropriateness of the point-to-point matching. The optimizer updates the transform based on the cost function. The process iterates until a minimum cost is achieved. Most progress in adapting image-based DIR to the lung is modification of the cost function. The two most common cost functions are sum of squared intensity difference (SSD) and mutual information (MI). SSD quantifies the intensity difference between corresponding points in the two images. MI attempts to achieve a 1:1 mapping of intensities between the two images. While both can be applied for lung registration, they are fundamentally flawed for application to the lung. The density of the lung changes when the lung changes in volume, Figure 3, rendering SSD inappropriate. Also, ventilation is not homogeneous indicating that intensity change is not

consistent throughout the lung. This renders MI inappropriate. A novel cost function was proposed by Yin *et al.* and is used by our group for lung registration called sum of squared tissue volume difference (SSTVD) [23]. SSTVD assumes that the change in density is due entirely to air entering the lung. Therefore, the intensity (density) of the points in the moving image can be adjusted to account for the density change due to air according to the local Jacobian of the transformation. The Jacobian of the transformation measures the volume change at the given voxel using the displacement field. A SSD comparison between the Jacobian-modified intensities and the target image is then used for cost analysis.

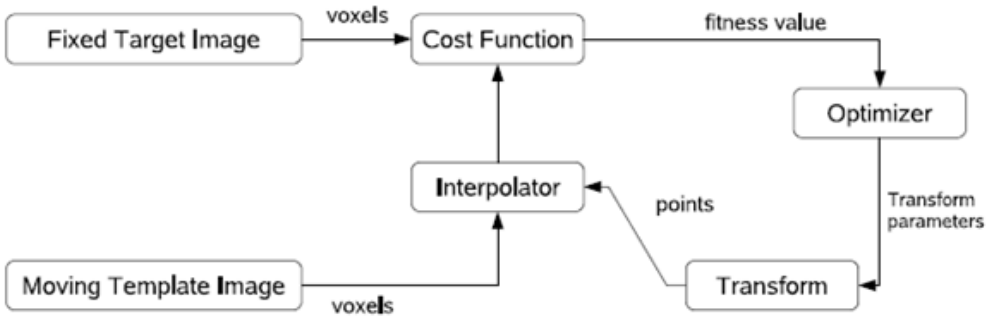

Figure 4: The basic components of the registration framework are two input images, a transform, a cost function, an interpolator and an optimizer.

Registration accuracy depends upon several factors including image quality, volume change between image pairs and error checking method. Typically registration accuracy is assessed using landmark error. Landmark error assessment is the process of identifying trackable landmarks and comparing the measured landmark displacement to the algorithm estimated displacement, see Figure 5. Typical landmark error for DIR are between 1.1 and 3.0 mm as reported by Brock *et al.* in a multi-institutional study [24]. This study was conducted using 4DCT scans of human lungs. Cao *et al.* reported landmark errors on the order of 1 mm using SSTVD on static scans [25]. It is difficult to compare registration algorithms across studies

considering static scans are of higher quality (easier registration) but have a greater volume change (more difficult registration). Landmark error has a couple limitations. First, vessel branch points are only identifiable in image to the 5^{th}-6^{th} generation. Therefore, the most reliable landmarks tend to be centrally located. Secondly, DIR leverages image contrast (landmarks being the main source of contrast in the lung) likely making landmark error a best-case error evaluation.

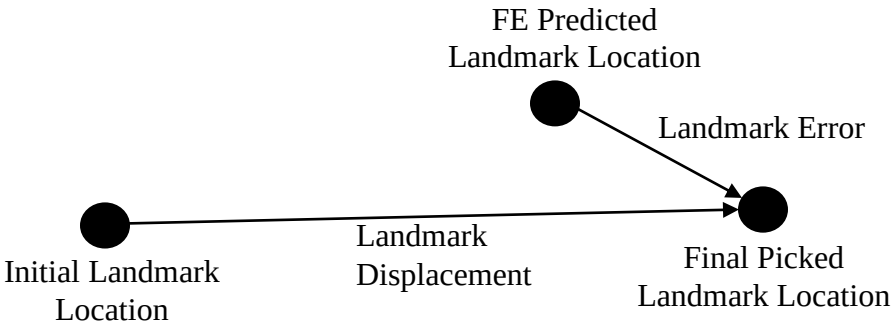

Figure 5. Illustration of landmark error and landmark displacement

Raw image-based DIR tend to be fairly noisy. For this reason smoothing of the displacement field, or the penalizing of radical shear deformations within the cost function, is used to provide a more controlled, uniform deformation field. This is likely a good assumption so long as a discontinuity does not exist within regions undergoing smoothing. However, this is precisely the case at the fissures in the lung. The lobes are known to slide relative to each other resulting in a discontinuity in the displacement field at the fissures. A couple groups have acknowledged this issue in their registration algorithms [4, 26]. Preliminary work analyzing lobe sliding and its effect on DIR are addressed in Section 2.2.

1.5 Physics-based DIR (FEM)

FEM, sometimes referred to as physics-based DIR, leverages our understanding about the mechanical nature and physics surrounding the body of interest to model what we observe. FEM is different from DIR in that FEM models the deformation which allows manipulation of the input parameters to predict motion under a variety of scenarios. The basic process involves discretization of the bodies of interest using a finite element mesh, application of material properties (stiffness) and application of boundary conditions (forces, constraints or contacts). Briefly, FEM then solves equilibrium equations for the discretized mesh based on the applied boundary conditions and underlying material properties.

State-of-the-art finite element (FE) lung models all follow a similar theme. Villard [15], Zhang [17] and Werner [27] discretize the EE volume as a continuous solid and the boundary of the EI volume as a shell. Uniform expanding pressures are applied to the surface of the EE solid with a contact constraint preventing the solid from penetrating the limiting EI shell. The EE solid deforms into a geometry similar to the EI geometry using physiologically reasonable boundary conditions (essentially leveraging an approximation of pleural pressure). Al-Mayah *et al.* takes the opposite approach by discretizing the EI volume as a continuous solid and the boundary of the EI volume as a shell [11]. Contact constraints prevent the solid from penetrating the shell. Displacements are defined on the shell to deform the underlying solid into an approximation of the EE geometry. Pleural pressure itself is not defined, but calculated during the FE process based on displacement boundary conditions and material properties. A summary of their individual contributions follows.

Zhang *et al.* noted that applying displacements directly to the lung surface could lead to poor results, because determining accurate point-to-point matching on the lung surface from images is impossible due to the lack of any definable landmarks [17]. However, the high contrast between lung and surrounding soft tissue allows for relatively accurate surface-to-surface matching. Therefore, Zhang proposed creating a solid mesh representing EE and a shell mesh representing the boundary of EI. Tumor subjects were considered in this study. Contact

constraints prevented the solid mesh from expanding beyond the limiting geometry. Quadratic tetrahedral elements (10-node) were used for the EE volume mesh. Uniform pressure was applied to the solid mesh, expanding the solid to fill the cavity formed by the limiting geometry. A frictionless contact, enforced with the penalty method, was applied between the lung surface and the limiting geometry. Linear elastic material properties were used with a Young's modulus (E) of 4 kPa and a Poisson's ratio (v) of 0.35. The simulated volumes ranged 3.2 – 4.0 L. No quantitative measure was used to evaluate simulation accuracy. Instead, a qualitative analysis determined that 'good agreement was obtained, especially at the lower lobe of the lung'.

Villard *et al.* created a model similar to Zhang to evaluate the effects of E and v on the final displacement field [15]. Tumor subjects were considered in this study. It was found that E had minimal effect on the final displacements. Increasing E simply mandated larger surface pressures to sufficiently expand the solid to the limiting geometry. However, v had a profound effect on the model. Increasing v resulted in increased shear stresses in the model. This makes sense as v represents the compressibility of the material. Higher v indicates a material that would rather deform significantly (potentially resorting to high shear stresses) than change in volume. Landmark error was not assessed.

Al-Mayah took a slightly different approach by discretizing the EI geometry to form the solid as well as the limiting geometry, then deforming the limiting geometry to match the EE volume. There are currently three published papers by this group with contradicting results. In 2008 Al-Mayah *et al.* explored the impact of material nonlinearity and contact boundary conditions on landmark error [11]. It was found that linear elastic material properties without a contact boundary condition worsened landmark error from 3.5 mm pre-simulation to 7.4 mm post-simulation. Hyperelastic material properties with a contact boundary condition improved landmark error from 3.5 mm pre-simulation to 1.7 mm post-simulation. They did not evaluate linear elastic material properties with contact, so one cannot determine whether the improvement was due to hyperelastic material or the contact boundary condition. They concluded that

hyperelastic material properties with a contact boundary condition are necessary for accurate results.

In 2009 Al-Mayah *et al.* tested the effect of Poisson's ratio and friction between the solid and the limiting geometry on landmark error [28]. Tumor subjects were considered in this study. However, unlike Villard, Al-Mayah specified stiffer material properties to tumor regions in the model (E = 7.8 kPa for tumor and E = 3.74 kPa for healthy lung). The reported optimum condition was a frictionless contact model with a Poisson's ratio of 0.4. Average landmark error in this case was roughly 2.88 mm. Closer inspection of the data indicates that landmark error varied by approximately 0.2 – 0.4 mm when testing the range of Poisson's ratio (0.35 to 0.499) and coefficient of friction (0 to 0.2).

In 2011 Al-Mayah *et al.* attempted optimization of their model input parameters concerning accuracy and computation time [29]. They report a post-simulation landmark error of 2.8 mm regardless whether linear elastic or hyperelastic materials were used. This paper concludes that linear material properties, linear elements, and linearized geometry are preferable for modeling lung deformation since none had a significant effect on landmark error. The accuracy of these models, however, is suspect. If data similar to their previous paper was used then landmark error was improved from 3.5 mm to 2.8 mm. This is only an improvement of only 20%.

Werner *et al.* [27] tested the effect of E and v on a lung FE model similar to previously mentioned models by Villard and Zhang. E was varied from 0.1 to 10 kPa and Poisson's ratio was varied from 0.2 to 0.45. The effect of E and v on landmark error was small (0.2 mm average, <= 1 mm maximum). Their average landmark error was 3.3 +/- 2.2 mm. This is a slightly larger error than the 2.8 mm achieved by Al-Mayah, however their landmark motion was nearly double (6.6 mm vs. 3.5 mm). Intraobserver variability in landmark identification was reported at 0.9 +/- 0.8 mm. Landmark error for centrally located landmarks did not significantly differ from landmarks near lung boundaries. However, the presence of larger tumors caused increased

landmark error near the tumor. Werner did not attempt to model the tumors and concluded that large tumors do alter lung dynamics both globally and regionally in FE models.

Chhatkuli *et al.* used the mesh-free method to simulate lung motion from EE to EI [30]. The lung tissue was analogized as a linear elastic, viscoelastic solid (E=0.78 kPa and v=0.46). Their results indicate error of around 2 mm, validated using gold markers positioned in the lung.

Conclusions from all previous models are that, in general, Young's modulus and Poisson's ratio can be arbitrarily assigned within the tested ranges without significantly affecting landmark error. All previous models were patient specific and constructed based off 4DCT data of tumor patients. Each lung half was modeled independently as a continuous solid. Landmark error is on the order of 3 mm, however, appears to increase with increased landmark motion (observation by comparing studies).

1.6 Motivation

Image guided radiotherapy (IGRT) is commonly used to treat patients with lung cancer. IGRT leverages images and image registration to track tumor motion and lung motion in order to design treatment plans that increase the amount of diseased tissue killed while limiting damage to the healthy tissue. IGRT can be used either in conjunction with respiratory gating or with tumor tracking. Respiratory gating involves tracking tumor motion during a predefined, reproducible portion of the respiratory cycle, usually end-expiration. The targeted region does not change during treatment. Tumor tracking involves tracking tumor motion throughout the respiratory cycle in order to move the irradiated region along with the tumor. Improved targeting in IGRT requires a better understanding of how the lung moves and deforms during breathing and requires tools that can measure and predict internal lung displacements. Radiation oncologists can also leverage a better understanding of lung function in order to predict function change post-treatment.

Deformable image registration (DIR) is commonly used to measure displacements throughout the lung [24, 25, 31-33]. Most DIR models are driven by image-intensity

information, often referred to as image-based DIR; herein referred to simply as ‘image registration’ or ‘DIR’. Image registration takes two images (in this case an image at two time points in the respiratory cycle) and estimates where each point in one image moved to in the other image. It can be shown that image registration performs well near definable landmarks but one can question the accuracy away from landmarks. Finite element models (FEM), sometimes referred to as physics-based DIR [11, 17], are also be used to predict internal lung motions and have been previously proposed as a tool to aid IGRT [11, 15, 27]. FEM models the lung tissue and the forces at the lung boundary to estimate internal displacements by solving physically-based equilibrium equations. The major difference between DIR and FEM is the former estimates the displacement field from images while FEM estimates the displacement field by modeling the physics of the situation. Mechanical FEM may be appropriate for the lung as the driver of lung deformation is the mechanical coupling between the diaphragm, chest wall and pleural cavity; see Section 1.2.

FEM has applications beyond radiation therapy and beyond the scope of DIR. FEM can determine the forces at both the lung boundary as well as internally. This can be used to answer questions such as: how much harder is it for the patient to breathe with a tumor? How does gravity affect the regional volume changes in the lung? FEM can be used to determine material properties through reverse finite element modeling. FEM can be used to predict lung motion under a variety of changing scenarios. For instance, how might lung deformation change during radiation therapy? How will lung deformation change for chest wall dominated breathing versus diaphragm dominated breathing? Prediction of lung motion may also have application in the reconstruction of 4DCT datasets serving as a guide or initial guess.

FEM has other applications within the scope of IGRT. For instance, our current understanding of respiratory motion summarized by Keall [34] indicates no general patterns of respiratory behavior. He states: ‘The many characteristics of breathing – quiet versus deep, chest versus abdominal, healthy versus compromised, etc. – and the many motion variations associated with tumor location and pathology lead to distinct individual patterns in displacement,

direction, and phase of tumor motion [34]. FEM is a tool that can simulate different methods of breathing in order to assess the causes of differences in respiratory motion. Also, radiation results in scar tissue formation in healthy lung regions, likely dose related. If the dose delivered can be correlated to a predictable change in material stiffness then FEM can model how lung function may look post-treatment. Currently high function regions are typically avoided during therapy, however, that operates under the assumption that each region of the lung operates independently. It is likely that a function change in one region of the lung has a global effect. The global effect to a given regional change in function can be simulated in FEM to provide better analysis of the effectiveness of IGRT.

Success of FEM depends on how appropriately the underlying physiology is modeled. This dissertation addresses a specific approach to account for an aspect of lung physiology widely recognized, but almost never addressed: the sliding between the lobes in the lung. In order to understand the ability of FEM to model physiology a brief background on lung anatomy and mechanics is required.

1.7 Specific Aims

The objective for this dissertation is to build upon state-of-the-art FE models reported in the literature by incorporating the role of lobar sliding and to assess its effect on estimations of lung deformation.

Aim 1: Develop a sliding lobe finite element model of the lung. Five patient specific 4DCT finite element models will be used. The FE model will consist of volumetric lobe meshes, representing the lobes, and a pleural cavity surface mesh. 4DCT is desired as radiotherapy treatments occur with the patient breathing. Pleural cavity displacements derived from image registration results will be used to implement the boundary conditions. Contact will be enforced between the lobes and the pleural cavity. A consistent, standard protocol will be developed for use in Aim 2. Model parameter choices will be evaluated to improve displacement field accuracy

and simulation convergence including frictional coefficient, Young's modulus and Poisson's ratio.

Aim 2: Assess what effect, if any, that the inclusion of lobar sliding plays in estimation accuracy by comparison with model without lobar sliding. Six patient specific finite element models will be developed from static scans spanning functional residual capacity to total lung capacity. The methodology and optimized material parameters and frictional coefficient will be used from Aim 1. Estimation of displacement field accuracy will be quantified using landmark error. Displacement field differences will be assessed between the developed FE model, lobe-by-lobe image registration and whole lung FE. In addition, lobe sliding and volume change distributions will be compared to that measured from image registration.

CHAPTER 2: PRELIMINARY STUDIES

2.1 Quantification of Lung Deformation[1]

2.1.1 Introduction

Volume change is the primary metric for assessing lung expansion and its health. But volume change in the lungs is not regionally homogeneous [36]. The practice of image-guided radiotherapy brought a need for regional characterizations of lung deformations as lung pathology and the effects of interventions (radiological or otherwise) are essentially region-specific. Methods have been developed to determine regional volume change from the displacement field using deformable image registration and MRI-grid tagging [20, 37]. Finite element simulations of lung deformation also yield a displacement field and, consequently, regional volume change.

Regional deformation of the lung during inspiration and expiration is more than just volume change. Volume change may also have orientational preference – anisotropy of deformation [16, 38]. Volume change and deformation anisotropy are independent quantities as a region may undergo no volume change, but still have deformed significantly – say, when the lengthening in one orientation is compensated by contraction along another orientation. Devoid of orientational preference, regional volume change alone may not do full justice to characterization of lung deformation, and this may have clinical implications. For example, consider two cases: one, a lung with fibrosis at its inferior region (close to the diaphragm); two, a healthy lung but with poorly functioning diaphragm. In both cases, the volume change may conceivably be lower at the inferior regions. But the anisotropy of deformation will likely be significantly affected only in the latter. Or perhaps, regions closest to the diaphragm are likely to

[1] This information is published in: Amelon *et al.*[35].

experience more volume change in the vertical orientation, or regions closest to the heart may be more constrained from expanding normal to the heart.

In classical mechanics, deformation of structures is characterized by the regional distribution of a strain or stretch tensor. Previous reports have addressed lung deformation using traditional methods employed in mechanics. West *et al*. [16] computed and reported lung regional strains along the anatomical orientations using an idealized 3D finite element model under the influence of gravity. They made visual observations of shape changes that occurred in the inferior portion of the model, but stopped short of quantifying it. Rodarte *et al*. [38] used parenchymal markers to quantify regional strains along the anatomical orientations. A comparison of strain magnitudes revealed a dominant transverse strain throughout the lung, though mean strains tended to be greater in the lower lobes. Napadow *et al*. [21] quantified strains using spin-inversion MRI. In addition to reporting strains along the standard anatomical orientations, they also reported the difference between strains in the coronal and sagittal axes – noted as in-plane shear strain. Cai *et al*. [20] used MRI grid-tagging to report regional ventilation and principal strains in two dimensions. Others have estimated point-wise displacements in the lung, but are often concerned only with accuracy of registration (verified using landmark error) which can be used for image-guided radiotherapy [24, 39, 40]. While strains entirely capture the deformation, use of strains themselves (be it principal strains or strain components based on an intuitive coordinate system) to interpret the nature of lung deformation may not be the best approach for a few reasons. One, strain components lump the effect of volume change with the preferential directionalities involved in volume change rendering independent interpretations difficult. Two, strains aren't physiologically intuitive within the context of lung deformation which is essentially about volume change. Three, the lungs do not have an intuitive coordinate system based on which individual strain components could be interpreted.

We submit that, regional lung deformation is best interpreted by indices that independently capture different aspects of lung deformation. The objective of this work is to

develop indices of lung deformation that independently capture volume change and the level and nature of orientational preferences that occur in volume change; and that these indices be intuitive and relevant to the physiology of lung function. Such indices will permit future studies on regional lung deformation (both experimental and computational) to make physiologically relevant interpretations from displacement fields determined by image registration based measurements or by numerical modeling.

2.1.2 Methods

2.1.2.1 Development of indices

We propose quantification of regional lung deformation using three independent measures determined from the displacement field, such that their physical meanings accommodate the essentially volumetric nature of deformation in the lungs. The indices are volume change (J), an anisotropic deformation index (ADI) and a slab-rod index (SRI) – defined and explained subsequently.

To understand the rationale and definitions behind these indices, consider that a point at position X in a body moves to a position x resulting in a displacement vector, $u = x - X$. The deformation gradient tensor, $\boldsymbol{F}$, describes the continuum deformation from the point-wise displacements.

$$\boldsymbol{F} = \frac{dx}{dX}$$

$\boldsymbol{F}$ may be decomposed into a rotation tensor $\boldsymbol{R}$ and a stretch tensor $\boldsymbol{U}$. Since the rotation tensor is orthogonal, it may be factored out by squaring $\boldsymbol{F}$.

$$\boldsymbol{F} = \boldsymbol{RU}$$

$$\boldsymbol{F^T F} = \boldsymbol{U^T R^T RU} = \boldsymbol{U^T U}$$

The eigenvalues of $\boldsymbol{U}$ are the principal stretches, λ_1, λ_2, and λ_3. The principal stretches may be calculated by,

$$\lambda_i = \sqrt{eigen\ values\ of\ \boldsymbol{F^T F}}.$$

Physically, if we consider an infinitesimal cube at a given point stretching to a rectangular cuboid (in the general case), the principal stretches are the ratio of the deformed length to the undeformed length in each of its three essential dimensions. The eigenvectors of $\boldsymbol{U}$ represent the orientations along which the principal stretches occur. Together, the principal stretches (eigenvalues of $\boldsymbol{U}$) and their orientations (eigenvectors) exhaustively capture regional lung deformation. But as with principal strains, principal stretches themselves do not quite help interpret the nature of lung deformation. Instead, the proposed indices (J, ADI and SRI) describe the relationships among the stretches with relevance to lung volumetric expansion. With three independent stretch ratios, there must be three independent indices of lung deformation for completeness.

The first index of lung deformation is the widely used Jacobian of deformation (J), a measure of volume change [37, 41] which in terms of the stretch ratios is,

$$\mathrm{J} = \lambda_1\lambda_2\lambda_3$$

J is the ratio of the current volume to reference volume for a given region. J varies from 0 to ∞. It can be equal to 1 corresponding to no volume change, less than 1 corresponding to reduction in volume (net contraction), or greater than 1 corresponding to an increase in volume (net expansion). J is not a new index we introduce, but rather an existing index, which we retain here as it captures regional volume change.

The second and third indices are derived from a shape-change spectrum graph. They capture the level and nature of orientational preference in volume change. Defining the principal stretches such that $\lambda_1 \geq \lambda_2 \geq \lambda_3$, a plot may be created with α on the x-axis and β on the y-axis.

$$\alpha = \frac{\mathrm{J}-1}{|\mathrm{J}-1|}\left(\frac{\lambda_2}{\lambda_3}-1\right)$$
$$\beta = \frac{\mathrm{J}-1}{|\mathrm{J}-1|}\left(\frac{\lambda_1}{\lambda_2}-1\right)$$

This graph and the indices derived thereof is conceptually similar to the Zingg plot used in geology literature for characterizing pebble shapes [42]. The plot was later adopted by Flinn for characterization of the deformation of rocks [43, 44]. We adopt these approaches, but with some modifications to suit our context. As opposed to characterizing shape, where the principal axes are all positive, deformation can be thought to have sign (expansion '+', contraction '-'). When data points are plotted on this graph (see Figure 6A), for all regions within the lung where principal stretches are known, those regions undergoing volumetric expansion fall in the first quadrant and those undergoing volumetric contraction fall in the third quadrant. It should be noted that x and y axes are independent of volume change.

The origin represents regions that underwent perfectly isotropic volume change ($\lambda_1 = \lambda_2 = \lambda_3$). The farther a point is from the origin, the more anisotropic the deformation. Thus, the distance of a data point from the origin captures the magnitude of anisotropy and is defined as the anisotropic deformation index (ADI). ADI ranges from 0 to ∞ where 0 indicates perfectly isotropic deformation.

$$\mathrm{ADI} = \sqrt{\left(\frac{\lambda_1 - \lambda_2}{\lambda_2}\right)^2 + \left(\frac{\lambda_2 - \lambda_3}{\lambda_3}\right)^2}$$

In addition to the magnitude of anisotropic deformation, the nature of anisotropy – i.e., whether the volume change is predominant along one or two orientations – is captured by the angular position on this graph. Thus, points nearer to the y-axis (where $\frac{\lambda_1}{\lambda_2} \gg \frac{\lambda_2}{\lambda_3}$; stretching occurs mostly in one orientation) represent regions where a cube would turn into a prolate cuboid (rod-like) while points nearer the x-axis (where $\frac{\lambda_2}{\lambda_3} \gg \frac{\lambda_1}{\lambda_2}$; stretching occurs mostly in two orientations) represent regions where a cube turns into an oblate cuboid (slab-like). The angular position therefore captures where a particular region falls within the spectrum of shapes between

these extremes. The angular position of a data point on this graph, normalized to a 0 to 1 range, thus captures the nature of anisotropy and defined as the slab-rod index (SRI).

$$\mathrm{SRI} = \frac{\tan^{-1}\left(\frac{\lambda_3(\lambda_1-\lambda_2)}{\lambda_2(\lambda_2-\lambda_3)}\right)}{\pi/2}$$

Figure 6B demonstrates how the deformed cuboids would look at different positions on the shape spectrum; J is held constant at 1 and plotted in the 1st quadrant.

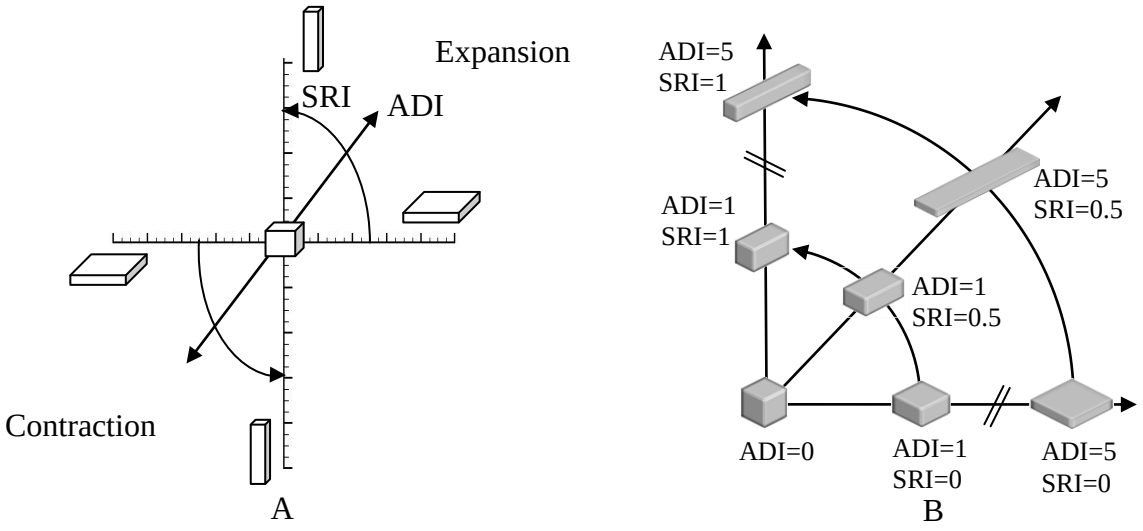

Figure 6: Illustration of relationship between ADI and SRI. (A) Illustration of the shape change spectrum graph. Anisotropic deformation index (ADI) corresponds to the radius of a point from the origin. SRI corresponds to the angle from the x-axis. J is constant over the entire graph but regions undergoing expansion and contraction are separated into the first and third quadrants respectively. (B) Illustration of the meanings of the shape change indices by placing a deformed cube at different positions on the shape spectrum. Volume change is held constant. In human subjects studied, the ADI ranged from 0 to 2.4 (5th to 95th percentile) and SRI from 0 to 1.

J, ADI and SRI are indices with independent physical meanings that describe both the volume change and orientational preferences to it. A final piece of information, that when accounted for would make the characterization of lung deformation exhaustive, is the orientations of the principal stretches (eigenvectors of $\boldsymbol{U}$). For ease of interpretation, it may be worthwhile to study the orientation of the maximum principal stretch alone, when considering expansion, as this is the orientation of primary deformation during expansion. It is best perceived visually by plotting the orientation vectors along maximum principal stretch on a finite number of sectional slices of the lung. Because the orientation of the maximum principal stretch is of little consequence when ADI is low (isotropic), it is prudent to weight the maximum principal stretch vector lengths with ADI.

2.1.2.2 Evaluation of indices in human lungs

All data were gathered under a protocol approved by our institutional review board. Pairs of volumetric CT data sets from six normal human subjects in supine orientation were used in this study. Of the six subjects, four were male and two were female. Subject age ranged from 22-37 years with a mean of 27.3 years. Functional residual capacity (FRC) lung volumes ranged from 2.67-3.75 liters with a mean of 3.22 liters. The six patients were non-smokers with no recorded exclusion criteria (recent respiratory infection, medication other than contraception, cardiopulmonary abnormalities, pregnancy or breast feeding, diabetes mellitus, positive PPD or history of tuberculosis, CT scan within the last year). Each image pair was acquired with a Siemens Sensation 64 multi-detector row CT scanner (Forchheim, Germany) during breath-holds near FRC and total lung capacity (TLC) in the same scanning session. Voxel dimensions were approximately 0.6x0.6 mm in the axial plane with a section spacing of 0.5 mm along the longitudinal axis. Linear elastic image registration, parameterized by a uniform cubic B-spline function, was used to register the static scan image pairs to obtain a 3D displacement field. Minimization of a cost function was used to obtain reasonable registration results. The cost function minimized the sum of squared tissue volume difference [23] while incorporating a

Laplacian smoothing filter. Detailed information on the registration process may be found in Cao *et al*. [25]. The distribution of voxel-wise displacements were then used to estimate the regional distribution of principal stretches and J, ADI and SRI as previously described. Contour plots were constructed to visualize distribution patterns of the three indices for Subjects 1 and 2. A three-dimensional vector plot was used to visualize the orientation of the maximum principal stretch weighted by ADI. Lobar indicial statistics were evaluated for all six subjects. For post-processing, the parenchyma was segmented first using Hu *et al*.[45], followed by an automatic lobe segmentation algorithm defined by Ukil *et al.* [46]. Further, since vessel regions may be expected to have a particularly anisotropic deformation, the vessels were segmented and analyzed separately using the Pulmonary Workstation 2.0 (VIDA Diagnostics, Inc., Iowa City, IA) based on methods previously reported by our group [47]. Vessel data was available for Subjects 1 and 2.

2.1.3 Results

Regional variations exist in J, ADI and SRI for subjects as seen on sequential sagittal slices from right to left (see Figures 7 and 8). Regionally, J is elevated at the inferior and dorsal ends of the lungs. ADI is elevated at the inferior region close to the diaphragm and also roughly along lobar fissures. SRI is not elevated predominantly in any particular localized region, but rather appears elevated at various localized spots in the lung. The maximum principal stretch vectors weighted with ADI (vector length=0 at ADI=0) are plotted on transverse slices of the lung (Figure 9). At the inferior region of the lung, the vectors were longer (higher ADI) and oriented roughly toward the diaphragm surface suggestive of a preferential deformation along that orientation. The vectors further indicate that regions farther from the diaphragm generally do not tend to expand/contract in any one preferential orientation save a few regions near the chest wall boundary.

Subject 1

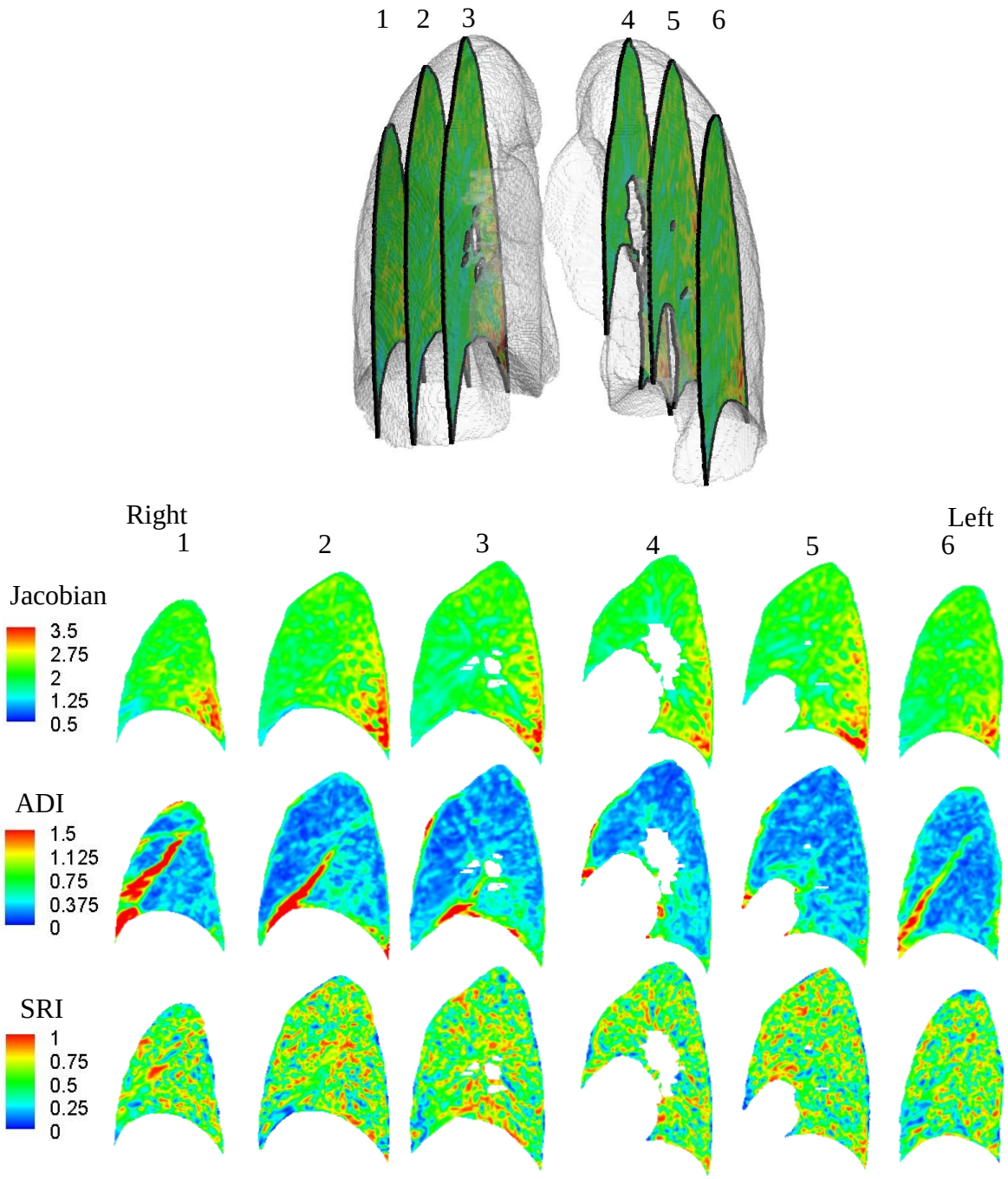

Figure 7: Contour plots for Subject 1 showing the distribution of J, ADI and SRI on 6 sagittal slices from patient right to left.

Subject 2

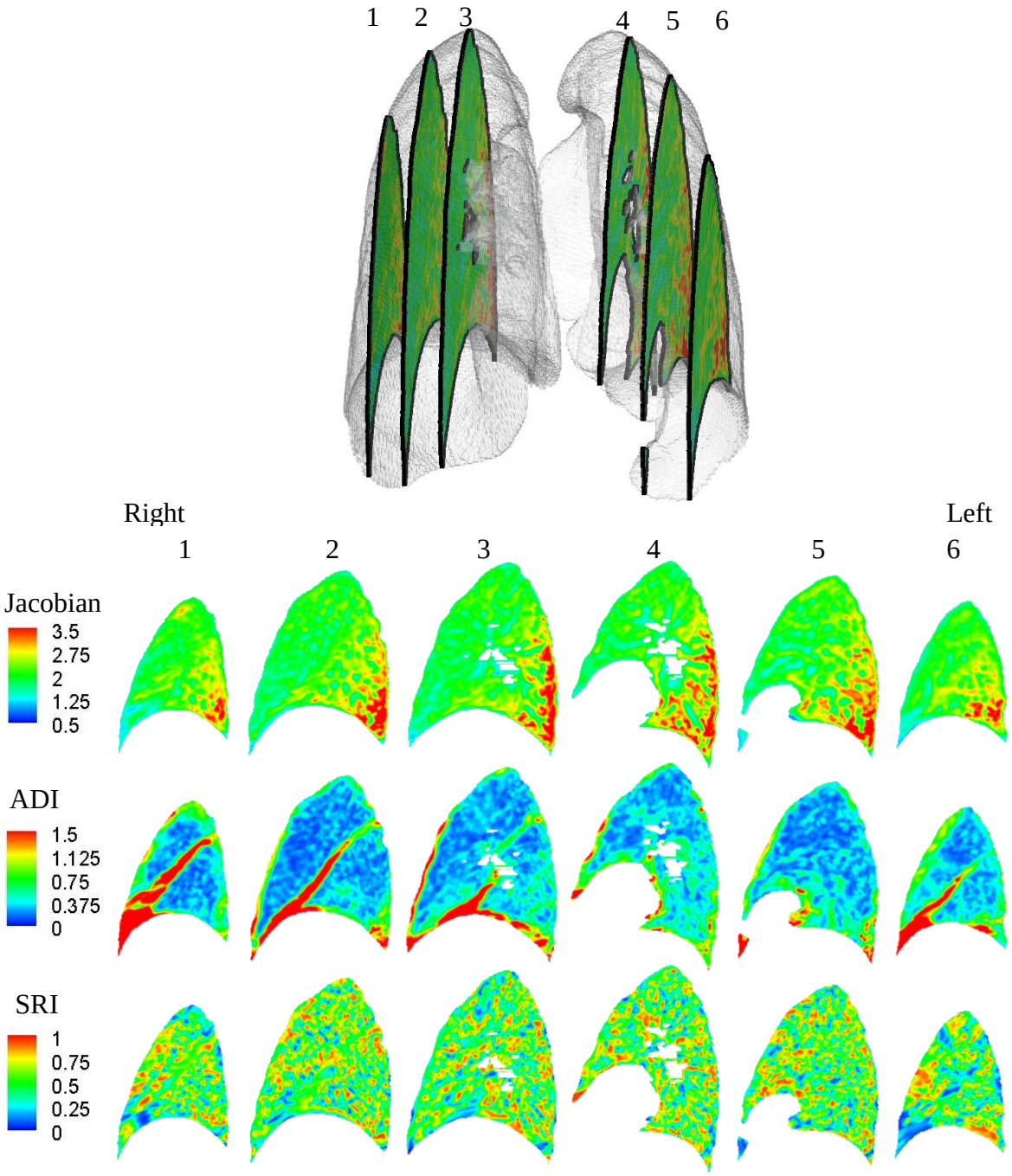

Figure 8: Contour plots for Subject 2 showing the distribution of J, ADI and SRI on 6 sagittal slices from patient right to left.

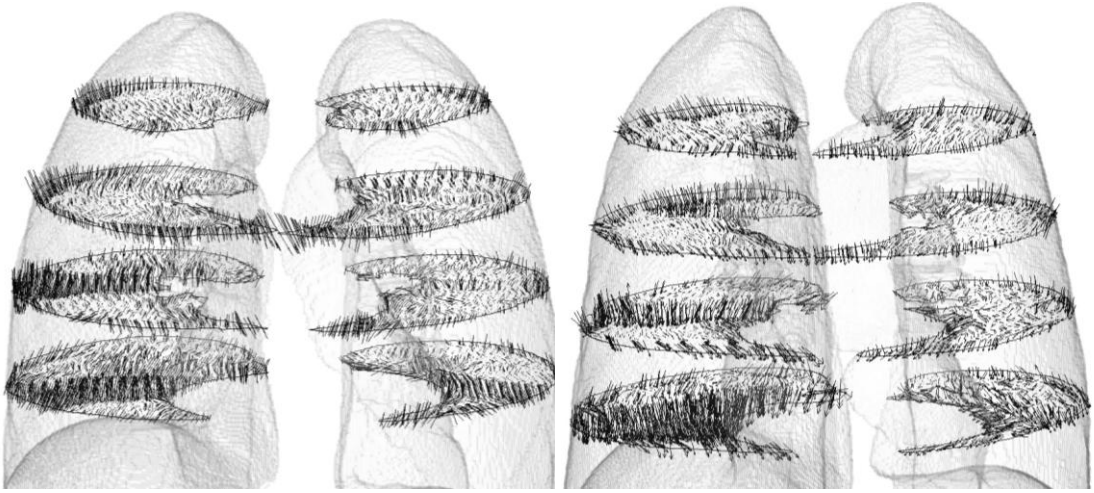

Subject 1 Subject 2

Figure 9: Vector plot of maximum principal stretch orientation weighted with ADI. For clarity the vectors are plotted on 4 transverse slices. Only a fraction of the vectors in a given slice is shown for clarity.

Indicial ranges were stratified on a lobar basis (see Figure 10). J was highest in the lower lobes and least in the right middle lobe with a remarkable consistency across subjects. ADI was highest in the right middle lobe and lowest in the upper lobes also consistently across subjects. No consistent trend was qualitatively identified for SRI between lobes. A paired student t-test showed that the medians of J and ADI in the lower lobes were greater than that for the corresponding upper lobes with statistical significance. J in the lower lobes was 19.4% and 21.3% greater than the upper lobes in the right ($p<0.005$) and left ($p<0.005$) lungs respectively (see Figure 10). Similarly, ADI in the lower lobes was 26.3% and 21.8% greater than in the upper lobes in right ($p<0.05$) and left ($p<0.05$) lungs respectively.

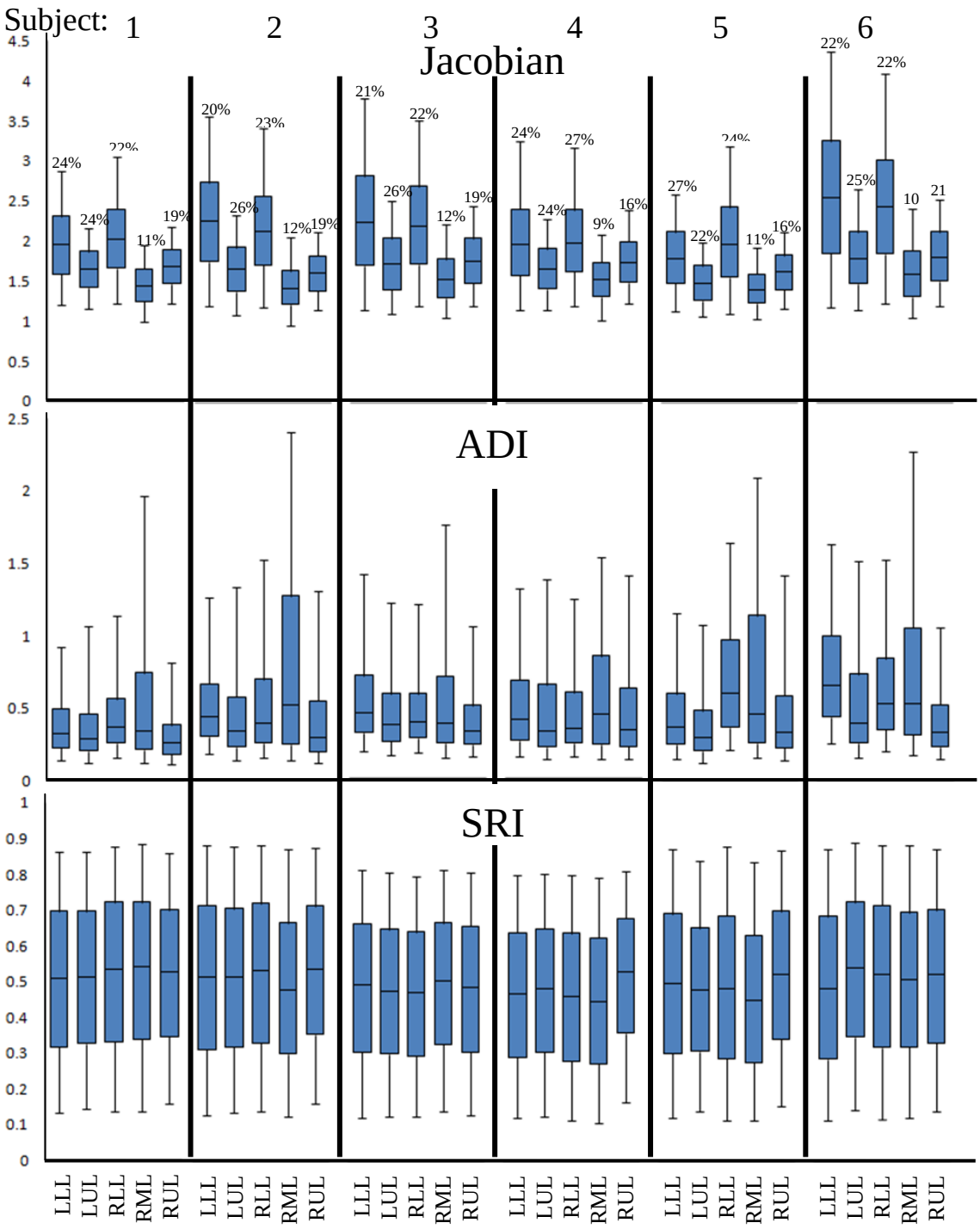

Figure 10: Box plots of the distribution of J, ADI and SRI in the six study subjects stratified by lobe. The bounds of the box represent the 25th and 75th percentile; the horizontal line inside the box represents the median; and the error bars extend from the 5th to 95th percentile. The percentage above each box represents lobe volume as a fraction of the total lung volume at FRC for that subject. LLL – left lower lobe; LUL – left upper lobe; RLL – right lower lobe; RML – right middle lobe; RUL – right upper lobe. The sample sizes for the quartiles are roughly the number of voxels in the particular lung lobe and range between 175K and 700K.

The indices were also evaluated for differences between the whole lung, all vessels, and only large vessels (roughly less than or equal to 4^{th} -5^{th} generation), (see Figure 11). When compared to the whole lung, J was substantially lower in the large vessels (32% and 35% lower medians for Subjects 1 and 2 respectively) and moderately lower in all vessels (23% and 22%). Similarly, compared to the whole lung, SRI was substantially elevated in major vessels (23% and 43% higher medians for Subjects 1 and 2 respectively) and moderately elevated in all vessel regions (17% and 14%). Differences in ADI, if they exist, were not noticeable.

2.1.4 Discussion

Lung parenchymal deformation is primarily about local volume change. It can vary regionally, especially in the presence of localized pathologies. A complete description of local volume change must consider the amount of volume change as well as orientational preferences in volume change.

Conventionally, lung deformation is characterized by the amount of tissue 'stretching'. But note that the term stretch may be used loosely when referencing the lung. Mechanically, tissue stretch is often associated with λ_1. However, often lung tissue stretch refers to large inflation of the lung – that is three-dimensional expansion (large J), not large λ_1 [48-51]. Reporting principal stretches alone leaves out physiologically relevant information and can lead to misinterpretations of lung function. While less prevalent, limitations of reporting one-dimensional shear indices instead of ADI is similar to the limitations in reporting λ_1 instead of J. We proposed and demonstrated a set of regional indices that separates lung deformation into volume change and shape change characteristics in a physiologically intuitive manner. As deformation is three dimensional, complete quantification necessitates the use of three independent indices.

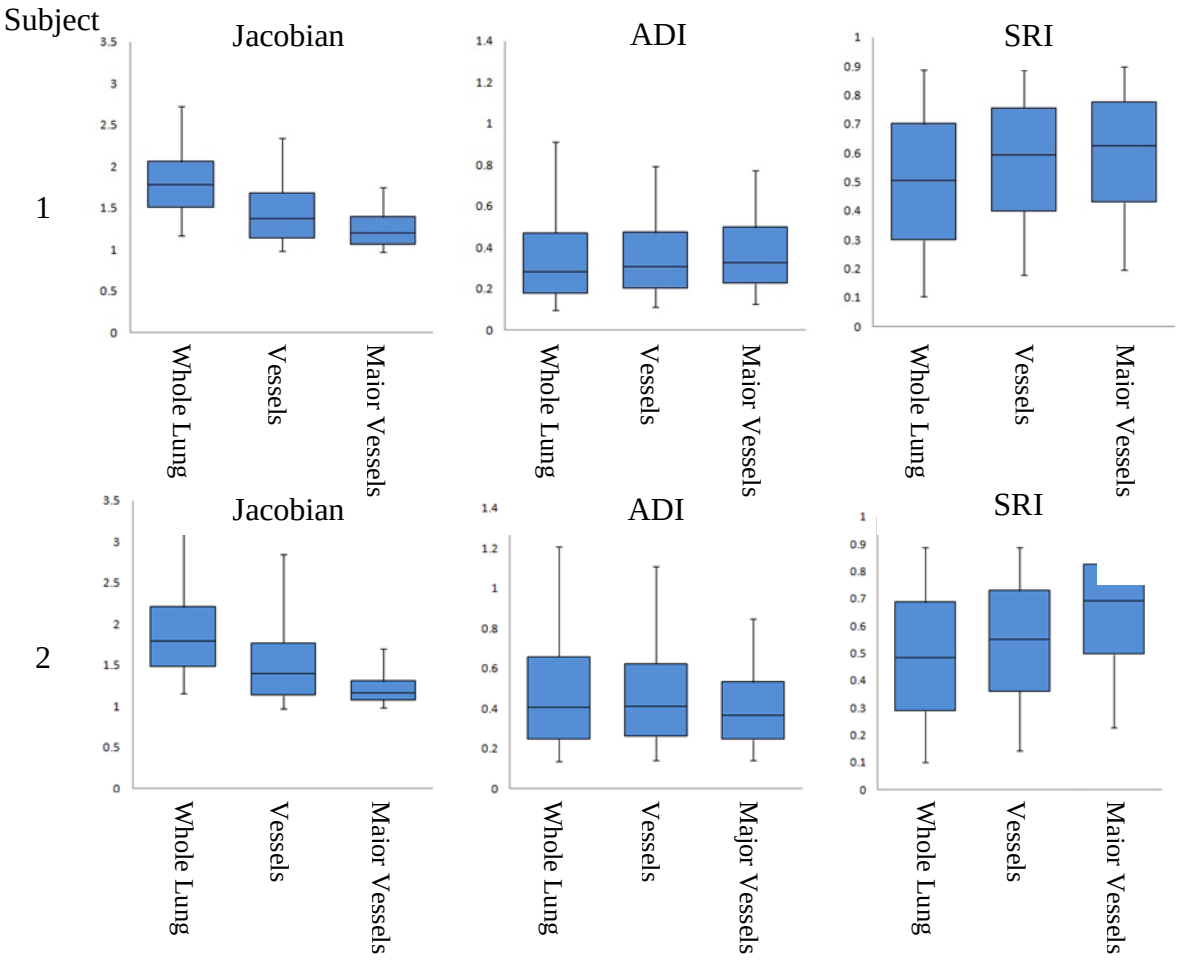

Figure 11: Box plots showing the distribution of J, ADI and SRI throughout the lung, in the vessels and in the major vessels (roughly the vessels of the 5th generation or lesser) only. The bounds of the box represent the 25th and 75th percentile; the horizontal line inside the box represents the median; and the error bars extend from the 5th to 95th percentile. The sample sizes for the quartiles are roughly the number of voxels in the associated data set and range between 33K (major vessels) and 2.7M (whole lung).

In the six human subjects evaluated in this study, the volume change index (J) was elevated at the dorsal, inferior region suggestive of a localized region of high volume change (Figures 7 and 8). The diaphragm is the primary driver of lung deformation and hence, the region closest to it – the inferior region – is likely experiencing elevated volume change compared to superior regions. Also, dorsal regions experience more volume change than ventral regions.

These observations are all consistent with expected volume change for subjects in the supine position [37] suggesting that the registration methods adopted are reasonable and the volume change index (J) captures that essential aspect of lung function. Only subjects in the supine position were analyzed from FRC to TLC. The distribution of J has been shown to change with patient orientation [16, 52, 53] and at different stages of breathing [54] therefore, it is likely that all indices will observe different distributions at different patient orientations and stages of breathing.

The fact that ADI was elevated in inferior regions is not unexpected when considering the boundary conditions. In the superior lung, the chest wall and diaphragm may have near equal contributions on expansion while in the inferior lung the vertically acting diaphragm is the primary driver of deformation. Elevated ADI values are also observed along the fissures where lobar sliding is expected [4]. But since our methods use a continuum approach, sliding is reflected as a very anisotropic deformation resulting in an elevated ADI at the fissures. Fissure sliding may be the reason for elevated ADI in the right middle lobes which have a greater surface area experiencing sliding compared to its volume.

The contour plots yield no identifiable regional trends in SRI. However, comparison of deformation indices between vessel regions and the whole lung suggest that the former deform differently (see Figure 11). Vessels are expected to undergo lower volume change compared to parenchyma during lung expansion and this is reflected in the lowered J for vessel regions. It is in this comparison that the utility of SRI becomes apparent. SRI places anisotropic deformation on the spectrum between rod-like (high) to slab-like (low) volume change. Conceivably, during lung expansion, the cylindrical vessels likely deform more by extending in length than by dilating radially (i.e., rod-like expansion). Such a rod-like expansion of vessel structures will result in high SRI. Some caution is warranted in interpreting SRI for contracting regions where the maximum principal strain is likely the least negative and has a smaller absolute value than the minimum principal strain, providing the motivation for separating expanding from contracting lung regions. In the contracting case a rod-like shape will result from contracting

primarily in two orientations while a disk-like shape is from contracting in one orientation. Therefore, interpretation of SRI needs to be reversed when one considers a primarily contracting volume change such as during expiration. In this study, we have confined to reporting deformation from FRC to TLC where contracting regions are a small fraction of expanding regions and, therefore, this issue does not impact our interpretations. Unlike SRI, ADI in vessels was relatively similar, which highlights the importance of capturing anisotropy using two independent indices. SRI, a measure of the nature of anisotropy, uniquely captures phenomenon in deformation that ADI, a measure of the magnitude of anisotropy, does not capture. One remarkable observation in this study was the consistency across subjects in the lobe-specific volume change (Figure 10) – especially in J – even though the FRC-TLC total lung volume change differed by about 40% between subjects (2.67 L to 3.76 L).

With increasing improvements in registration techniques, there will be increasing fidelity in acquiring regional displacements within the lung. The proposed indices of regional lung deformation – J, ADI and SRI – and the orientation of maximum principal stretch allow for physiological interpretation of these displacement fields. Decoupling the causes (material properties and boundary effects) from their resulting effects (changes in observed deformation) can provide insights into disease detection and the effect of diseases on lung function. These indices may permit approximately decoupling these two determinants of lung expansion through the use of finite element simulations.

2.2 Lobe Sliding from CT Images[2]

2.2.1 Introduction

The human lung is divided into five lobes, three in the right lung and two in the left lung. The lobes contact each other to create four inter-lobar boundaries, Figure 12. Herein the

[2] Portions of this section were published at SPIE, 2011 [55].

boundaries are labeled as follows: Left Upper – Left Lower boundary (LU-LL); Right Upper – Right Middle boundary (RU-RM); Right Upper – Right Lower boundary (RU-RM); Right Middle – Right Lower boundary (RM-RL). During breathing the lobes slide with respect to each other [4, 5, 20, 56], which is thought to reduce parenchymal distortion [56].

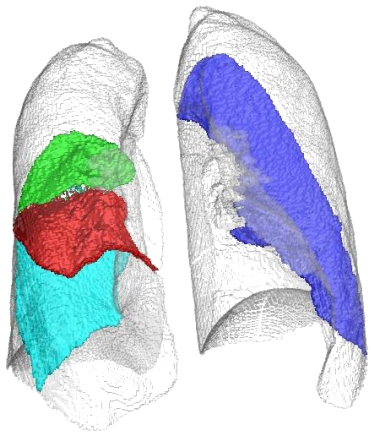

Figure 12: A legend illustrating the four lobe boundaries: (Green) RU-RL boundary, (Red) RU-RM boundary, (Cyan) RM-RL boundary and (Blue) LU-LL boundary.

Literature on quantification of lung lobe sliding is scarce. In 1987, Hubmayr *et al.* used parenchymal markers to quantify lobe rotations about the transverse axis in dogs [56]. Lower lobes rotated opposite that of upper lobes during mechanical ventilation in supine position, indicative of sliding. In 2009, Ding *et al.* quantified lung lobe sliding from lobe-by-lobe image registration of CT scans by interpolating the displacement field on either side of the fissure to the fissure surface [4]. Up to 20mm of sliding was observed in the extreme ventral portions of the LM-LL boundary, increasing from nearly no sliding near carina. However, due to complexities in the algorithm only the left lung was considered as it contains only a single fissure. Cai *et al.* used grid-tagged MRI to obtain a displacement field for the lung [5]. They clearly noted a discontinuity in the displacement field along fissure surfaces including differences in the

direction the lobes moved. These methods prove that lung lobe sliding exists, but limitations due to methodological complexities or low resolution limit understanding and the ability to characterize lobe sliding in the lung.

A better understanding of regional lung deformation and mechanics of breathing will aid the practice and evaluation of image guided radiotherapy (IGRT). Relative lung lobe sliding may be a key driver in determining how the lung deforms. Lung lobe sliding, when improperly accounted for, also influences many state-of-the-art techniques for measuring and modeling local lung deformation. Specifically, deformable image registration (DIR) typically requires displacement field regularization, which smoothes potential discontinuities [4]. Likewise, finite element modeling (FEM) of lung deformation explicitly models the lung as a continuum which prohibits modeling of lobe sliding [27, 29]. The significance of neglecting discontinuities at lobe boundaries in either method is not understood as the nature of sliding between lung lobes is relatively unaddressed in literature. Understanding where and to what degree lobe sliding occurs gives an indication as to where potential errors exist in the continuum assumption. The clinical implications arise when such methods are proposed to aid treatment planning for radiation therapy [24, 27, 29, 57]. The objective of this paper is to characterize lung lobe sliding from CT scans and demonstrate its influence on traditional whole lung registration.

2.2.2 Methods

2.2.2.1 Shear as a surrogate for sliding

Given any 2D/3D displacement field, if a significant discontinuity in the displacement field exists, and the displacement field is analyzed as a continuum, then the discontinuity will manifest as a region of elevated shear stretch. This concept can be demonstrated in two-dimensions, Figure 13. The setup for this demonstration is two bodies in space where the space is discretized using a grid; analogous to two lung lobes discretized with a voxel grid, Figure 13A. When the upper block is slid relative to the lower block, with no internal distortions, the elements spanning the boundary between the two bodies is distorted, Figure 13B. This distortion

is shear deformation that manifested not due to actual shearing of the individual bodies, but due to relative sliding between the bodies. This demonstrates the theoretical framework for quantifying sliding in images using shear deformation.

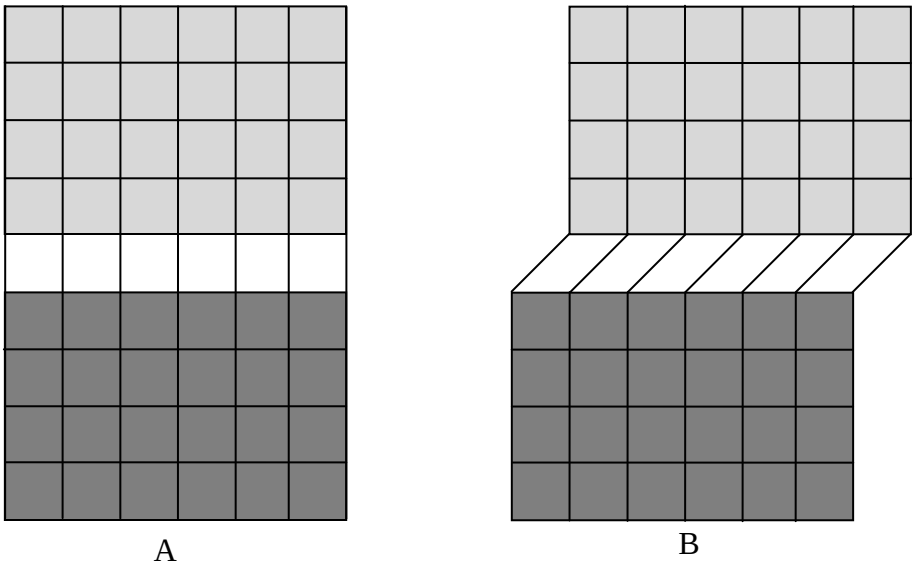

Figure 13: A 2D example showing the relationship between sliding and shear. (A) Two bodies (light and dark) where the space is discretized with square elements. In (B), the light block is slid relative to the left block. The shear deformation of the squares spanning the boundary between the light and dark blocks represents sliding and not actual shear deformation.

2.2.2.2 3D quantification of shear

The relationship between shear deformation and sliding in images translates well to three-dimensions. Shear deformation can be quantified from any 3D displacement field using finite elasticity theory. The deformation gradient tensor, $\mathbf{F}$, describes the transformation of any infinitesimal region from the reference state, dX, to the final state, dx. $\mathbf{F}$ is directly related to the displacement gradient tensor, $\nabla\mathbf{u}$. $\mathbf{F}$ is comprised of a rotational component, $\mathbf{R}$, and a

deformation component, $\mathbf{U}$. Isolation of the deformation component is accomplished by squaring $\mathbf{F}$ as $\mathbf{R}$ is an orthonormal tensor. Principal stretches are obtained by eigenvalue decomposition of $\mathbf{U}$. The eigenvalues and eigenvectors represent the magnitude and orientation, respectively, where only normal deformation exists. Shear deformation in a given orientation is quantified by the off-diagonal components of the stretch tensor. Mohr's circle demonstrates the in-plane relationship between principal and shear tensor components. Figure 14 illustrates that the maximum shear (γ_{max}) for any stretch tensor is half the difference between the maximum (λ_1) and minimum principal (λ_3) stretch components.

$$\mathbf{F} = (\boldsymbol{\nabla}\mathbf{u})(\boldsymbol{\nabla}\mathbf{u}^{\mathrm{T}})$$

$$\mathbf{F}^{\mathrm{T}}\mathbf{F} = (\mathbf{RU})^{\mathrm{T}}\mathbf{RU} = \mathbf{U}^{\mathrm{T}}\mathbf{R}^{\mathrm{T}}\mathbf{RU} = \mathbf{U}^{\mathrm{T}}\mathbf{U}$$

$$\gamma_{\max} = \frac{(\lambda_1 - \lambda_3)}{2}$$

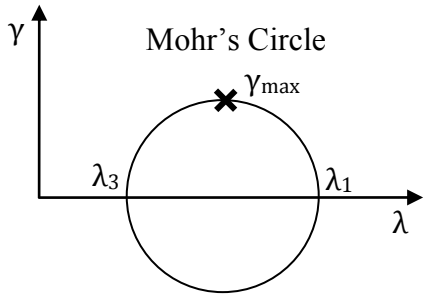

Figure 14: Mohr's circle demonstrates the relationship between shear and axial stretch ratios. Maximum shear is marked with an 'X' and is given by half the difference between the maximum and minimum principal stretch ratios.

A three-dimensional example of the relationship between sliding and shear deformation is demonstrated with a phantom cube, Figure 15. Consider two blocks, one on top of the other. The space is discretized such that each cube is made up of 9x9x4 voxels with a single voxel layer

spanning the boundary between the blocks. Together, they resemble a single square block of 9x9x9 voxels with a fissure half-way along its height (A). Consider that the bottom block rotates 30° about its central height axis while the top block remains static (B). The resulting displacement field is shown in (C) – displacements are zero in the upper block and gradually increase with distance from central axis in lower block. This creates a discontinuity in the displacement field at the fissure plane with zero sliding at the center of the fissure (axis of rotation) and gradually increasing sliding with distance from the axis of rotation. Maximum shear, γ_{max}, is computed for all the voxels (not just the voxels at the fissure) and shown in D. As expected, the maximum shear deformation is zero in all non-fissure regions and the maximum shear stretch map captures the radially increasing sliding magnitude at the fissure. This demonstrates that in this context, γ_{max} quantifies relative sliding.

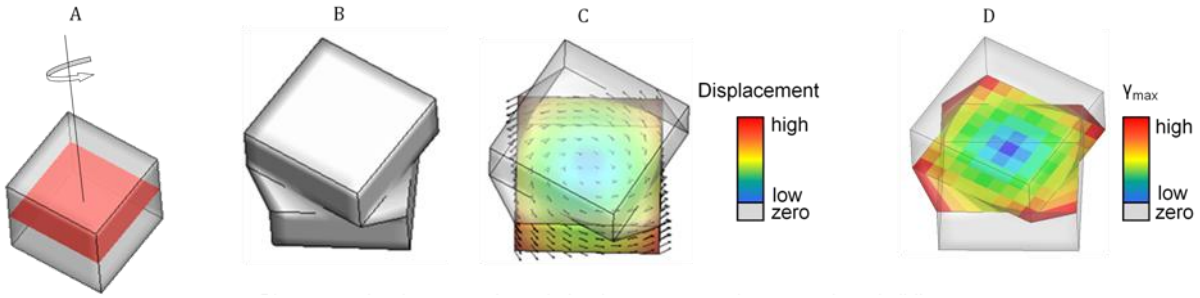

Figure 15: An illustration of the relationship between sliding and γ_{max}.

The shear example demonstrated the idealized relationship between rigid bodies. In the lung γ_{max} will lump contributions of lobe sliding with actual tissue shear. If γ_{max} is dominated by sliding at the lobe boundaries then it can be considered a good index for capturing relative lobe sliding magnitude.

2.2.2.3 Image Acquisition and Registration

All data were gathered under a protocol approved by the institutional review board at the University of Iowa. Pairs of volumetric CT data sets from six normal human subjects in supine orientation were used. Each image pair was acquired with a Siemens Sensation 64 multi-detector row CT scanner (Forchheim, Germany) during breath-holds near functional residual capacity (FRC) and total lung capacity (TLC) in the same scanning session. Voxel dimensions were approximately 0.6×0.6x0.5 mm and resampled to a 1x1x1 mm voxel grid for registration. Of the six subjects, four were male and two were female. Subject age ranged from 22-37 years with a mean of 27.3 years. FRC lung volumes ranged from 2.67-3.75 liters with a mean of 3.22 liters. The six patients were non-smokers with no recorded exclusion criteria (recent respiratory infection, medication other than contraception, cardiopulmonary abnormalities, pregnancy or breast feeding, diabetes mellitus, positive PPD or history of tuberculosis, CT scan within the last year). Lobe segmentations were used in the analysis process and followed the protocol outlined by Ukil *et al.* [46].

Linear elastic image registration, parameterized by a uniform cubic B-spline function of grid size 4x4x4 mm, was used to register the static scan image pairs to obtain a 3D displacement field. The transformation cost function minimized the sum of squared tissue volume difference (SSTVD) [23]. The displacement field is regularized with a Laplacian smoothing filter. Detailed information on the registration process may be found in Cao *et al*. [25].

Traditional, whole lung registration occurred by registering the segmented lung in TLC to the segmented lung in FRC. The output is a 3D displacement vector at each voxel in the FRC image space.

Lobe-by-lobe registration occurred by independently registering each of the five segmented lobes from FRC to TLC (five registrations per subject). The resulting displacement fields were then combined into a single voxel grid for analysis. Lobe-by-lobe registration is identical to whole lung registration without regularization across lobe boundaries and no inter-lobe contributions to the respective cost function (i.e. no penalty for lobe sliding).

2.1.3 Results

Coronal slices displaying contours of γ_{max} are shown in Figure 16. Dorsal slices are presented because in many subjects the illuminated boundary disappears in the medial portion of the lung even though a discontinuity was enforced using lobe-independent registration.

To better visualize sliding along the fissures, the parenchymal nodes were removed from the model leaving a 3D perspective of the lobar boundaries, see Figure 17.

Quantitative measures of sliding per lobe boundary are summarized across subjects as well as sliding averaged across all subjects, Figure 18.

Inspection of Figure 17 suggests a positive correlation between sliding and distance from the carina, as Ding *et al.* previously suggested for the left lung. This correlation was found for all subjects in this study as well.

The sliding metric was also calculated for traditional whole lung segmentation on the same six subjects. A sliding metric comparison, demonstrated with saggittal slices, of lobe-by-lobe and whole lung registration for corresponding subjects can be found in Figure 19.

2.1.4 Discussion

A better fundamental understanding of lung mechanics and physiology will influence how abnormalities are detected, diseases treated, and lung motion modeled. Sliding between lung lobes is a widely acknowledged but poorly characterized aspect of lung physiology. The importance of a better understanding of lung lobe sliding is underscored in how it affects the ability of state-of-the-art techniques, such as DIR, to measure regional lung motion. On the other hand, DIR has only recently allowed lobe sliding to be adequately measured in human subjects with the method presented in this study.

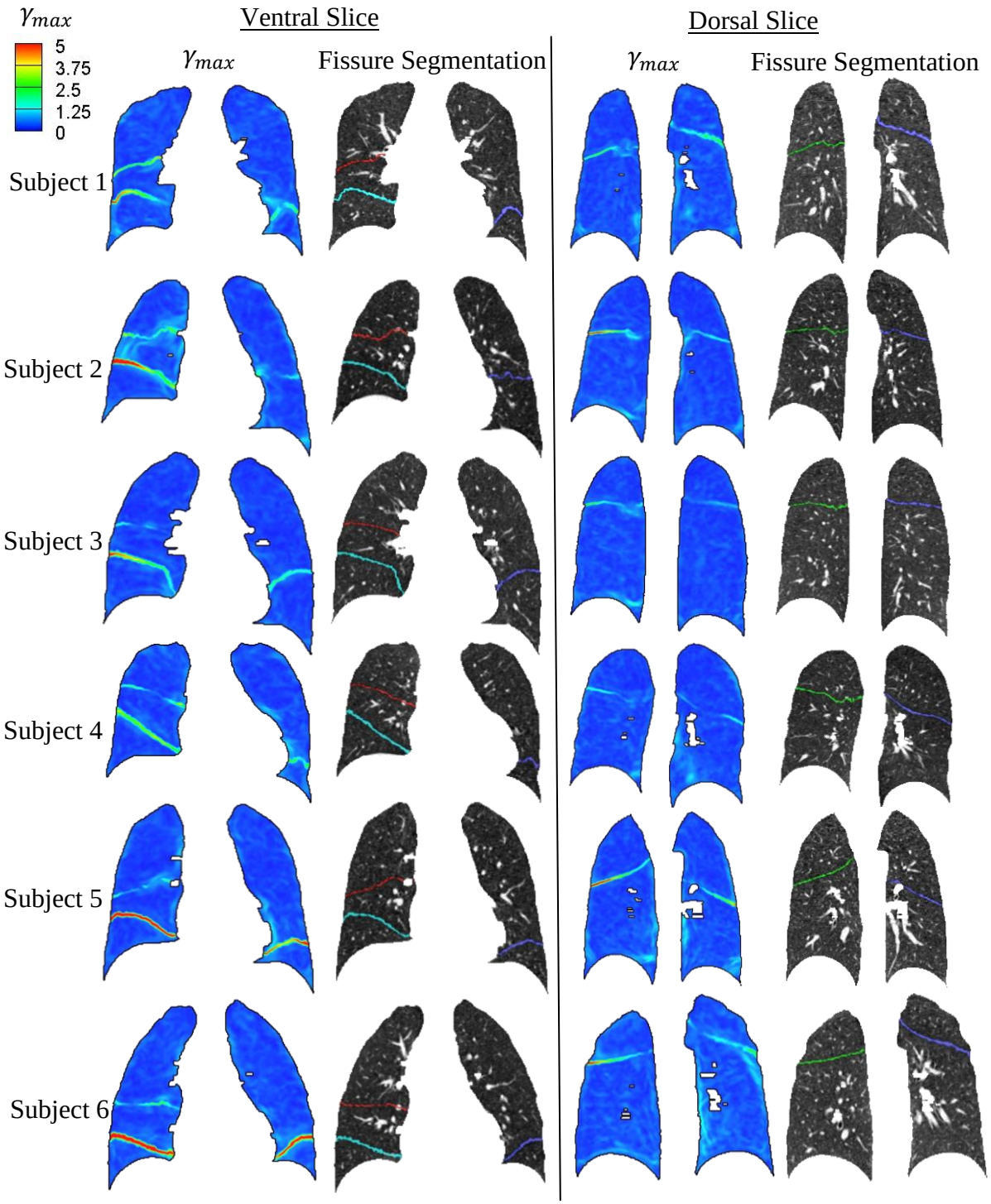

Figure 16: Coronal slices of maximum shear stretch on a ventral and dorsal slice for one subject

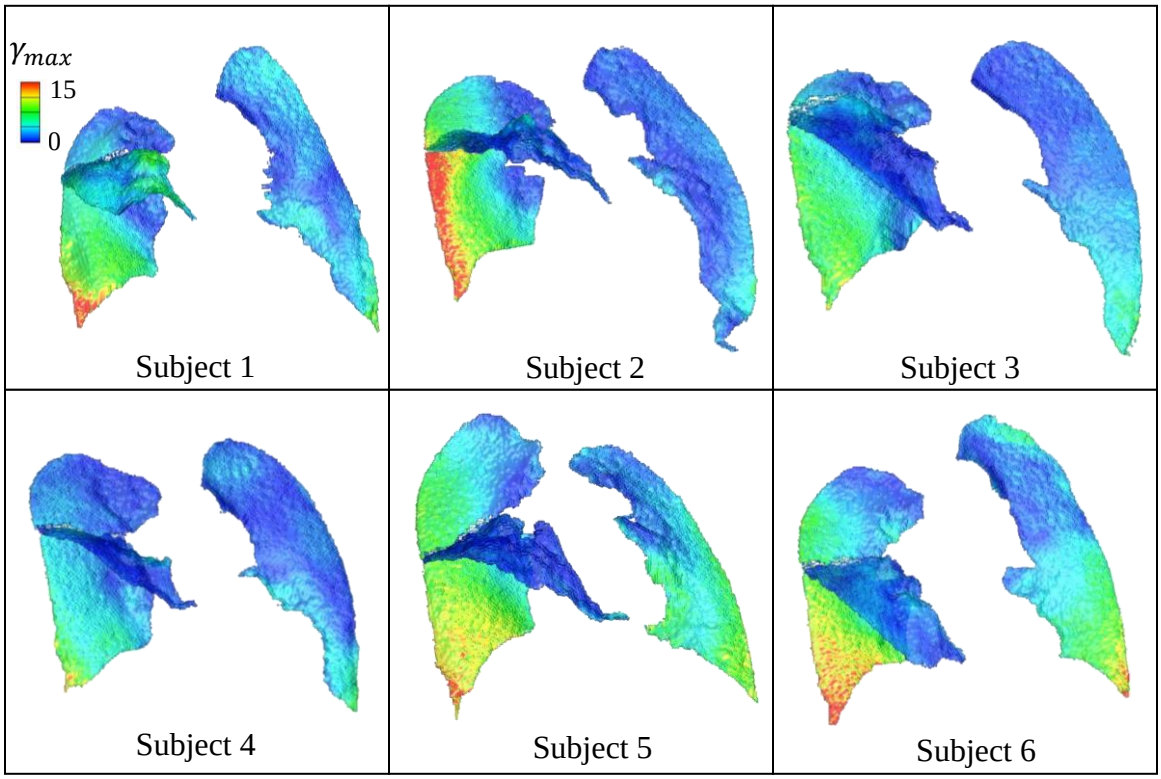

Figure 17: Max shear stretch contour on lobe boundaries.

There are groups stressing the importance of acknowledging the discontinuity at lobe boundaries with physiologically meaningful DIR algorithms. Yin *et al.* developed a registration method that accounts for discontinuities at lobar fissures [26]. The discontinuity in the displacement field was quantified in the method similar to Ding *et al.* [4] and also was confined strictly to the left lung. Sheng *et al.* reported significantly improved finite element results by meshing each lobe independently allowing inter-lobar motion [58]. Their results were checked against ^{3}He MR tagging. Modat *et al.* state that their registration algorithm could be improved by accounting for the slipping between the lobes [31]. Characterization of lobe sliding is mandatory for identifying the influence of lobe sliding on DIR and to further establish clinical relevance.

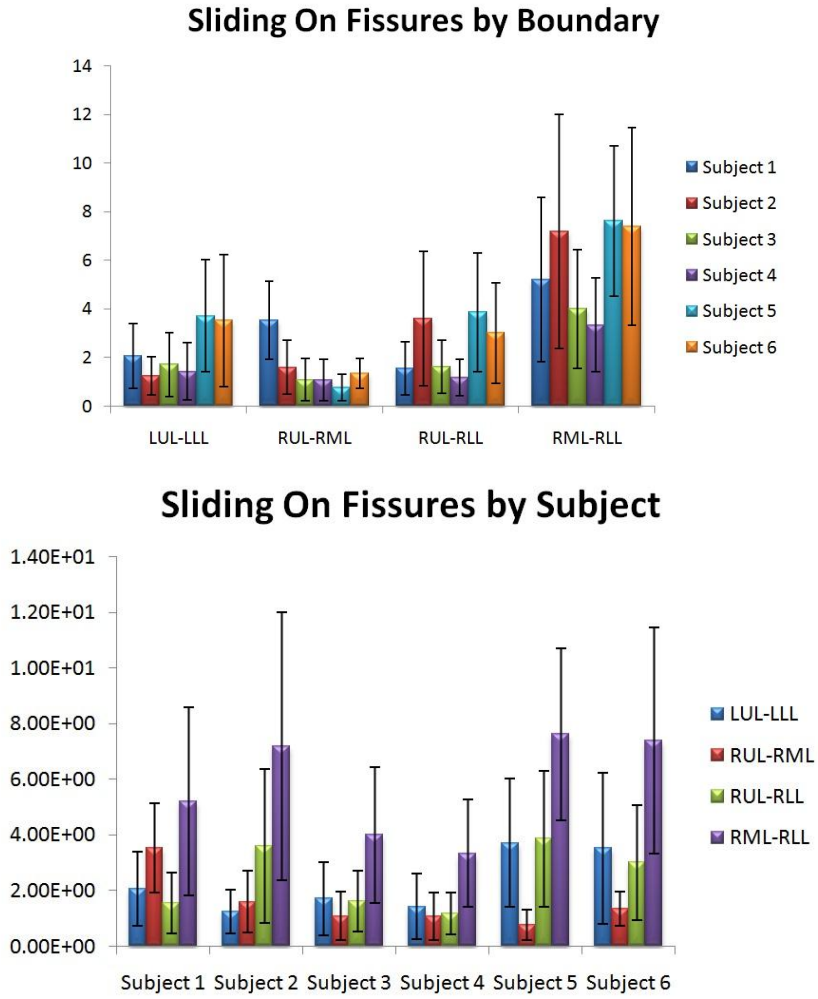

Figure 18: Sliding parameter stratification. (top) Distribution of voxel-wise γ_{max} stratified by subject, sorted by lobe boundary. (bottom) Distribution of voxel-wise γ_{max} stratified by lobe boundary, sorted by subject.

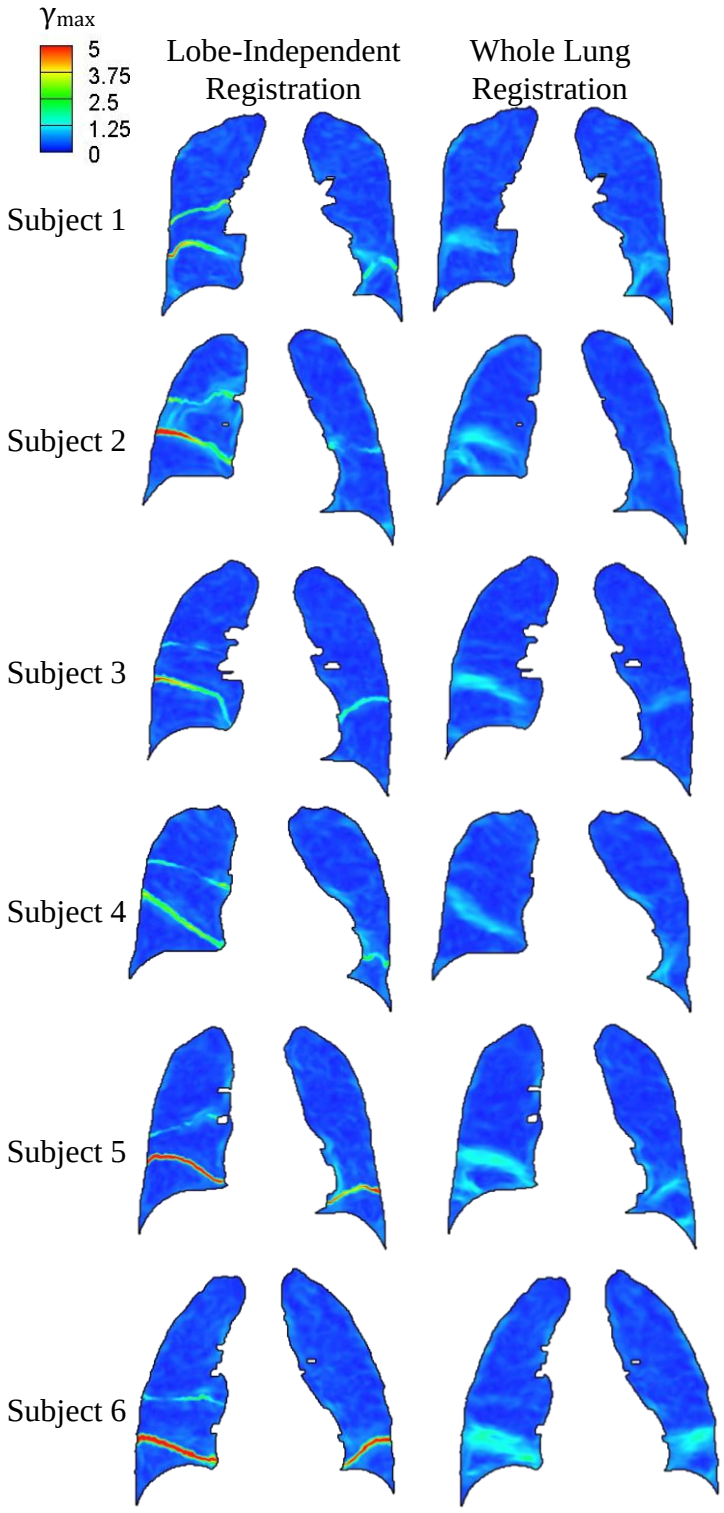

Figure 19: A comparison of γmax contoured on saggittal slices for lobe-by-lobe registration results (left) and whole lung registration results (right).

The proposed index, γ_{max}, is much greater at internal lobe boundaries than in the parenchyma. The result of DIR is a 3D vector displacement image. A discontinuity in the displacement field, such as that introduced by lobe sliding, will manifest as shear deformation of the underlying voxel grid. In this context, if sliding affects γ_{max} significantly more than actual tissue shear then γ_{max} can be used as a surrogate for sliding. As γ_{max} is as much as 15x greater at lobe boundaries than in the parenchyma, we conclude that the elevated γ_{max} at lobe boundaries likely has little contribution from actual tissue shear. This means that the elevated γ_{max} at lobe boundaries is a combination of lobe sliding and registration error. Currently there is no ground truth displacement data near lobe fissures for error checking.

Figure 15 demonstrates the positive correlation between elevated sliding and shear in an idealized displacement field. An advantage to shear as a proxy for sliding is that no prior knowledge of the discontinuity location is necessary. The limitations to using shear to represent sliding are that 1) shear is a unit-less quantity whose magnitude depends of element size and 2) shear magnitude is affected by how the discontinuity intersects the element. In this study, the former concern is mitigated by resampling the voxel grid to a 1x1x1mm voxel grid prior to analysis. The latter concern is limited by considering the sliding field as a whole rather than individual voxel results.

Sliding in human subjects was analyzed using lobe-by-lobe DIR to allow sliding at lobe boundaries. Figure 16 demonstrates much greater γ_{max} at lobe boundaries opposed to throughout the parenchyma. This demonstrates lesser natural tissue shear in the lung and the effect of the discontinuity at the lobe boundary has much more influence on γ_{max} than actual tissue shear.

A 3D perspective of the lobe fissures contoured with γ_{max} illustrates the characteristics of sliding along lobe boundaries. Sliding increases with increasing distance from the carina or mediastinum. This trend can be visually observed in the Figure 17. First, notice that the dorsal slices report very little sliding toward the medial lung. This is not unexpected as the internal structures of the lung (airways and blood vessels) enter and exit the lung near this point; which should limit the sliding. There is some consistency in sliding trends between subjects. The most

sliding occurs at the RM-RL boundary while the least sliding is observed at the RU-RM boundary. Furthermore, the RU-RL and RM-RL boundaries are often combined and termed the right oblique fissure. Figure 17 demonstrates a nearly continuous transition for γ_{max} between these two boundaries indicating the RU and RM lobes reorient within the pleural cavity in a similar manner – different from the RL lobe. The gradient in γ_{max} along the boundaries suggests sliding due to differences in lobe rotations with the carina or mediastinum being the axis of rotation (similar to that proposed by Rodarte *et al.* [38]); sliding owning to translation would be a constant over the surface. The phantom cube demonstrates sliding magnitude due to differences in rotation.

Sliding can have a significant influence on traditional whole lung registration. Figure 19 compares γ_{max} contour for lobe-by-lobe and whole lung registration. In regions of elevated γ_{max} from lobe-by-lobe registration there is a corresponding elevation of γ_{max} in whole lung registration. This suggests that the intensity- and feature-based cost metrics attempt to impart a discontinuity in the displacement field. However, the b-spline parameterization and regularization across lobe boundaries limits the degree of discontinuity. In regions of elevated γ_{max} the regularization term is dominating the displacement field, thus, indicating severe artifact due to poor incorporation of lobe sliding. Results in these areas should be questioned as they likely contain a high level of error. Error is typically quantified with landmark error. Ding *et al.* previously published a minimal difference in landmark error between lobe-by-lobe and whole lung registrations [4]. This indicates that not incorporating sliding has a small impact on lung registrations at the whole lung level. However, this is a poor quantity for capturing error relevant to lobe sliding as no landmarks exist near lobe fissures. If an unaccounted for 15mm discontinuity exists, then at that point there would be a 7.5mm error at best.

Since no landmarks exist near fissures, the accuracy of sliding captured by image registration such as in this paper may be questioned. However, there are indications in the data supporting the notion that the magnitude of sliding is reasonably represented. The consistency in the results displayed in Figures 17 and 18 suggests a definable trend and not random noise. Also,

increased γ_{max} in whole lung registration supports the notion that sliding exists without introducing a bias of pre-segmented lobe boundaries.

2.1.5 Conclusion

A method for quantifying relative lung lobe sliding was presented. To our knowledge this is the first time the regional nature has been quantified in both right and left lungs. The influence of neglecting sliding in DIR was demonstrated. It can be concluded that lobe sliding results in a significant discontinuity in each lung and its effects should be considered whenever quantifying lung motion. Further studies should focus on sliding influence at the tidal breathing level as well as other applications.

CHAPTER 3: DEVELOPMENT OF A FINITE ELEMENT LUNG MODEL

Section 2.2 demonstrates that lobe sliding exists and imparts a significant discontinuity in the displacement field. Current state-of-the-art finite element (FE) lung models mesh the lung as a continuum, thus prohibiting sliding at lobe boundaries. The effect of neglecting sliding at lobe boundaries in FE on the resulting displacement field has not been studied. This chapter focuses on the development of a new FE lung model paradigm that incorporates sliding at lung lobe boundaries and evaluates changes in displacement field accuracy with varying material properties and inter-lobar frictional coefficients.

3.1 Methods

3.1.1 Finite Element Concept

The new finite element (FE) model concept is a modification of that proposed by Al-Mayah, herein referred to as whole lung FE (FE_{WL}) (see Section 1.5) [29]. The concept utilizes a pleural cavity surface representation to deform the underlying lung volume from a higher lung volume to a lower lung volume. Pleural cavity surfaces are easily distinguishable in CT scans, see Figure 3. It is not possible, however, to determine pleural cavity displacements. Therefore, a frictionless boundary condition allows sliding between the pleural cavity and lung volume, Figure 20. This enforces deformation to the lower lung volume with minimal influence from individual pleural cavity nodal displacements. In this case, exhalation is modeled as deformation goes from a higher lung volume to a lower lung volume.

To allow sliding between lung lobes the volumetric whole lung mesh is replaced by independent lobe meshes. Figure 21 illustrates the difference in initial geometries between FE_{WL} and the proposed lobe sliding FE. Contact boundary conditions prevent the lobes from penetrating each other while allowing relative lobe sliding. This chapter focuses on methodological development to go from 4DCT through FE solution analysis. Three input

parameters - Poisson's ratio, Young's modulus and the inter-lobar frictional coefficient - were assessed for accuracy and FE solution stability across five subjects.

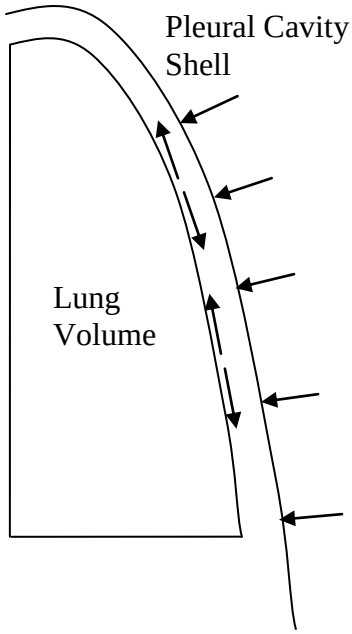

Figure 20: Illustration of the boundary conditions used. Displacements are prescribed for every node on the pleural cavity mesh. Contact allows the pleural cavity to deform while the lung can slide relative to the pleural cavity.

3.1.2 Image Acquisition

The data used in this study is a sub-set of previously collected data published in [59]. The following information on image acquisition and post processing procedures is paraphrased from Du *et al.* [59]. All data from human subjects was gathered under a protocol approved by the University of Iowa Institutional Review Board. 4DCT scans were acquired of five human subjects about to undergo radiation therapy for lung cancer.

Prior to imaging, each subject was trained using a biofeedback system (RESP@RATE, Intercure Ltd., Lod Israel) to provide guidance for maintaining a constant breathing rate. Musical cues were used to pace respiration during imaging, using a technique developed at our institution which was previously shown to have high success.

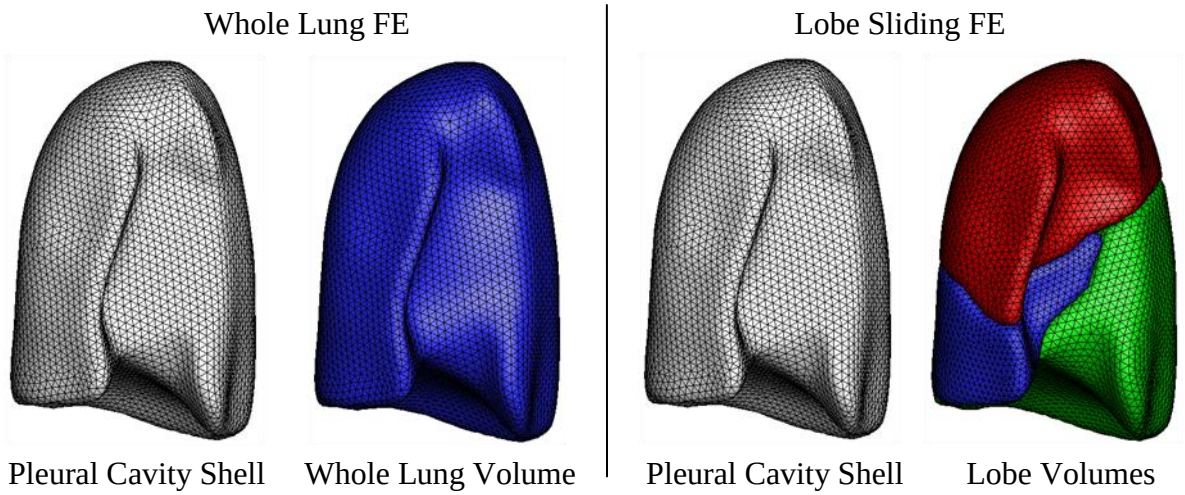

Figure 21: A comparison of whole lung FE and lobe sliding FE. Lobe sliding FE replaces the continuum lung model with independently meshed lobe models.

Patients were scanned in supine position using a 40-slice CT scanner (Siemens Biograph, Hoffman Estate, IL) operating in helical mode. Imaging parameters were 120 kV, 2.0 mm slice thickness, 0.5 mm slice increment, 1.2 mm collimator, B30F medium smooth kernel reconstruction filter. Acquisition occurred with a pitch of 0.1 and either a tube rotation speed of 500 ms per rotation (requiring each respiratory cycle do not exceed 5 s) or 1000 ms per rotation (for respiratory cycles do not exceed 10 s). The amplitude of the respiratory motion was monitored using a strain gauge belt with a pressure sensor (Anzai, Tokyo, Japan). The images were inspected to ensure there were minimal reconstruction artifacts and no severe breathing artifacts or other acquisition problems.

Relevant volume and volume change data calculated from the image data are listed in Table 2. Tumor locations are listed in Table 3.

Table 2: Volume change data for subject population.

Volume Change Data						
Subject	Right Lung 100IN Volume (L)	Left Lung 100IN Volume (L)	Right Lung Volume Change (Jacobian)	Left Lung Volume Change (Jacobian)	Whole Lung Volume (L)	Whole Lung Volume Change (Jacobian)
1	2.96	2.47	1.09	1.08	5.43	1.09
2	1.87	1.71	1.25	1.27	3.58	1.26
3	2.01	1.82	1.14	1.20	3.83	1.17
4	1.70	1.48	1.13	1.12	3.18	1.12
5	1.64	1.02	1.16	1.13	2.66	1.15
Average	2.11	1.81	1.18	1.19	3.92	1.18

Table 3: Tumor location for subject population.

Tumor Location	
Subject	Tumor Location
1	LUL
2	RUL
3	RUL
4	RUL
5	LUL/LLL

3.1.3 Image Segmentation

Images of the human subjects were resampled to a 1x1x1 mm voxel size with image size 304x304x320 voxels. The Pulmonary Workstation 2.0 software (VIDA Diagnostics, Inc., Iowa City, IA) was used to identify the lung regions in the CT images. Lung segmentations at the lower inflation, end-expiration (EE), and the higher inflation, end-inspiration (EI), were necessary. The lung segmentations were manually inspected and modified if necessary.

Modifications included manual separation of the right and left lungs and trachea removal. The binary mask obtained from the segmented lung at this stage will be referred to as the ‘original whole lung segmentation’.

In every case there was a cavity in the original whole lung segmentation where the pulmonary artery and vein enter the lungs, Figure 22. This cavity does not exist in any lung FE simulation in literature and could lead to FE convergence problems. Therefore, this cavity was manually eliminated by following the existing inner contour of the lung, Figure 22. At this point small cavities and protrusions existed in the whole lung segmentations that are not compatible with surface modeling or FE meshing. These were eliminated using a combination of dilation and erosion. The mask was dilated by 3 voxels, eroded by 6 voxels, then dilated by 3 voxels. The original whole lung segmentation after manual filling of the cavity and the dilation-erosion procedure will simply be referred to as the ‘whole lung segmentation’.

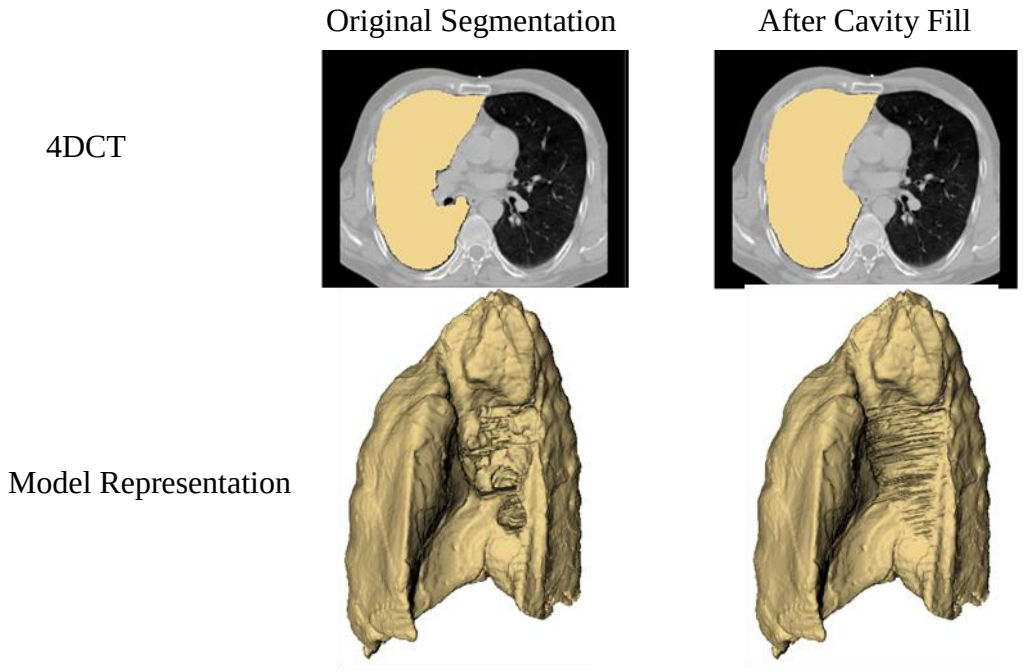

Figure 22: A cavity existed in the original whole lung segmentation that does not exist in any FE models in literature. The cavity was manually filled.

A manual segmentation algorithm, outlined in Appendix A, was developed to obtain lobe masks for each subject. Lobe segmentations were only necessary from EI images. Slicer4 (http://www.slicer.org) was used for lobe segmentation. A filling algorithm was then applied to ensure the combined lobe segmentations and corresponding whole lung segmentation occupied exactly the same space.

3.1.4 Mesh Development

Separate finite element simulations were run for the left and right lungs. Pleural cavity representations of the left and right lungs were formed by the union of the left and right lobes, respectively. The left and right pleural cavity representations will herein be referred to as the right pleural cavity, RPC, and the left pleural cavity, LPC. Surface models of the lobes and pleural cavity representations were constructed and smoothed in Mimics (Materialise) using the method outlined in Appendix B. The surface models were meshed using Gambit (Ansys). The RPC and LPC were meshed using 3-noded triangular elements with a characteristic element size of 6 mm. The RLL, RML, RUL, LLL and LUL volumes were meshed with 4-noded tetrahedral elements with a characteristic element size of 6 mm. The number of elements in the RPC or LPC meshes ranged 4,526 to 8,710 depending primarily on lung surface area. The number of elements for the lobes varied from 7,173 to 53,650 depending primarily on lobe volume. Lobe volumes and total volume calculated from the final FE mesh is listed in Table 4. The total volumes listed here are higher than volumes calculated in Table 2 due to filling of the cavity formed by the pulmonary artery and vein.

3.1.5 FE Assembly

Abaqus (SIMULIA) was used to determine all FE solutions. The simulation was run as dynamic, quasi-static with standard time integration. The quasi-static ensured that the kinetic energy in the system was small compared to the internal energy in the system; this ensured the effects due to inertia were insignificant.

Table 4: Volume information for the finite element mesh at end-inspiration.

EI volumes calculated from final FE mesh (L)						
Subject	**RLL**	**RML**	**RUL**	**LLL**	**LUL**	**Total**
1	0.92	0.55	1.68	0.89	1.74	5.78
2	0.81	0.40	0.80	0.80	1.01	3.82
3	0.91	0.59	0.68	0.77	1.16	4.11
4	0.87	0.29	0.68	0.84	0.72	3.40
5	0.68	0.27	0.80	0.61	0.48	2.84

3.1.5.1 Initial Geometry

Separate simulations were conducted for every lung half of every subject. This resulted in twelve simulation sets (six subjects with two lung halves each). All pleural cavity meshes were defined using 3-noded shell elements (S3R in Abaqus). All lobe meshes were defined using 4-noded tetrahedral elements (C3D4 in Abaqus).

3.1.5.2 Material Property

Homogeneous, isotropic material properties were used in this study. All material property definitions were hyperelastic, Neo Hookean material described by the strain energy density function below. This description was paraphrased from the Abaqus 6.11 User Manual [60].

$$U = C_{10}\left(\overline{I}_1 - 3\right) + \frac{1}{D_1}(J^{el} - 1)^2$$

Where U is the strain energy per unit of reference volume; C_{10} and D_1 are material parameters. $\overline{I}_1$ is the first deviatoric strain invariant defined by,

$$\overline{I}_1 = \overline{\lambda}_1^2 + \overline{\lambda}_2^2 + \overline{\lambda}_3^2.$$

Where the deviatoric stretches $\overline{\lambda}_i = J^{-\frac{1}{3}}\lambda_i$. The material parameters C_{10} and D_1 are related to the small strain shear modulus, μ_o, and small strain bulk modulus, κ_o, by the relations:

$$C_{10} = \frac{\mu_o}{2}$$

$$D_1 = \frac{2}{\kappa_o}$$

μ_o and κ_o are related to Poisson's ratio, ν, and Young's modulus, E, by the infinitesimal strain relations below.

$$\mu_o = \frac{E}{2(1+\nu)}$$

$$\kappa_o = \frac{E}{3(1-2\nu)}$$

The values for the material constants were based on a range of E and ν from literature and translated to the corresponding Neo Hookean input parameters, C_{10} and D_1.

3.1.5.3 Boundary Conditions

A displacement boundary condition was assigned to every node of the RPC and LPC meshes. Displacements were obtained from deformable image registration of the EE whole lung segmentation to the EI whole lung segmentation. This registration utilized the sum of squared intensity difference (SSD) as the cost function. The transform was parameterized with a cubic B-spline of size 4x4x4 voxels. The cost function was appropriate as the masks were binary images, so corresponding points had the same voxel intensity. The method worked well as only boundary displacements were desired. Displacement vectors were then interpolated from the DIR output to the RPC and LPC meshes.

The pleural cavity meshes were fully constrained. A shell element has six degrees of freedom, three displacement degrees of freedom and three rotational degrees of freedom. The

displacement conditions were interpolated from the whole lung registration. The rotational degrees of freedom were set to 0.

Contact pairs were defined between every outer lobe surface and the inner surface of the pleural cavity mesh. Contact was enforced using a linear penalty method. The frictional coefficient between the lobes and the pleural cavity was set to 0.

Contact pairs were defined between the each of the lobe surfaces. Contact was enforced using a linear penalty method. The frictional coefficient, f, was varied to control the amount of sliding allowed by the model.

3.1.6 Input Parameter Perturbation

The range of test material parameters was influenced by reported linear elastic material parameters in literature, summarized by Werner *et al.* [27]. For this study, seven Young's modulus values were considered (units are in kPa): 0.7, 2.8, 4.9, 7, 28, 49, 70. The chosen range centers near the optimal parameters reported by the model most similar to this study's model, Al-Mayah *et al.* [11]. The range spanned 1/10 of the central value to 10x the central value with two equally spaced values between the extremes and the median.

Poisson's ratio spanned seven values: 0.2, 0.25, 0.3, 0.35, 0.4, 0.45, 0.49. This completely covers the range of reported landmark values reported in literature.

Four values for inter-lobe frictional coefficients were tested: 0, 0.5, 1, 1.5. It was assumed that 1.5 would ensure a no-slipping scenario.

Simulations for all combinations of the seven values for E, seven values for ν, and 4 values of f were conducted for a total of 196 combinations of parameter values. When applied across the 10 simulation sets in this study, a total of 1,960 simulations were run.

3.1.7 Landmark Picking

Anatomic landmarks were used to quantify FE solution accuracy. A semiautomatic landmark picking system was employed for landmark selection and establishing correspondence between images [61]. Between 120–185 vascular bifurcation points were manually identified

within the lungs for each data set. Landmark correspondence was established by visualizing the EI and EE images simultaneously. Landmark displacement is defined as the distance between a landmark's EI and EE positions. Landmark distributions are summarized in Table 5. Landmark displacements are summarized in Table 6.

Table 5: Landmark distribution for subject population

Number of landmarks broken down by subject and lobe						
Subject	RLL	RML	RUL	LLL	LUL	Total
1	9	7	41	20	43	120
2	16	6	33	27	38	120
3	18	17	25	10	53	123
4	58	13	32	44	38	185
5	40	8	54	33	11	146

Table 6: Average landmark displacements (mm)

Landmark Displacements (mm)						
Subject	RLL	RML	RUL	LLL	LUL	Total
1	4.34	3.40	3.88	1.73	3.88	3.54
2	17.46	9.08	5.83	18.08	5.63	10.23
3	11.96	5.08	3.41	16.95	5.07	6.71
4	8.59	6.03	3.37	8.78	3.77	6.56
5	10.64	7.42	4.84	5.87	3.17	6.68
Average	10.60	6.20	4.27	10.28	4.30	6.74

Landmark correspondence is a manual process with inherent user variability. An estimate of intra-user variability was obtained by having the same user re-pick Subjects 4 and 5.

3.1.8 Landmark Error Metrics

Due to non-uniform landmark distribution, three different landmark-based error metrics were assessed.

3.1.8.1 Average Landmark Error

Average landmark error captures the difference in final landmark position between the FE predicted and manually selected landmark EE location. If $U_{n,LMK}$ and $U_{n,FE}$ represent the picked landmark displacement vector and FE predicted landmark displacement vector for the n^{th} landmark, respectively, then the average landmark error, ξ, is given by:

$$\xi = \frac{\sum_{n=1}^{N} \left| U_{n,LMK} - U_{n,FE} \right|}{N}$$

where N is the total number of landmarks assessed. A visual representation of landmark error is presented in Figure 23.

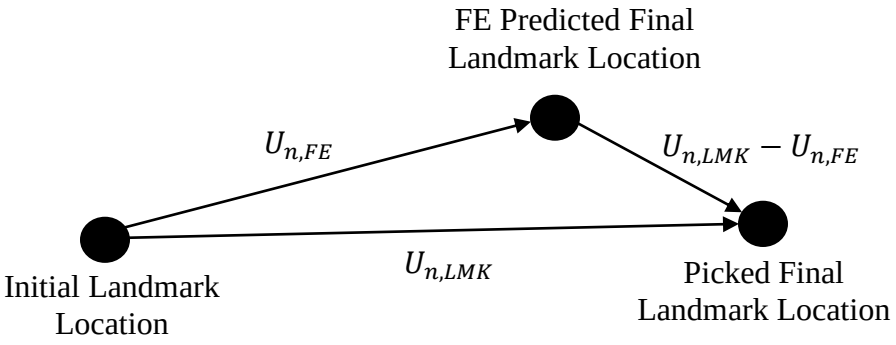

Figure 23: Schematic of landmark error

3.1.8.2 Lobe Weighted Average Landmark Error

The lobe weighted average landmark error, ξ_{LW}, weights the average landmark error of each lobe with equal value. Average landmark error for each lobe is calculated then averaged across all considered lobes, see equation below. Let $U_{n,m,LMK}$ be the displacement vector of the n^{th} landmark in the m^{th} considered lobe determined by landmark picking. Let $U_{n,m,FE}$ be the

displacement vector of the n^{th} landmark in the m^{th} considered lobe determined by finite element simulation.

$$\xi_{LW} = \frac{\sum_{m=1}^{M} \frac{\sum_{n=1}^{N_m} \left| U_{n,m,LMK} - U_{n,m,FE} \right|}{N_m}}{M}$$

Where M is the total number of lobes considered and N_m is the number of landmarks in a given lobe m.

3.1.8.3 Lobe Volume Weighted Average Landmark Error

Lobe volume weighted average landmark error, ξ_{LVW}, weights the average landmark error of each lobe with its volume. Average landmark error for each lobe is calculated followed by a weighted average based on lobe volumes.

$$\xi_{LVW} = \sum_{m=1}^{M} w_m \frac{\sum_{n=1}^{N_m} \left| U_{n,m,LMK} - U_{n,m,FE} \right|}{N_m}$$

Where w_m is the ratio of the volume of lobe m to the entire volume of all lobes in set M.

3.2 Results

Each simulation took between 12 minutes and 2 hours running in parallel across 4 processors. The variation in simulation time depended on the number of iterations to obtain the final solution.

The percentage of simulations that converged is listed in Table 7. 82% of the right lung simulations converged and 94% of the left lung simulations converged.

Table 7: Percent of converged FE solution sets

Subject	Lung Half	Solution Convergence Percentage
1	Right	86%
1	Left	94%
2	Right	73%
2	Left	92%
3	Right	84%
3	Left	91%
4	Right	81%
4	Left	100%
5	Right	88%
5	Left	94%

The data will be presented with a 3D plot. The axes correspond to the three independent variables (E, ν, f) and the color contour represents the dependent variable. The percentage of converged solutions for every parameter combination across all simulation sets is plotted in Figure 24. The scatter points are contoured with the percentage of converged solutions where red represents a low convergence percentage and blue represents a high convergence percentage.

Figure 25 quantifies ξ averaged across all subjects. The results are reported for all simulation sets (both lungs), only left lung simulation sets and only right lung simulation sets. Solutions that did not converge were not considered when averaging for this figure. A black 'X' indicates a parameter combination without a converged solution for any subject.

Figure 26 quantifies ξ_{LW} averaged across all subjects. The results are reported for all simulation sets (both lungs), only left lung simulation sets and only right lung simulation sets. Solutions that did not converge were not considered when averaging for this figure. A black 'X' indicates a parameter combination without a converged solution for any subject.

Figure 27 quantifies ξ_{LVW} averaged across all subjects. The results are reported for all simulation sets (both lungs), only left lung simulation sets and only right lung simulation sets. Solutions that did not converge were not considered when averaging for this figure. A black 'X' indicates a parameter combination without a converged solution for any subject.

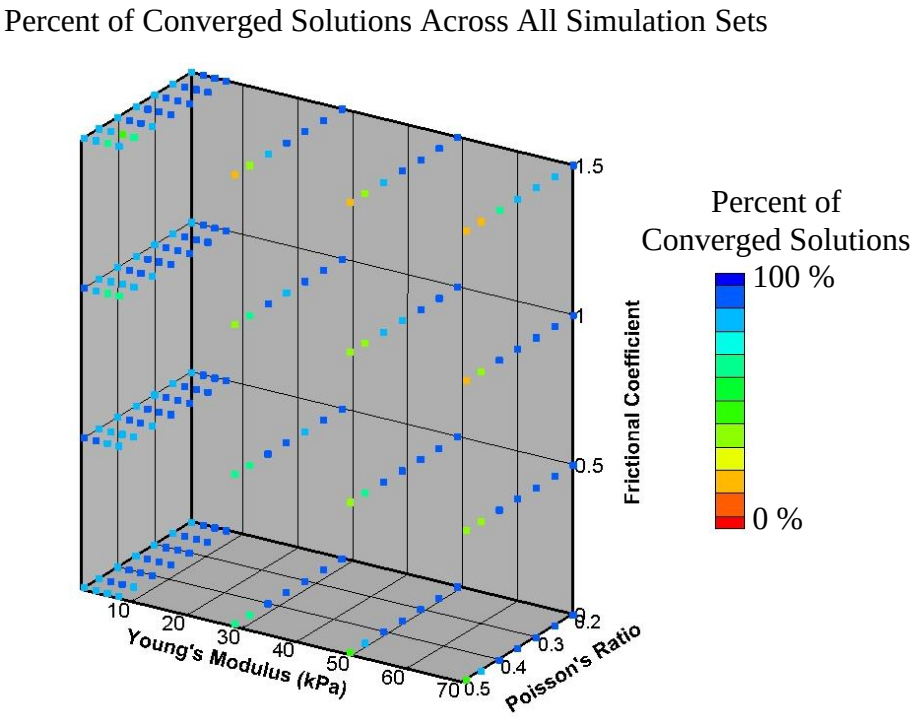

Figure 24: The percent of converged solutions across all subjects for all parameter combinations. 100% indicates all FE simulations for that parameter combination converged while 0% indicates no FE simulations for that parameter combination converged.

The intra-user landmark picking variability was conducted for Subjects 4 and 5. The average landmark picking error was 0.83 mm. The maximum landmark picking error was 10.95 mm. 90% of the landmarks were within 2 mm of the previous pick. A histogram intra-user variability in landmark picking is shown in Figure 28.

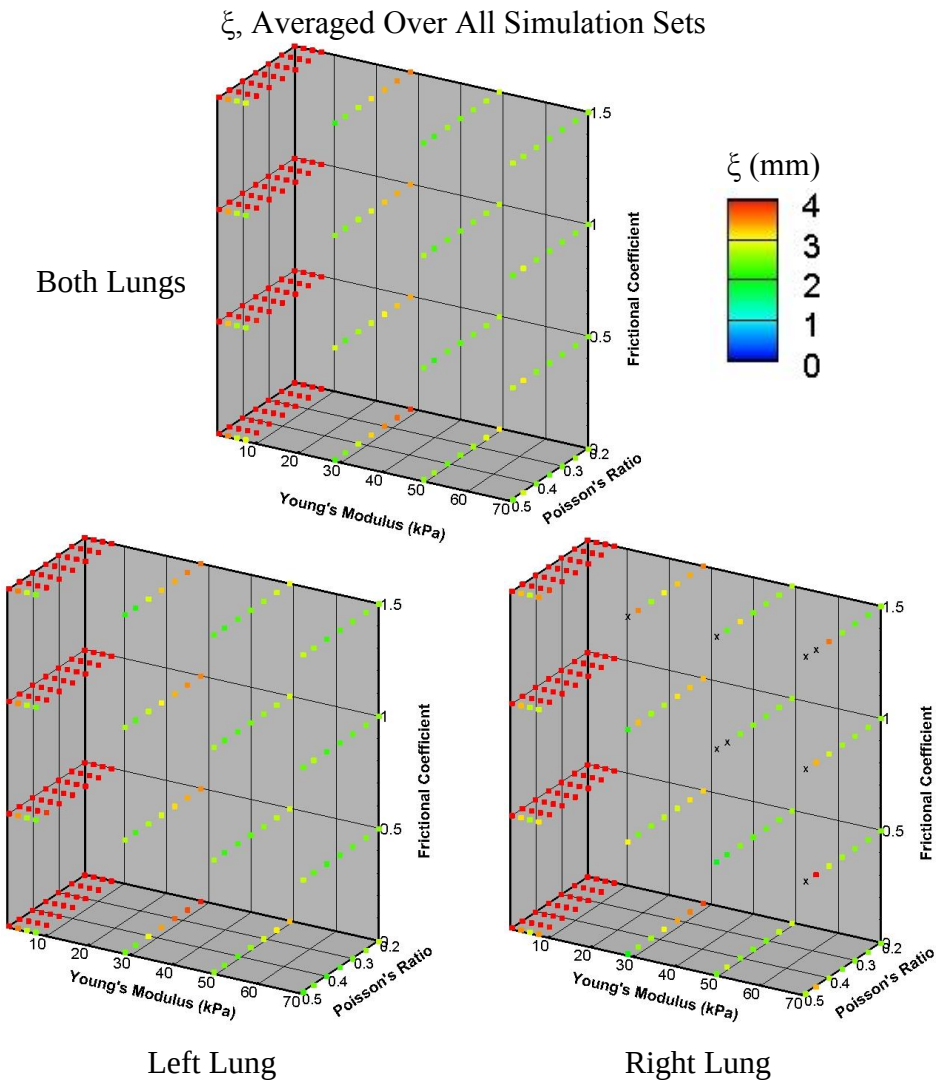

Figure 25: Average landmark error. (top) Average landmark error, averaged across all simulation sets, is shown for every parameter combination. (bottom left/right) Average landmark error, averaged across all left/right lung simulation sets, is shown for every parameter combination.

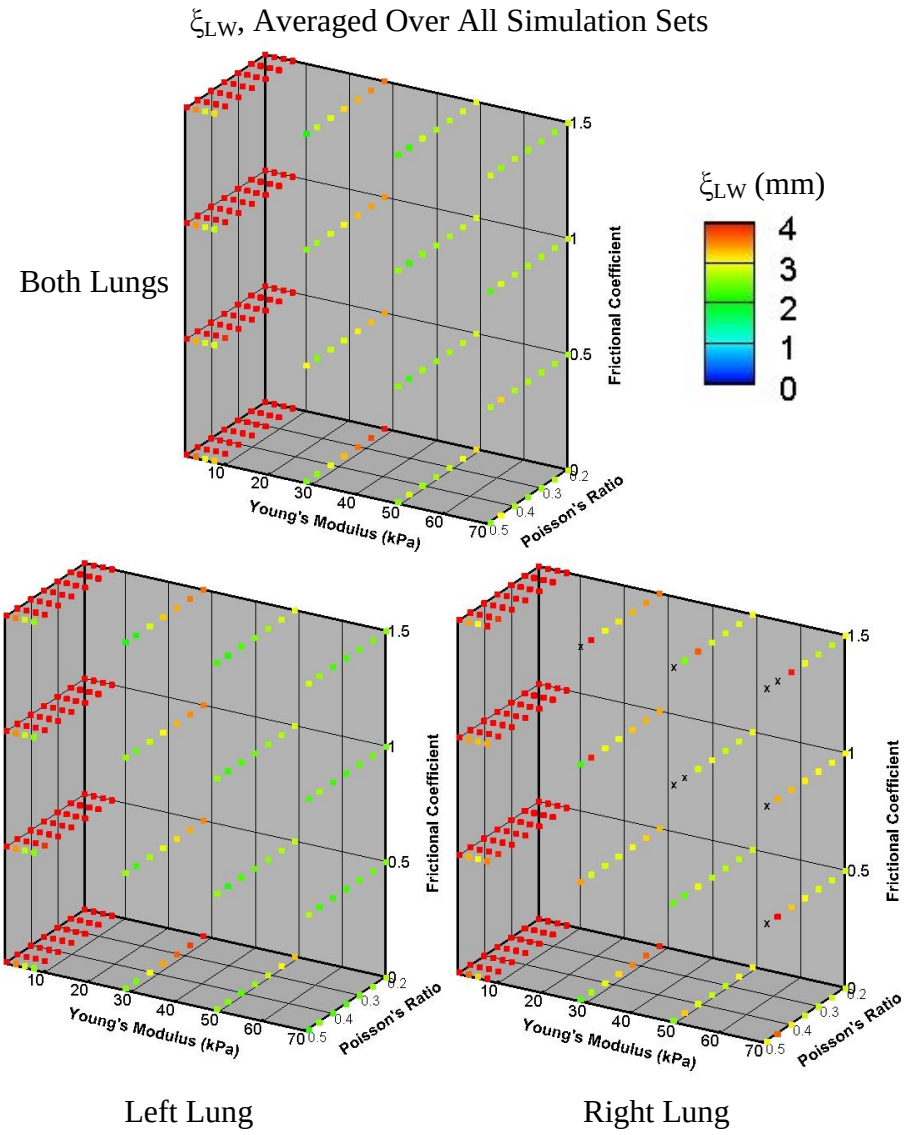

Figure 26: Lobe-weighted average landmark error(top) Lobe weighted average landmark error, averaged across all simulation sets, is shown for every parameter combination. (bottom left/right) Lobe weighted average landmark error, averaged across all left/right lung simulation sets, is shown for every parameter combination.

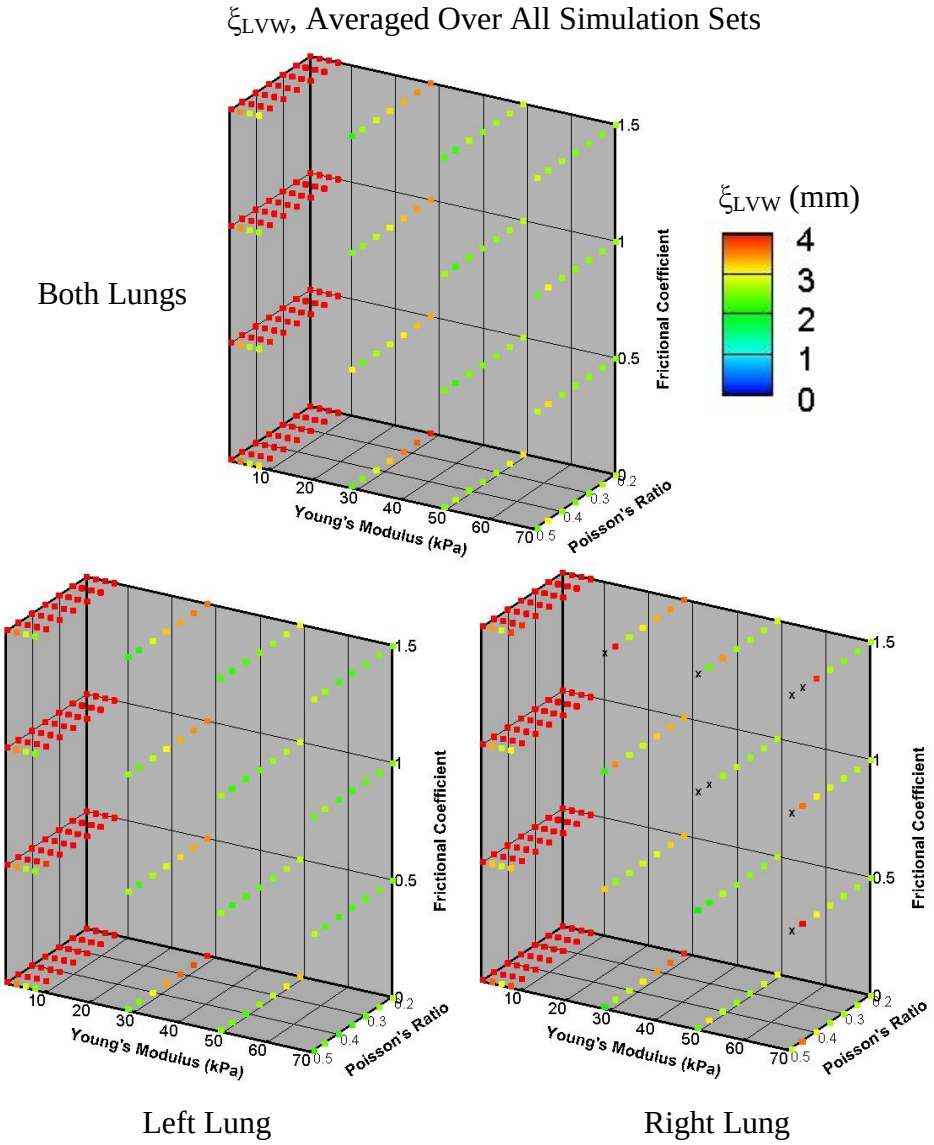

Figure 27: Lobe volume-weighted averaged landmark error. (top) Lobe volume weighted average landmark error, averaged across all simulation sets, is shown for every parameter combination. (bottom left/right) Lobe volume weighted average landmark error, averaged across all left/right lung simulation sets, is shown for every parameter combination.

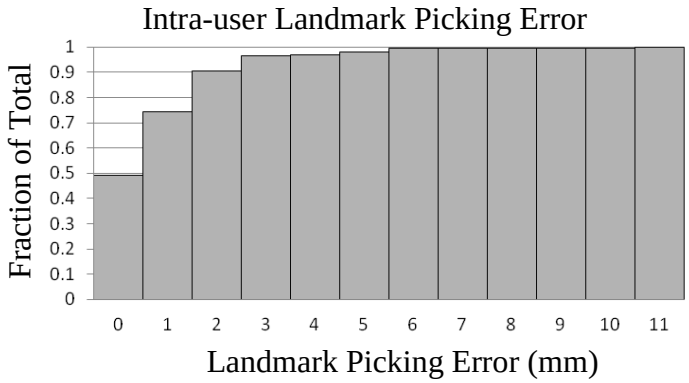

Figure 28: Intra-user landmark picking error for Subjects 4 and 5. Average landmark picking error was 0.87 mm.

3.3 Discussion

In order for FE lung modeling to be effective, a validated, repeatable FE methodology based on the physiology and mechanics of lung deformation must first be developed. Research groups such as Al-Mayah, Werner, Zhang, West and Liu have developed and interrogated FE lung models on issues such as displacement field accuracy [17, 27, 29], gravitational dependence on ventilation [16] and influence of pleural cavity shape change on regional ventilation [62]. All simulations to date have assumed each lung half behaves as a continuum. However, there is a large body of evidence suggesting this assumption is wrong due to sliding between the lobes of the lung during breathing, see Section 2.2 and [4, 55, 56].

Several recent publications acknowledge the potential importance of incorporating lobe sliding in DIR. As the clinical use of image registration to track lung motion expands there becomes a greater emphasis on accuracy. Most analyses of lung motion, be it deformable image registration or finite element simulation, consider the lung as a continuum and smooth out the displacement discontinuity at the fissure boundaries [14, 27, 28, 37, 63-66]. However, some groups are stressing the importance of correctly acknowledging the discontinuity with

physiologically meaningful image registration algorithms. Yin *et al.* developed a registration method that accounts for discontinuities at lobar fissures [26]. The discontinuity in the displacement field was quantified in the method similar to Ding *et al.* [4] and also was confined strictly to the left lung. Modat *et al.* state that their registration algorithm could be improved by accounting for the slipping between the lobes [31].

Though some strides have been made in lobe sliding with DIR, incorporation of lobe sliding in FE models is essentially non-existent. Since FE results are governed solely by the material properties, boundary conditions and initial geometry, it is plausible that incorporation of lobe sliding in FE modeling will have a greater effect on the resulting displacement field compared with incorporation into DIR. The FE paradigm adopted in this chapter introduces a new interpretation to initial geometry and boundary conditions for the incorporation of lung lobe sliding. The methods clearly define the steps to go from 4DCT to working FE model.

Two qualities of a successful FE methodology are a high percentage of converged solutions and solution accuracy. Due to variability in landmark picking, interpretation technique and subject variability, a single 'optimal' combination of ν, E and f cannot be determined. Instead, there is a working range of ν, E and f that offer landmark errors within tolerance and have high percentage of converged solutions. Intra-subject variability in landmark picking helps determine accuracy tolerance. Average intra-subject picking error was 0.87 mm (near image resolution at 1x1x1 mm). This is similar to the landmark picking error reported by Werner *et al.* [27]. Therefore, landmark accuracies within 1 mm landmark error were considered within tolerance as this is on the order of image resolution.

Figure 24 indicates a significant drop-off in percent of simulations converged for $\nu>0.45$. 67% of the solutions converged for $\nu\geq0.45$ compared to 97% converged for $\nu<0.45$. For this reason, Poisson's ratio values of 0.45 and 0.49 were not considered within the working range.

3.3.1 Average Landmark Error, ξ

Average landmark error, ξ, is the traditional metric for assessing error in DIR or FEM related to the lung. ξ for all combinations of material parameters, averaged across all simulation sets, is shown in Figure 25. There is a relationship between ν, E and ξ. ξ significantly increases when E<28kPa. Values of E>28kPa all have low ξ, independent of ν. When E=28kPa, ξ depends on the value of ν; higher ν results in lower ξ. Internal energy increases with increasing ν and E, therefore, ξ appears correlated to the internal energy of the system. This concept is demonstrated by plotting the relationship between κ, μ, f and ξ, Figure 29. Higher κ and μ indicate more energy necessary to deform into the final configuration, verified by the role of each value in the Neo Hookean strain energy density function. Parameter combinations with high ξ are focused near κ=0 and μ=0.

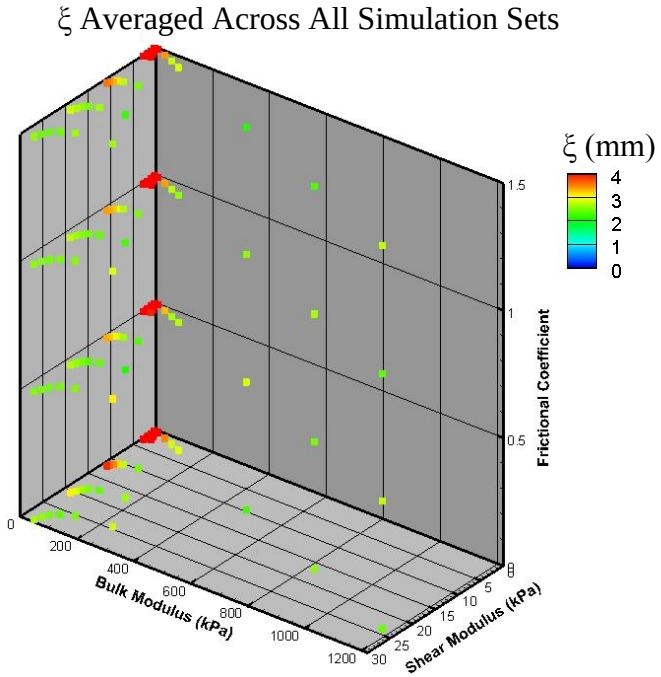

Figure 29: Average landmark error, average across all simulation sets, plotted against shear modulus, bulk modulus and frictional coefficient. Average landmark error increases as bulk modulus and shear modulus simultaneously approach zero.

Figure 25 suggests ξ was independent of friction. For further clarity, ξ averaged across all simulation sets is plotted using flood fill for f=0 and f=1.5, Figure 30. This figure illustrates the fact that friction has a nearly negligible contribution to changes in ξ.

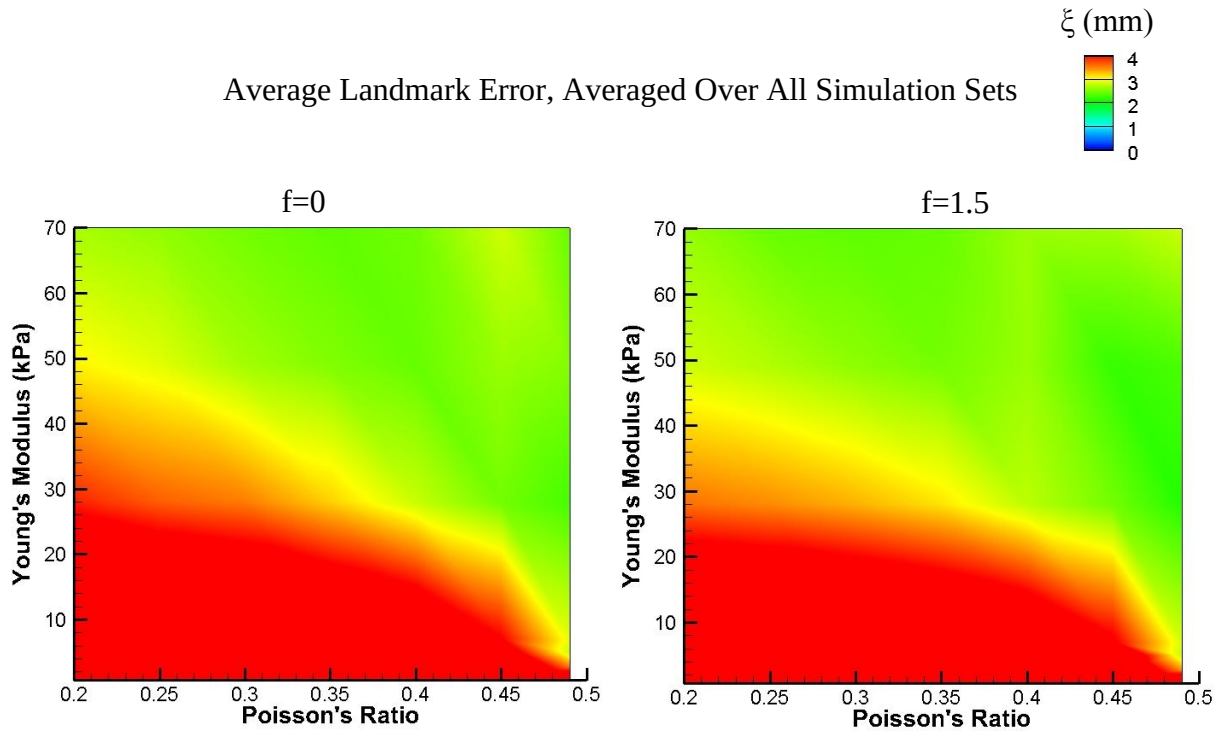

Figure 30: Average landmark error is plotted with flood fill contour for all combinations of Young's modulus and Poisson's ratio, but only for f=0 (left) and f=1.5 (right). The plots illustrate minimal influence of frictional coefficient on changes in average landmark error

The lowest value of ξ averaged across all simulation sets was 2.14 mm which occurred at ν=0.49, E=28kPa, f=1.5. Figure 31A shows the original results while Figure 31B illustrates all parameter combinations within 1 mm ξ (a black 'X' indicates ξ > 3.14 mm). All combinations of 0.45 and 0.49 were omitted due to convergence issues. This threshold suggests an acceptable

region when E>=49 kPa. When E=28 kPa, the solution is generally within tolerance when ν>=0.35.

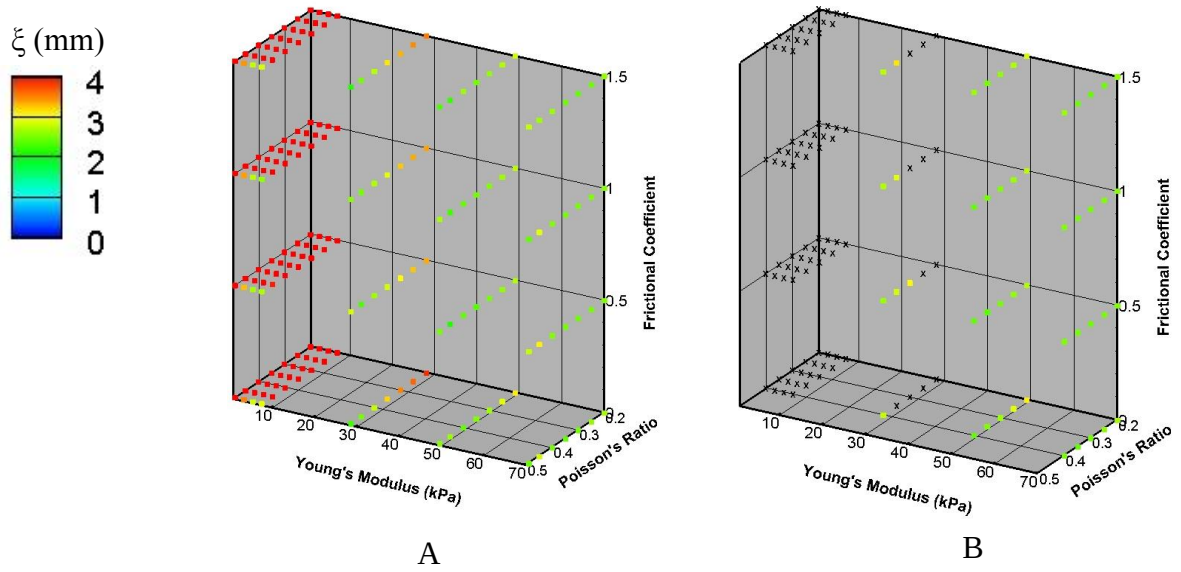

Figure 31: Illustration of the acceptable region for E, ν and f evaluated using average landmark error. (A) Average landmark error, averaged across all subjects, plotted for all input parameter combinations. (B) Only parameter combinations within 1 mm average landmark of the best simulation (<3.14 mm) are plotted with contour; the remaining parameter combination points are represented with a black 'X'. All parameter combinations with Poisson's ratio greater than 0.45 were omitted due to a low percentage of converged solutions.

Validation of DIR and FEM of the lung in literature almost exclusively uses landmark error. Landmark error is only a good metric if landmarks are evenly distributed throughout the lung and represent the entire underlying displacement field including away from landmarks. In the lung, landmarks are chosen at vessel bifurcations which tend to focus on regions where the vessels are well defined. These tend to be located medially. Furthermore, landmarks are not distributed equally between lobes, or even a function of lobe volume, refer to Table 5. To compensate for potentially poor landmark distribution, two additional error metrics were introduced and evaluated. Lobe weighted average landmark error, ξ_{LW}, weights the average

landmark error of every lobe equally. Lobe volume weighted average landmark error, ξ_{LVW}, weights the average landmark error of every lobe by its volume.

3.3.2 Lobe Weighted Average Landmark Error, ξ_{LW}

This is a novel index being reported for the first time. ξ_{LW} compensates for this by calculating the average landmark error for each lobe, then average those values. The result is an average landmark error where each lobe receives the same weight, regardless of the number of landmarks contained within the lobe. This landmark-based metric is appropriate if the displacement field accuracy of each lobe is considered equally important.

The lowest value of ξ_{LW} was 2.09 mm. Analysis of ξ_{LW} results in the same conclusions as ξ. There is a correlation between ν, E and ξ_{LW} while ξ_{LW} is independent of f. Figure 32A summarizes ξ_{LW} averaged across all subjects while Figure 32B displays only values of ξ_{LW} within 1 mm of the optimal (a black 'X' indicates ξ_{LW} > 3.09 mm).

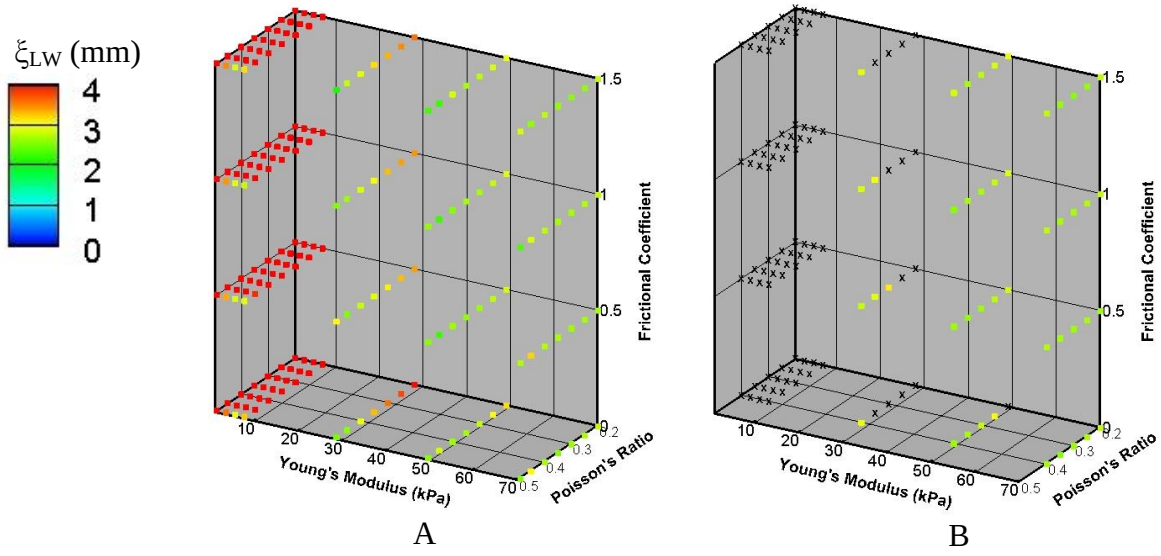

Figure 32: Illustration of the acceptable region for E, ν and f evaluated using lobe-weighted average landmark error (A) Lobe weighted average landmark error, averaged across all subjects, plotted for all input parameter combinations. (B) Only parameter combinations within 1 mm lobe weighted average landmark of the best simulation (<3.09 mm) are plotted with contour; the remaining parameter combination points are represented with a black 'X'. All parameter combinations with Poisson's ratio greater than 0.45 were omitted due to a low percentage of converged solutions.

3.3.3 Lobe Volume Weighted Average Landmark Error, ξ_{LVW}

This is a novel index being reported for the first time. ξ_{LVW} provides a slight variation on ξ_{LW}. Instead of weighting each lobe equally, the lobes are weighted by the lobe's fractional volume at EI. This way, lobes that make up a larger portion of the lung contribute more to ξ_{LVW}. This metric may be necessary if landmarks are bunched together in an individual lobe.

Figure 33A summarizes ξ_{LVW} averaged across all subjects while Figure 33B displays only values of ξ_{LVW} within 1 mm of the optimal (a black 'X' indicates ξ_{LVW} > 3.15 mm).

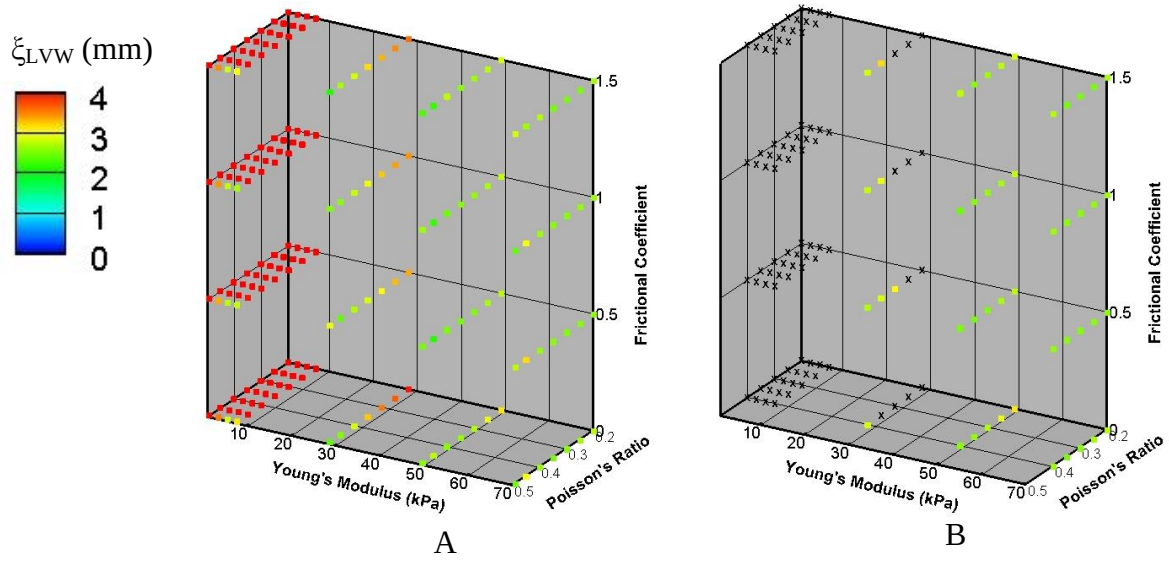

Figure 33: Illustration of the acceptable region for E, ν and f evaluated using lobe volume-weighted average landmark error (A) Lobe volume weighted average landmark error, averaged across all subjects, plotted for all input parameter combinations. (B) Only parameter combinations within 1 mm lobe volume weighted average landmark of the best simulation (<3.15 mm) are plotted with contour; the remaining parameter combination points are represented with a black 'X'. All parameter combinations with Poisson's ratio greater than 0.45 were omitted due to a low percentage of converged solutions.

Theoretically, ξ_{LW} and ξ_{LVW} compensate for the non-equal distribution of landmarks as observed in Table 5. The fact that the new indices lead to the same conclusion indicate that the landmarks are evenly distributed enough that further compensation was unnecessary.

3.3.4 Qualitative Assessment of Parameter Perturbation

The values of ν, E and f all qualitatively affected the behavior of the model. To understand how ν and E influence the model, it is beneficial to understand the relationship between ν, E, μ and κ. This is because μ and κ have clear physical meanings within the Neo Hookean model as well as clear physical meaning. κ quantifies the amount of energy necessary to change the volume of an element. It is associated with the volumetric parameter of the Neo Hookean model. μ quanifies the amount of energy necessary to deform an element in shear (change in shape).

Poisson's ratio increases with increasing κ and increases with decreasing μ. Therefore, a higher Poisson's ratio will have a propensity to change in shape (lower μ) rather than change in volume (higher κ). Conversely, a lower Poisson's ratio will have more of a propensity to change in volume than change in shape. These trends are reflected in the models. Figure 34 shows a displacement vector magnitude contour for the right lung of Subject 4 for the two extremes of ν. At higher ν, the lobes squeeze together in attempt to completely fill the pleural cavity volume. At lower ν, the lobes would tend to pull away from each other and the pleural cavity. This phenomenon is subtle and highlighted in Figure 34 with arrows. Note that despite the differences in the displacement contours, the landmark errors for the models in Figure 34 were within 1 mm tolerance (ξ differed by 0.80 mm).

If κ and μ are both increased by a constant t, then E will increase by that same constant t, where ν will remain unchanged. This indicates E alters the amount of energy required to deform the tissue. In the model, lower E had a negative effect on the model, illustrated in Figure 35. The lobes pull away from each other (Figure 35, arrows) at the lobe boundaries and deformation is confined near the surface driving the deformation. Higher E resulted in a more uniform deformation field. The landmark error for the models in Figure 35 differed by 4.67 mm.

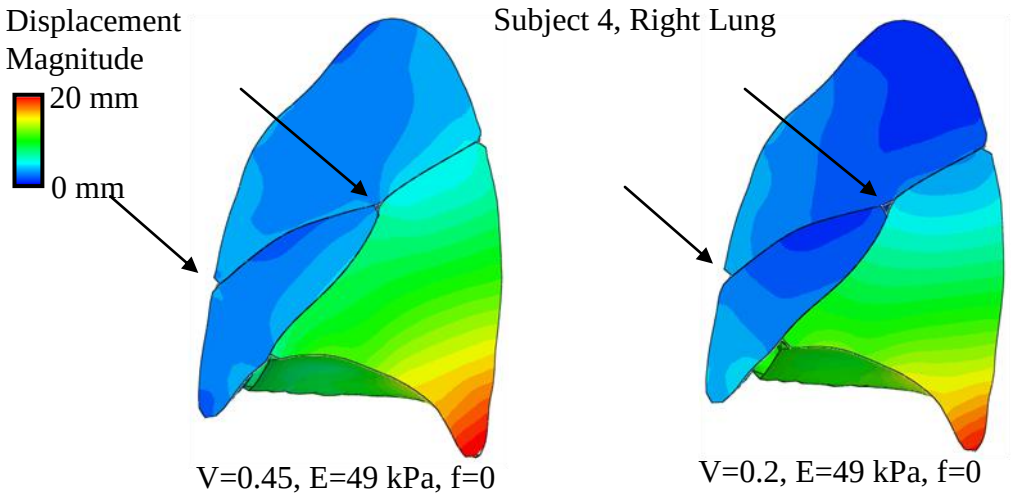

Figure 34: Displacement magnitudes on a roughly saggittal slice illustrating the qualitative influence of Poisson's ratio on the displacement field output of lobe sliding FE. A low Poisson's ratio resulted in slight separation of the lobes, highlighted with arrows, though the result is subtle.

Increasing the frictional coefficient limited the lobes from sliding relative to each other. Sliding can be observed by the difference in displacement magnitude contour values at the lobe boundaries, Figure 36. In these two models, landmark error differed by only 0.13 mm, though clear differences in the displacement fields exist, particularly in the RML. At low f, the RML translates ventrally as it is forced out from between the RUL and RLL. At high f, the RML sticks to the RLL resulting in more superior-dorsal motion.

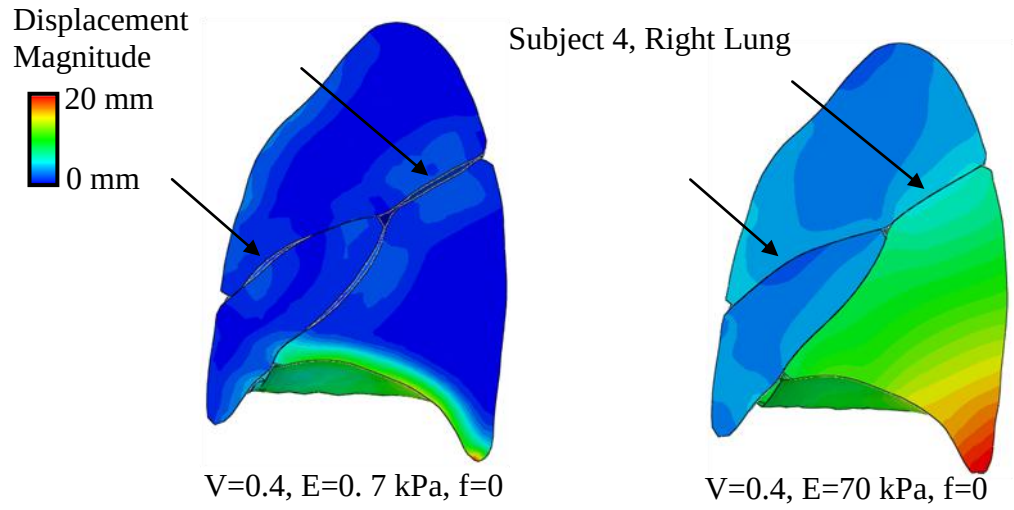

Figure 35: Displacement magnitudes on a roughly saggittal slice illustrating the qualitative influence of Young's modulus on the displacement field output of lobe sliding FE. Low Young's modulus resulted in major separation of the lobes, highlighted with arrows. At low Young's modulus deformation was concentrated near the diaphragm, which was primarily driving deformation.

3.3.5 Further Quantitative Analysis

Figure 36 illustrates that friction does affect on the underlying displacement field without changing average landmark error. A more in-depth quantitative analysis reveals what is going on. Figure 37 stratifies landmark error by lobe. RML landmark error improves with lower friction while RLL landmark error improves at higher friction. The ventral motion at low friction improves landmark error in the RML. This improvement in ξ is mitigated by the loss of average landmark accuracy in the RLL at low friction. In the left lung, the LLL landmark error improves slightly at lower friction. Both upper lobes are virtually unaffected by friction.

A paired t-test was conducted for each lobe across all data sets. The statistical variables were f=0 and f=1; ν and E were held constant at 0.35 and 70 kPa respectively. Friction did not affect average landmark error of any lobe with statistical significance ($p>0.05$). It was found, however, that the upper lobes performed significantly better than the lower lobes at ν=0.35 and

E=70 kPa. A paired t-test for f=0 and f=1 resulted p=0.0005 and p=0.001 respectively. This may be attributed to relatively small landmark displacements in these lobes.

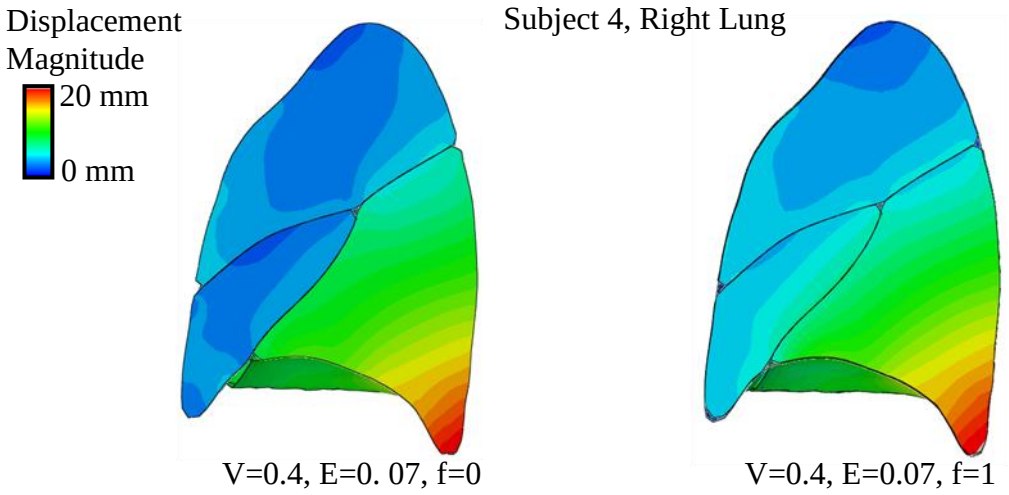

Figure 36: Displacement magnitudes on a roughly saggittal slice illustrating the qualitative influence of inter-lobar frictional coefficient on the displacement field output of lobe sliding FE. A low inter-lobar frictional coefficient resulted in sliding between the lobes; illustrated by the discontinuity in the contour plot at the lobe boundaries. A high inter-lobar frictional coefficient nearly eliminated sliding at the lobe boundaries; illustrated by the approximate continuity in the displacement magnitude contour across lobe boundaries.

Werner *et al.* compared FE accuracy near and away from lung tumors [67]. Werner found that, on average, landmark error was 3.1 mm over the entire lung with a 4.2 mm landmark error near the tumor. The tumor was not modeled differently than healthy parenchyma. This suggested that the tumor may have significantly different material properties than healthy parenchyma and affects how the lung deforms near the tumor. In this study, lung halves containing tumors did not perform differently with any statistical significance ($p>0.05$). However, this was a poor data set to evaluate the role of tumors in lobe sliding FE accuracy as the tumors were located in the upper lobes in all subjects considered. A better data set would focus on tumors located in the lower

lobes where more deformation would likely result in the stiffer tumor having a greater influence on deformation.

There is a degree of subjectivity in the segmentations for this study. Automatic lobe segmentation of 4DCT does not exist, so manual segmentation was used. A step-by-step algorithm was developed to help minimize subjectivity. However, fissure locations were not always clear, particularly at the RUL-RML boundary, resulting in potential disagreements in fissure location. Different interpretations of fissure location may have a significant effect on the FE solution. For this reason, an automatic lobe segmentation algorithm capable of segmenting 4DCT images is desired.

Smoothing at all levels in this study was consistent across all subjects, though the degree of smoothing was arbitrarily defined. A degree of smoothing that eliminates small features in both the model geometries and pleural cavity displacements while retaining overall model shape was desired. Figure 38 compares a sample RPC representation across three stages of the process: original segmentation, segmentation smoothed at image level, final FE mesh. Figure 39 compares a sample right lung lobe segmentations and corresponding final FE mesh. Although arbitrarily defined, the smoothing algorithm retains the overall geometry of the pleural cavity and lobes.

There is a cavity in the original whole lung segmentation where the pulmonary artery and vein enter the lung. This cavity does not exist in any FE lung models in literature and was manually filled in for this study as it caused FE solution convergence difficulties, see Figure 22. However, this cavity is not lung and may not correctly be assigned to any lobe. It is unclear how filling of this cavity, as corresponding lobe assignment, influences FE results. The lobes of the lung are thought to be mechanically joined near the mediastinum or carina by the airways and blood vessels; this corresponds to the region within the cavity. This is supported by the lack of sliding near the mediastinum or carina reported in Section 2.2. No inter-lobar connections other than friction were employed in this study. Future studies may want to focus on FE with the

cavity or a novel boundary condition in this region to account for the fact that the lobes may be loosely connected within this region.

3.3.6 Limitations

A homogeneous, isotropic material model was used. Lung parenchyma is the lumping of airways, blood vessels and connective tissue and, therefore, is neither homogeneous nor isotropic. Experimental determination of relative lobar material properties, much less sub-lobar, in live subjects is not available. Incorporation of such information may significantly improve results. For this study, a hyperelastic material model was used desired since large deformations were modeled. The simplest hyperelastic model is the Neo Hookean model with two material parameters. Conveniently, the Neo Hookean material parameters have clear correlations to shear modulus and bulk modulus at infinitesimal strains. This provided a good basis to correlate the reported values for E and ν to a hyperelastic constitutive model. The working range of material parameters determined in this study is not meant to represent the material parameters of actual lung parenchyma. The FE lung model developed in this study is an analog of a real lung with many assumptions. Therefore, the optimal material parameters and frictional coefficient should be interpreted as the optimal parameters for this FE paradigm that are applicable across a large subject population.

The lobes in this study interacted solely by surface contact and friction. In reality, the lobes are thought to be loosely connected at the mediastinum and carina by the vessel and airway trees, respectively [4]. The connection was not considered in this model to limit the number of test variables, though modeling this connection is not difficult. Enforcing such a connection would limit the degree of lobar translation and may increase the degree of lobar rotations, consistent with Rodarte *et al.* [38]. An improvement on the model presented may include a boundary condition consistent with the mediastinum and/or carina.

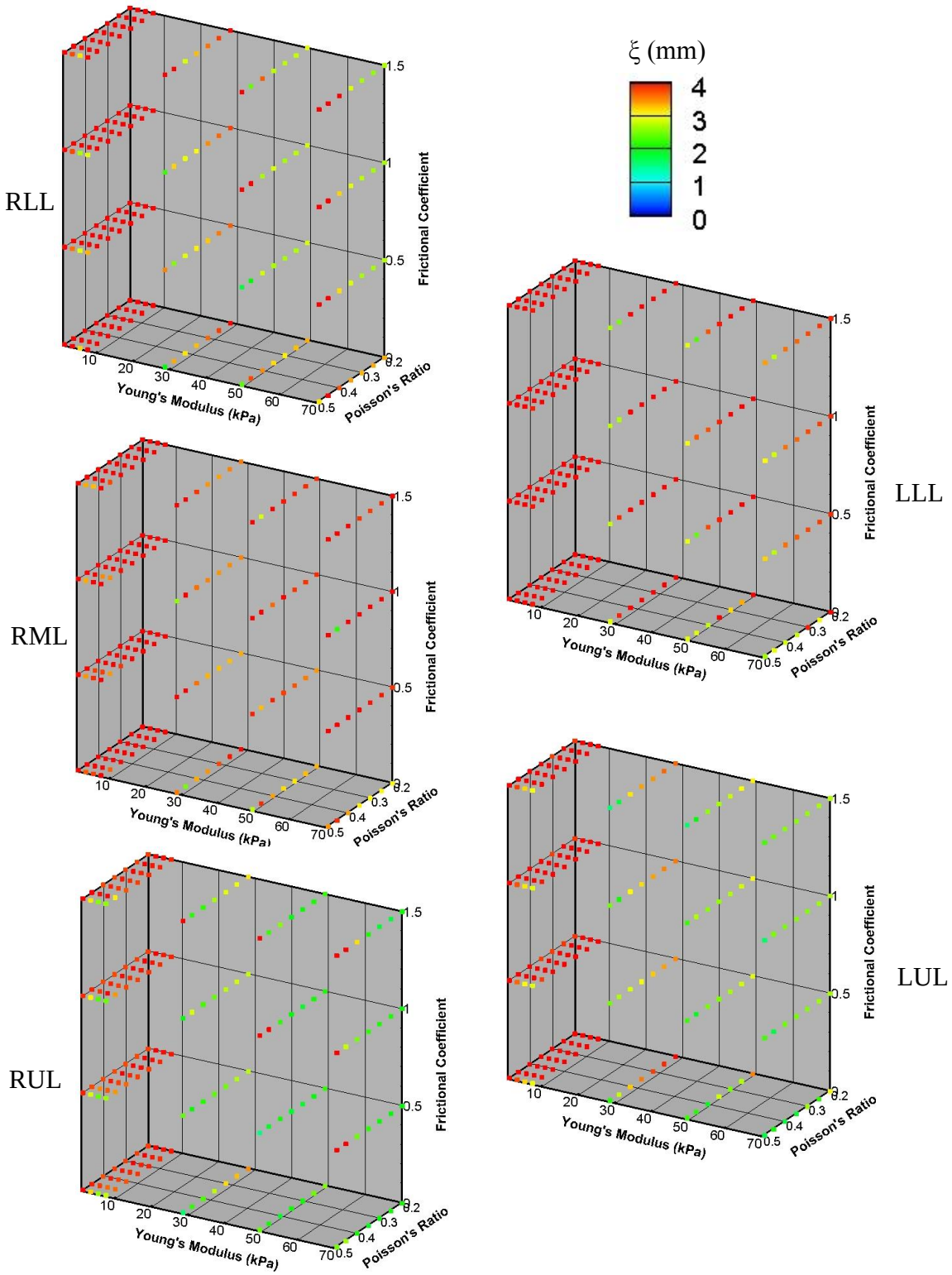

Figure 37: Quantification of average landmark error, averaged across all subjects and stratified by lobe, for all parameter combinations.

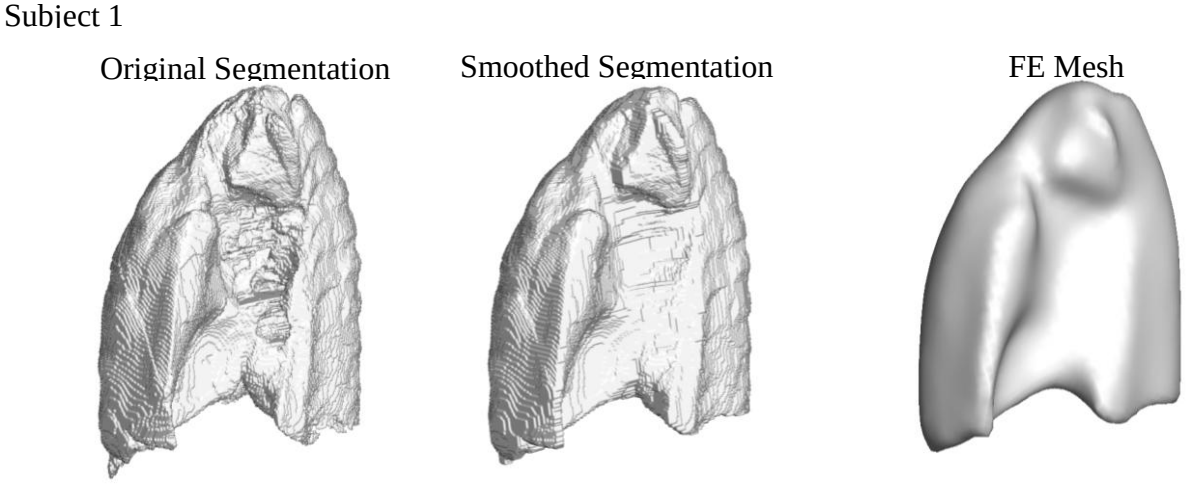

Figure 38: Illustration of the amount of smoothing used to obtain the pleural cavity mesh. (left) The original segmentation. (middle) The segmentation after manually filling of the cavity formed by the pulmonary artery and vein and erosion-dilation smoothing. (right) Surface representation of the initial FE pleural cavity geometry

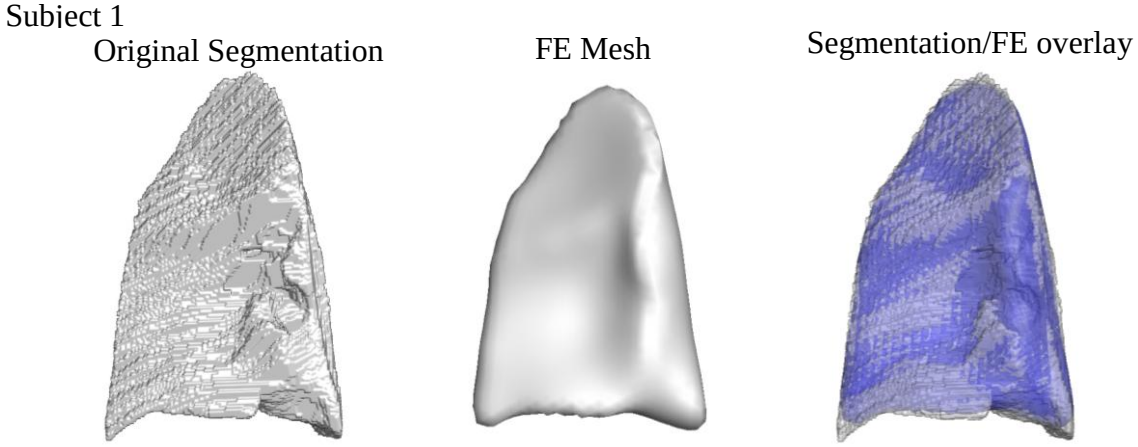

Figure 39: Illustration of the amount of smoothing to obtain the lobe meshes. The right lower lobe for Subject 1 is shown. The smoothing eliminates small surface features while preserving the original overall lobe geometry. (right) An overlay of the FE mesh and original lobe segmentation.

West et al. demonstrated the influence of gravity on FE models associated with the lung [16]. Gravitational forces were not included in this model. The inclusion of gravity would increase the assumptions of the model. For gravity to be included correctly, tissue density, lobe boundary conditions and material properties must be correctly modeled. Tissue density is easily obtained from CT scans. However, as per the mediastinum and carina, lobe boundary conditions are likely not entirely correct. Also, lung material properties are non-linear, which is thought to play a role in the gravitational dependence of volume change [1]. It would be prudent to first understand the role of material properties and boundary conditions associated with the model prior to the inclusion of gravity.

3.4 Conclusion

A clear, repeatable methodology was developed for FE modeling of lung deformation with the inclusion of lobe sliding. A clear working range for E (>49 kPa) and ν (<0.45) was identified for acceptable percentage of converged solutions and landmark errors within the defined tolerance of 1 mm. Friction had a negligible effect on all landmark-based error metrics. However, further qualitative and quantitative assessment confirms that friction does affect the results. In particular, allowing sliding increased landmark accuracy in the RML while limiting sliding increased landmark accuracy in the RLL.

CHAPTER 4: SIGNIFICANCE OF LOBE SLIDING IN LUNG FINITE ELEMENT MODELING (FEM)

Chapter 3 demonstrated that lobe sliding finite element (FE) modeling with no inter-lobar friction yields landmark errors similar to lobe sliding FE with high inter-lobar friction. Although average landmark error is generally unaffected, the displacement fields are different. The difference was quantitatively demonstrated with improved landmark error in the RML at low inter-lobar frictional coefficients and improved landmark error in the RLL at high inter-lobar frictional coefficients, Figure 37. The difference was also qualitatively assessed in the displacement fields, Figures 36. The lack of statistical differences in average landmark error between high friction lobe sliding and low friction lobe sliding models may be attributed to the tidal breathing data set. Of the subjects considered, volume change increased by only 15.8%, on average, between EE and EI. The relatively small amount of deformation may limit the significance of lobe sliding in FE lung models. To better understand the role of lobe sliding in lung FEM, scans spanning functional residual capacity (FRC) to total lung capacity (TLC) may be considered. The volume change increase between FRC and TLC is typically closer to 80%, roughly 5x the deformation experienced in tidal breathing. Larger deformation may result in increased sliding and, consequently, its influence on the final displacement field may be magnified. This chapter leverages the findings in Chapter 3 to model and assess the role of lobe sliding in lung deformation by modeling FRC-TLC of healthy human subjects from static CT scans.

4.1 Methods

4.1.1 Subject Demographics

The data set used in this study is the same as that reported on in Sections 2.1 and 2.2. All data were gathered under a protocol approved by our institutional review board. Pairs of volumetric CT data sets from six normal human subjects in supine orientation were used in this

study. Of the six subjects, four were male and two were female. Subject age ranged from 22-37 years with a mean of 27.3 years. The six patients were non-smokers with no recorded exclusion criteria (recent respiratory infection, medication other than contraception, cardiopulmonary abnormalities, pregnancy or breast feeding, diabetes mellitus, positive PPD or history of tuberculosis, CT scan within the last year). Each image pair was acquired with a Siemens Sensation 64 multi-detector row CT scanner (Forchheim, Germany) during breath-holds near FRC and total lung capacity (TLC) in the same scanning session. Voxel dimensions were approximately 0.6x0.6 mm in the axial plane with a section spacing of 0.5 mm along the longitudinal axis.

The parenchyma was segmented using Hu *et al*.[45], followed by an automatic lobe segmentation algorithm defined by Ukil *et al.* [46]. Modification of the whole lung segmentation followed the same procedure outlined in Chapter 3, which included separation of the left and right lung segmentations, manual filling of the cavity formed by the pulmonary artery and vein, and smoothing with dilation and erosion. An automatic filling algorithm, outlined in Appendix A, expanded to lobe segmentation volumes to fill the modified whole lung segmentation.

FRC volume information is listed in Table 8. Volume change information for all data is summarized in Table 9.

Table 8: Lobe volumes and total volumes for all subjects in the study population measured from the volume of the lobe segmentations.

Lobe Volumes at FRC (L)						
Subject	RLL	RML	RUL	LLL	LUL	Total
1	0.70	0.38	0.61	0.67	0.84	3.20
2	0.80	0.38	0.54	0.91	0.76	3.39
3	0.64	0.33	0.57	0.69	0.69	2.92
4	0.72	0.23	0.43	0.63	0.66	2.67
5	0.88	0.44	0.73	0.74	0.97	3.76
6	0.75	0.33	0.71	0.72	0.84	3.35

Table 9: Lobe volume change and total volume change for the subject population measured using the volume change of the lobe segmentations.

Volume Change (Jacobian)						
Subject	RLL	RML	RUL	LLL	LUL	Total
1	2.27	1.58	1.79	2.34	1.77	1.98
2	2.05	1.45	1.64	1.84	1.51	1.74
3	2.06	1.45	1.67	1.98	1.65	1.80
4	2.08	1.55	1.78	2.07	1.70	1.89
5	2.20	1.46	1.63	2.31	1.68	1.89
6	2.52	1.65	1.84	2.64	1.85	2.15
Average	2.20	1.69	2.20	1.52	1.73	1.91

Landmarks were selected using the same semi-automatic picking method presented in Chapter 3. The distribution of picked landmark locations is summarized in Table 10. Average picked landmark displacements are listed in Table 11.

Table 10: Number of landmarks per lobe for the subject population.

Landmark Distribution						
Subject	RLL	RML	RUL	LLL	LUL	Total
1	37	16	34	32	31	150
2	51	15	19	38	41	164
3	30	17	34	40	39	160
4	45	5	14	18	23	105
5	64	16	32	51	43	206
6	42	10	29	43	45	169

Table 11: Landmark displacements quantified by the difference in picked landmark locations in the FRC and TLC images.

Average Picked Landmark Displacements						
Subject	RLL	RML	RUL	LLL	LUL	Average
1	35.5	24.4	16.1	35.4	19.0	26.5
2	43.6	19.1	17.7	35.0	13.2	28.8
3	38.5	21.0	12.1	38.3	15.1	25.3
4	32.2	20.5	12.7	35.6	13.5	25.5
5	39.4	19.5	12.3	39.1	19.8	29.5
6	44.9	25.9	13.5	45.2	18.9	31.5
Average	39.0	25.9	14.1	38.1	16.6	27.8

4.1.2 Lobe-by-Lobe Image Registration

To allow for the discontinuity at the lobe boundaries caused by lobe sliding, lobe-by-lobe DIR was used; see Section 2.2. Briefly, the masked lobe volumes were independently registered to ensure no inter-lobar contributions to the similarity metric as well as no regularization across the lobar boundaries. Linear elastic image registration, parameterized by a uniform cubic B-spline function, was used to register the FRC-TLC image pairs. The cost function minimized the sum of squared tissue volume difference [23] while incorporating a Laplacian smoothing filter. Detailed information on the registration process may be found in Cao *et al*. [25]. After registration, the resulting displacement fields for each subject were combined into a single image for analysis.

4.1.3 Lobe Sliding FEM

The protocol from lobe segmentations to FE model was the same as that outlined in Section 3.1. Briefly, the left and right lungs for every subject were modeled in separate simulations. Finite element meshes of each lobe and pleural cavity at TLC was constructed according to the procedure outlined in Appendix B. For more information the development of lobe sliding models see Section 3.1.

A frictionless boundary condition was enforced between the lobe surfaces and the inside surface of the pleural cavity. A contact boundary condition was enforced at every lobe-lobe surface. The frictional coefficient at lobe-lobe interfaces was set to f=0 for the frictionless case and f=1.5 for the high friction case. For clarity, let FE_0 refer to a lobe sliding FE model with f=0 and $F_{1.5}$ refer to a lobe sliding FE model with f=1.5. Material properties were defined using the Neo Hookean model with an equivalent infinitesimal Young's modulus value of 70 kPa and Poisson's ratio of 0.35; these values are within the acceptable range defined in Chapter 3. The conversions from equivalent Young's modulus and Poisson's ratio values to Neo Hookean input parameters are outlined in Section 3.1. Displacement boundary conditions were defined at every node in the pleural cavity meshes. Displacements were interpolated from SSD registration of the TLC whole lung segmentation to the FRC whole lung segmentation. All rotational degrees of freedom in the pleural cavity meshes were set to zero.

4.1.4 Whole Lung FEM

Whole lung FE modeling was similar to that reported by Al-Mayah [29]. For clarity, whole lung FE will be referred to as FE_{WL}. The left and right lungs for every subject were modeled in separate simulations. The pleural cavity representations were identical to lobe sliding FEM. A whole lung mesh was obtained by volumetric meshing of the pleural cavity representations with 4-noded tetrahedral elements in Gambit. A frictionless boundary condition was enforced between the whole lung mesh and the pleural cavity mesh. Material properties were defined using the Neo Hookean model with an equivalent infinitesimal Young's modulus value of 70 kPa and Poisson's ratio of 0.35.

4.2 Results

Average landmark error, averaged across all simulations, were FE_0=6.18 mm, $FE_{1.5}$=5.95 mm, and whole lung FE =6.16 mm. FE_{WL} resulted in average landmark error significantly higher than $FE_{1.5}$ ($p<0.001$); no other pairs of simulations were statistically different ($p>0.05$). The results for all simulations are plotted in Figure 40.

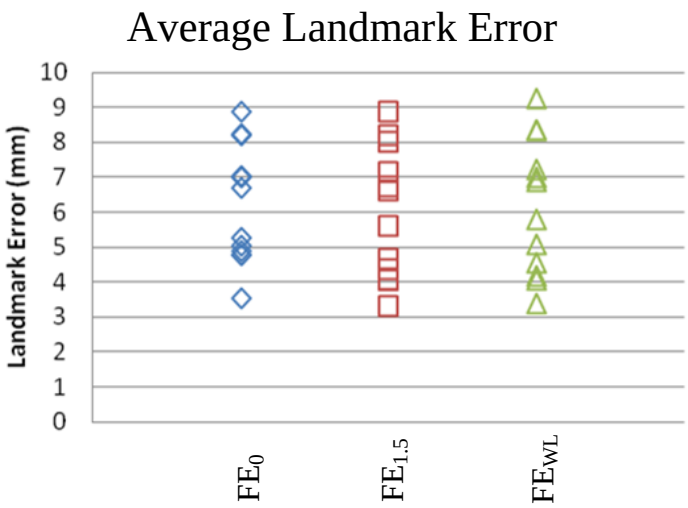

Figure 40: Average landmark error plotted for FE_0, $FE_{1.5}$ and FE_{WL} all simulations. A statistical improvement in average landmark error was found between $FE_{1.5}$ and FE_{WL}.

Average landmark errors for FE_0 and $FE_{1.5}$, stratified by lobe, are listed in Figure 41. Average landmark error was significantly lower in the LLL and RLL for FE_0 than $FE_{1.5}$. Conversely, average landmark error was significantly lower in the LUL and RUL for $FE_{1.5}$ than FE_0. No statistically difference was found for the average landmark error in the RML, though average landmark error in the RML was lower for $FE_{1.5}$.

The displacement fields from FE_0, $FE_{1.5}$ and FE_{WL} were compared with the displacement field from lobe-by-lobe DIR. Nodal displacements from FE_{WL}, FE_0 and $FE_{1.5}$ were interpolated to TLC voxel locations. To preserve sliding characteristics, interpolation occurred on a lobe-by-lobe basis. This means the nodal displacements for a given lobe were interpolated to the voxels of the corresponding lobe segmentation. The average difference in voxel displacements between lobe-by-lobe DIR and FE_{WL}, FE_0 and $FE_{1.5}$ are listed in Table 12. None of the FE methods resulted in displacement fields statistically more similar to the lobe-by-lobe DIR predicted displacement field ($p>0.05$).

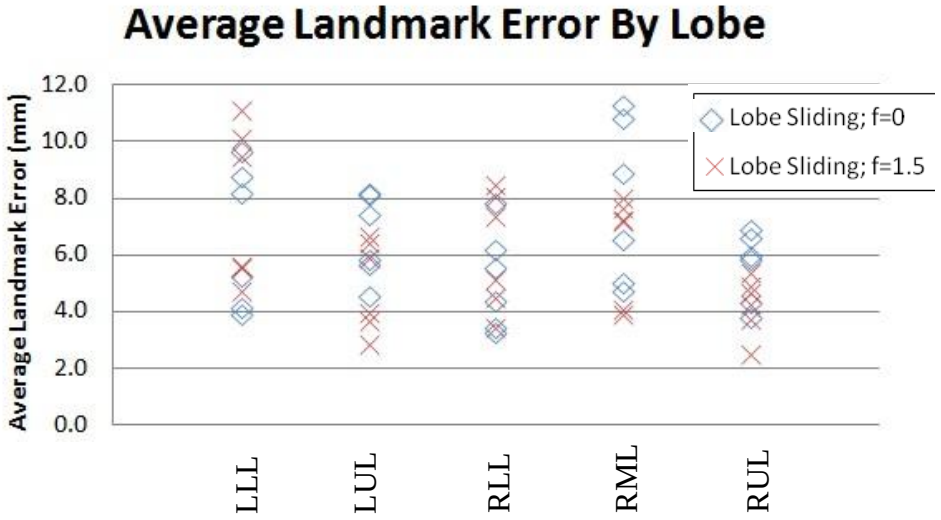

Figure 41: Average landmark error for FE_0 and $FE_{1.5}$ stratified by lobe for all simulations.

Table 12: The average difference in voxel displacement estimated by lobe-by-lobe DIR and all FE methods.

Difference in voxel displacements predicted by lobe-by-lobe DIR and FE						
Subject	RLL	RML	RUL	LLL	LUL	Average
FE_0	4.7	6.6	5.4	6.1	5.6	5.57
$FE_{1.5}$	5.0	7.8	4.8	6.4	4.7	5.50
FE_{WL}	4.9	8.2	4.9	6.6	5.1	5.70

Figure 42 highlights sliding characteristics predicted by FE_0 by plotting contours of γ_{max} on coronal slices. These plots were made from FE_0 displacement data interpolated to the TLC voxel grid as described in the previous paragraph. Figure 42 illustrates that γ_{max} is significantly higher along the lobe fissures than throughout the parenchyma. Also, previously described trends for sliding in FRC-TLC subjects were observed in the FE_0 displacement field, see Section 2.2. These include highest sliding at the RML-RLL boundary and decreased sliding in medial and dorsal regions. Compare Figures 42 and 16 for similarities between FE_0 predicted sliding and lobe-by-lobe DIR measured sliding.

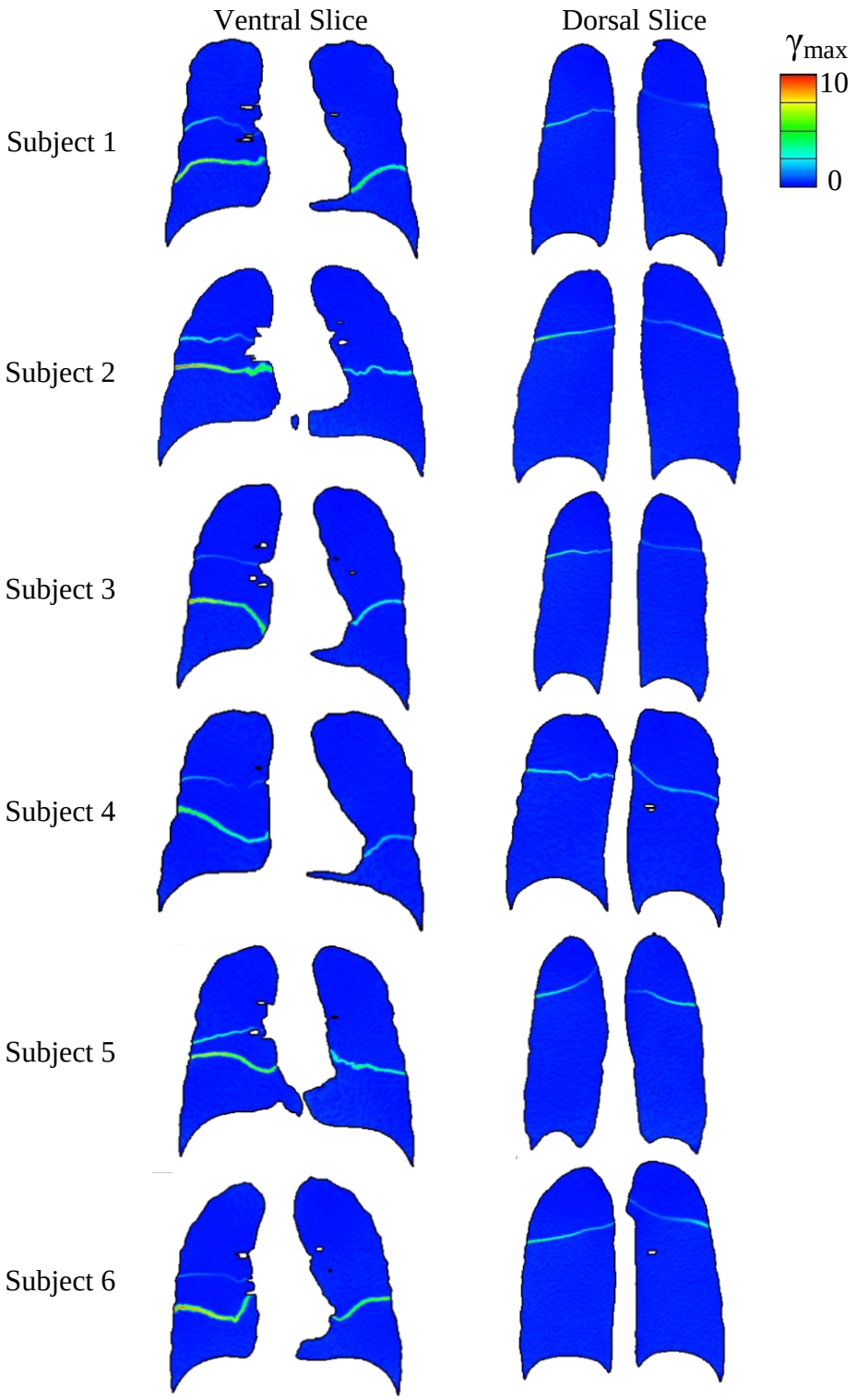

Figure 42: Contour slices for γ_{max} plotted on coronal slices. A slightly more ventral slices is in the left column and a slightly more dorsal slice is in the left column.

Average Jacobians, stratified by lobe, are compared between FE_0, $FE_{1.5}$ and lobe-by-lobe DIR in Figure 43. Since lobe-by-lobe DIR matches the FRC lobe segmentation to the TLC lobe segmentation with high accuracy, it can be considered the ground truth for average lobe Jacobian.

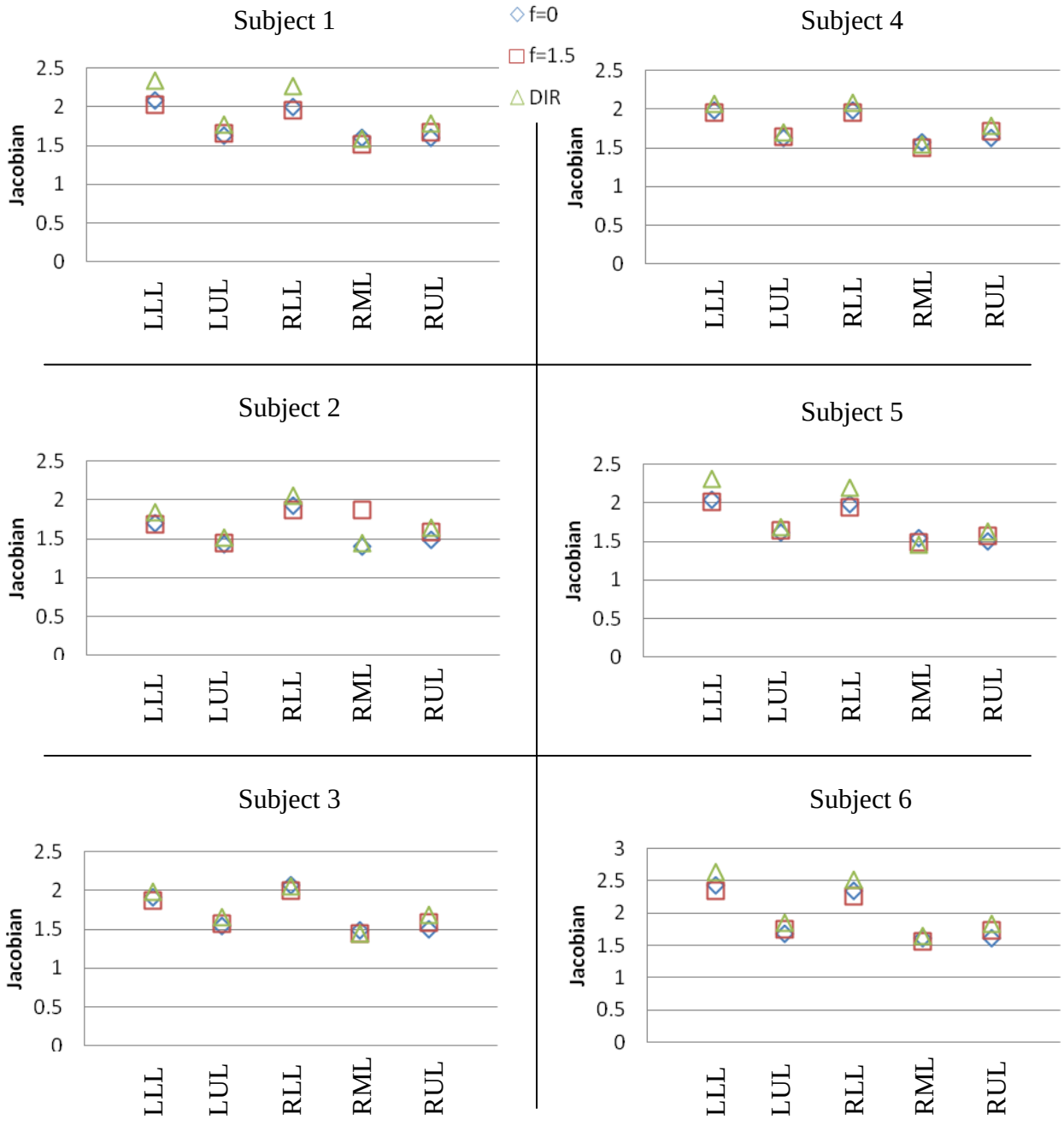

Figure 43: Average Jacobians, stratified by lobe, are plotted based on the measured segmentation Jacobian, the Jacobian predicted by FE_0 and the Jacobian predicted by $FE_{1.5}$.

4.3 Discussion of Displacement Field Accuracy

Image guided radiotherapy (IGRT) is the primary motivation for developing FE lung models. For this reason, recent publications involving patient specific FE lung models focus on displacement field accuracy assessed with landmark error. In Chapter 3 a novel patient specific FE lung model was developed that incorporated lung lobe sliding. The motivation was that continuum based models could not capture the discontinuity in the displacement field introduced by lung lobe sliding. However, no statistical difference in any landmark-based metrics was found between FE models with that allowed sliding and those that did not allow sliding. Qualitative assessment of the average landmark error suggested that inter-lobar frictional coefficients do not influence changes in landmark error. However, further qualitative and quantitative evaluation indicated that changing the frictional coefficient did alter the underlying displacement field; the changes simply did not affect landmark error.

The lack of landmark error improvement may be due to several reasons: 1) lobe sliding was poorly modeled, 2) landmark distribution did not sufficiently capture changes in the displacement field or 3) sliding was muted in tidal breathing due to relatively small deformation. The latter two limitations are addressed in this chapter by modeling FRC-TLC data sets and comparing the FE predicted displacement fields with lobe-by-lobe DIR displacement fields.

FRC-TLC data sets have much larger deformation which amplifies characteristics of deformation. The difference in deformation magnitude is illustrated in Figure 44. The average Jacobian for the FRC-TLC subjects in this chapter was 1.91 compared to an average Jacobian of 1.18 for the tidal breathing subjects in Chapter 3. In literature, lung lobe sliding measurements focus on FRC-TLC data sets where large magnitudes in deformation likely increase lobe sliding magnitude. The downside of modeling FRC-TLC data sets with finite elements is the larger deformation results in increased computational cost and increases the chance of element distortion resulting in non-converged solutions. Computation time increased to between 2 and 5 hours per FRC-TLC simulation (compare to 20 minutes to 2 hours for tidal breathing) when run

across 4-processors. The increased computation time was a consequence of several more steps and iterations per step required to obtain a converged solution.

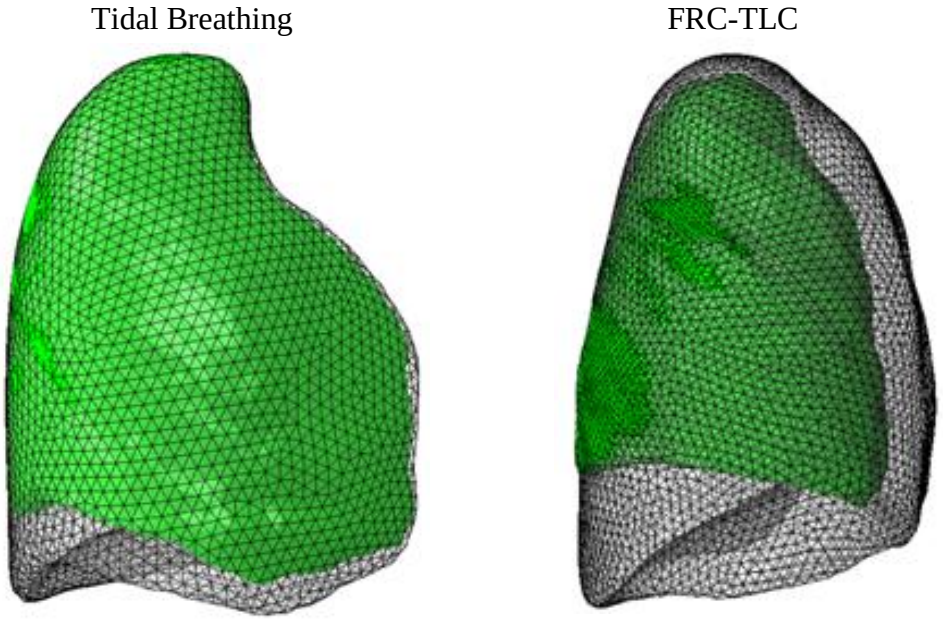

Figure 44: Initial (transparent grey) and final (green) pleural cavity geometries used as FE boundary conditions in Chapter 3 (left) and 4 (right). The magnitude of deformation in FRC-TLC data sets is much greater than tidal breathing.

4.3.1 Landmark Error Analysis

Prior to comparison with lobe-by-lobe DIR displacement fields, average landmark error was assessed; see Figures 40 and 41. Consistent with the results in Chapter 3, no statistical improvement in landmark error was found between FE_0 and $FE_{1.5}$. Statistically, $FE_{1.5}$ had lower average landmark error than FE_{WL} when averaged across all simulation sets, but the 0.19 mm average difference suggests improvement was minor and unimportant.

The average landmark errors in the FRC-TLC models were much higher than the tidal breathing models in Chapter 3 and those reported in literature. This is attributed to a significant increase in landmark displacements. Average landmark displacement in the FRC-TLC data sets

was 27.8 mm compared with 13.3 mm average landmark displacement in the tidal breathing data set in Chapter 3. To account for differences in landmark displacements, landmark error was normalized with observed landmark displacements to obtain 'landmark error improvement', LEI. Let $U_{n,LMK}$ be the picked landmark displacement vector and $U_{n,FE}$ be the FE predicted landmark displacement vector for the n^{th} landmark. LEI is given by the equation below.

$$LEI = 1 - \frac{\sum_{n=1}^{N} \left| U_{n,LMK} - U_{n,FE} \right|}{\sum_{n=1}^{N} \left| U_{n,LMK} \right|}$$

A value of LEI greater than 0 indicates the predicted final landmark location is closer to the picked final landmark location than the initial landmark location. In other words, the simulation moved the landmark closer to its actual final location than where it started. A value less than 0 indicates the predicted final landmark location is farther from the picked final landmark location than the initial landmark location. The maximum value for LEI is 1, indicating the predicted final landmark location and picked final landmark location was at the same point.

LEI for FE_0, $FE_{1.5}$ and FE_{WL} averaged over all simulation sets was 0.79. This means the FE predicted final landmark location is 79% closer to the picked final landmark position, relative to the initial landmark position. This compares favorably with LEI estimates from Chapter 3 (LEI between 0.54 and 0.69 within acceptable parameter ranges) as well as estimates from literature: Werner *et al.* (LEI = 0.50) [27] and Al-Mayah *et al.* (LEI = 0.20) (from [29] assuming a data set similar to their previous study in [11]).

4.3.2 Comparison of lung FE and lobe-by-lobe DIR

Landmarks may not be well distributed enough to capture the differences between FE_0 and $FE_{1.5}$. Therefore, FE results were compared to lobe-by-lobe DIR to investigate FE performance away from landmarks. Lobe-by-lobe DIR typically reports landmark errors under 1 mm. While lobe-by-lobe DIR accuracy may not be confirmed away from landmarks, for the

purpose of this comparison it is assumed that lobe-by-lobe DIR performs better than FE at all points and may be used as the gold standard for comparison.

FE_0, $FE_{1.5}$ and FE_{WL} were compared to the lobe-by-lobe displacement field. In order to make the comparison, the displacement vectors for all FE methods were interpolated to the TLC voxel grid using inverse distance interpolation. At a given voxel, the magnitude of the difference in the lobe-by-lobe DIR displacement vector and the FE displacement vector defines the error at the voxel. Errors are then averaged over the lobes and whole lung; results listed in Table 12.

The displacement field for FE_0 was more similar to that of DIR than $FE_{1.5}$ in the LLL, RLL and RML. FE_0 displacements were closer to lobe-by-lobe DIR displacements by 0.30 mm in the LLL, 0.33 mm in the RLL and 1.34 mm in the RML; the differences were not statistically significant. Conversely, the displacement field for FE_0 was less similar to that of lobe-by-lobe DIR than $FE_{1.5}$ in the LUL and RUL. $FE_{1.5}$ displacements were closer to lobe-by-lobe displacements by 0.93 mm in the LUL and 0.66 mm in the RUL. Again, these differences were not statistically significant.

The lack of statistical significance in the error improvement was not due to similarities in the FE_0 and $FE_{1.5}$ displacement fields. Landmark error and the comparison with lobe-by-lobe DIR stratified by lobe highlight regional differences in the displacement fields between FE_0 and $FE_{1.5}$. However, the regionally assessed error metrics do suggest $FE_{1.5}$ and FE_{WL} are similar. Furthermore, statistics indicate $FE_{1.5}$ may be systematically better than FE_{WL}. The lack of statistical improvement in the error metrics between FE_0 and $FE_{1.5}$ is therefore due to inconsistencies. Inconsistencies may arise in the subject population or in the influence of assumptions used by the FE model.

Population inconsistencies include all unaccounted for variations in the subject population. For instance, the lung material was modeled as a homogeneous, isotropic Neo Hookean material and all subjects were assigned the same material parameters. It is likely that variations material properties exist subject-to-subject, as well as lobe-to-lobe. For instance, in some subjects the RML may be stiffer than the RUL while the opposite is true in other subjects.

Inconsistent differences between actual material parameters and the homogeneous material parameters used in the study may lead to inconsistent errors in the displacement field. Also, lobe boundary conditions may vary across subjects. It is assumed that the mediastinum and carina loosely couple the lobes together. This coupling may play a larger role in governing lobe deformations in some subjects. A better handle on population inconsistencies may only be clarified with a large population study set.

Inconsistencies due to finite element model assumptions include errors in assumptions that lead to inconsistent results. For instance, the cavity in the lobe segmentation formed where the pulmonary artery and vein enter the lung was artificially filled in and assigned a lobe based on a filling algorithm. The procedure for cavity filling and lobe assignment was consistent across all subjects. However, the influence of cavity filling may affect some subjects more than others. Also, the pleural cavity was smoothed by the same smoothing protocols in all subjects. However, smoothing may influence the FE displacement fields more dramatically than others. Likewise, lobe segmentations and models were smoothed. While the smoothing protocol was consistent, the influence of lobe smoothing on the final displacement fields may not be consistent. A better handle on inconsistencies due to finite element modeling assumptions would require individual investigation of modeling assumptions and possibly a large subject population to rule out population inconsistencies. Consistent assumptions need not mean consistent consequences of the assumptions. Further investigation is warranted.

It is clear that at its current state FE_0 provides no improvement to displacement field accuracy when compared to $FE_{1.5}$ and FE_{WL}.

4.4 Discussion of FE Predicted Physiological Lung Phenomenon

Image guided radiotherapy (IGRT) is the primary motivation for the development of finite element lung models in recent years. For this reason, evaluation of the FE models is concerned solely around displacement field accuracy, be it regional or global accuracy measures. Limiting the role of FE analysis to displacement field accuracy (how the lung deforms) for use in

IGRT precludes contributions of FE to the field of lung research. Image-based analysis techniques will always overshadow physics-based models of lung displacement simply because all displacement field error metrics for *in-vivo* lungs are based on image information, thereby biasing accuracy towards image-based analysis. While image-based techniques are better at determining how the lung deforms, they cannot elucidate mechanisms of lung deformation. For instance, Xenon-CT and DIR both indicate a gravitational dependence in ventilation but cannot determine why the gravitational dependence exists. Finite element modeling serves as a platform to test hypotheses into why the lung deforms as it does. With regards to FE lung models, displacement field accuracy is important but only part of the solution. Equally important is the ability for the FE model to capture observed physiological phenomena. The remaining paper investigates the ability of the developed finite element models to accurately capture lung lobe sliding magnitude as well as regional variations in ventilation.

4.4.1 Lobe Sliding Predicted By FE_0

The lobes of the lung slide relative to each other during breathing. In Section 2.2, lung lobe sliding was measured from deformable image registration data using the metric γ_{max}, see Section 2.2 for a further background on lobe sliding in literature and for the definition of γ_{max}. A few consistent characteristics of lung sliding emerged. Namely, the most sliding consistently occurred at the boundary between the RML and the RLL and very little sliding occurred at the boundary between the RUL and the RML. Also, sliding increased away from the carina or mediastinum. The hypothesis is that the carina and/or mediastinum loosely couple the lobes which limit the amount of sliding in the medial and dorsal lung. The measureable amount of lobe sliding observed in Chapter 3 motivated the incorporation of lobe sliding into an FE lung model. Successful modeling of lobe sliding may shed light on the mechanism behind sliding.

Modeling assumptions are very important when interrogating FE models for physiological relevance. No coupling mechanism was modeled between the lobes except the inter-lobar frictional coefficient; neither the mediastinum nor carina was modeled. Material

property distribution was homogeneous and isotropic. No displacement or force boundary conditions were prescribed to any node on the lobe meshes; the lobe boundary conditions were completely governed by lobe-lobe and lobe-pleural cavity contact. With these assumptions in mind, the lobe displacements were resampled to the TLC voxel grid and sliding was parameterized with γ_{max}. Coronal slices, contoured with γ_{max}, are shown in Figure 42. First, notice that γ_{max} is much greater in the fissures than in the bulk tissue, indicating γ_{max} is dominated by lobe sliding as relatively little actual tissue shear existed in the FE model. The ventral slice contours illustrate the relative magnitude of sliding on the boundaries. The most sliding occurred at the boundary between the RML and RLL and the least amount of sliding is observed at the boundary between the RUL and RML and in the dorsal region of the LUL and LLL boundary. This is consistent with the trends in sliding observed from lobe-by-lobe DIR in Section 2.2. Qualitative assessment of the ventral and dorsal slices suggest slightly lesser sliding toward the medial lung than the lateral lung; both the carina and mediastinum are located medially. Figure 45 plots γ_{max} in a 3D perspective for Subject 2. This was accomplished by only showing voxel coordinates with $\gamma_{max} > 0.75$. Figure 45 further illustrates the trends observed in Figure 42. These plots illustrate that characteristics of sliding are reasonably captured by the FE_0 model. No sliding was observed in the $FE_{1.5}$ model, see Figure 46 for a sample coronal slice, contoured with γ_{max}.

The fact that lobe sliding was modeled using this FE paradigm with its assumptions has implications on the mechanisms of actual lobe sliding. Lobe sliding can be predicted from the mechanical interaction of the lobes and pleural cavity. Homogeneous material properties were used indicating heterogeneous material properties are not necessary for lobe sliding to occur. Airflow was not modeled indicating airflow distribution does not drive lobe sliding. The fact that a gradient in γ_{max} existed in the FE models, with lesser sliding near the carina, when no lobe coupling or boundary conditions to limit lobe sliding in this region was applied suggests the sliding gradient observed from CT scans in Section 2.2 and Ding et al. [4] may not be a result of lobe coupling at the carina. Instead, the gradient in sliding magnitude along the fissures was

modeled by considering solely lobe and pleural cavity initial geometries and pleural cavity deformation. Future studies involving lobe sliding finite element models should be pursued to further elucidate the mechanical contributors to lung lobe sliding.

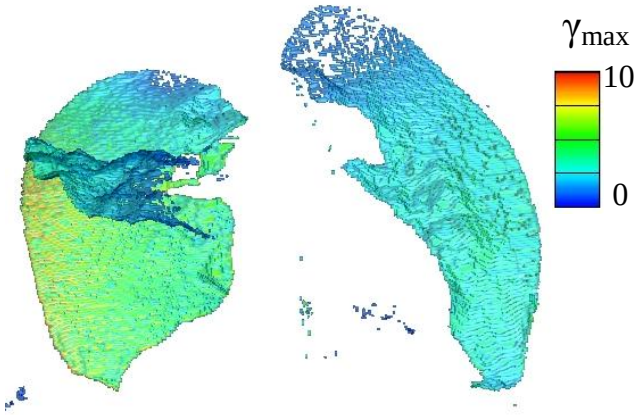

Figure 45: Sliding magnitude predicted by FE for Subject 1 shown on a 3D plot. This figure was obtained by eliminating all voxels in the volume that had a γ_{max} less than 0.75. A slight lateral to medial gradient in sliding is observed in the right lung.

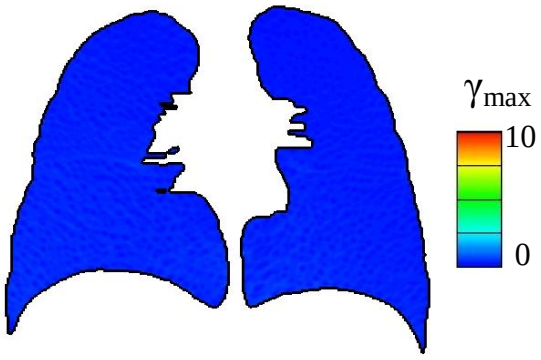

Figure 46: A contour slice showing γ_{max} plotted on a coronal slice for $FE_{1.5}$. This illustrates that $FE_{1.5}$ almost completely eliminated lobe sliding.

4.4.2 Regional Variations in Lung Ventilation Predicted by FE

Regional variations in lung ventilation have traditionally been associated with two factors: 1) gravity acting on the lung 2) pleural cavity shape change. There is a larger body of evidence supporting the gravitational theory as opposed to pleural cavity shape change.

Gravitational dependence, explained by West [1], operates on the assumption that regional lung elasticity follows a pressure volume curve similar to that of the whole lung, see Figure 1. In the range of FRC-TLC the lung becomes stiffer as the pressure increases. Gravity acts on lung tissue which increases the intrapleural pressure in the direction of gravity. The increase in intrapleural pressure is caused by the lung weight as the higher pressure is necessary to support the lung tissue above. In the context of negative pressure breathing, the intrapleural pressure at lower gravity is less negative. In the range of FRC-TLC lung volumes, the lower lung is always at a more compliant position on the pressure volume curve. West and Matthews explored the influence of lung weight on regional ventilation in an idealized lung [16]. Changes in pleural cavity shape were not considered and non-linear material properties were used to simulate decreased compliance at higher lung volumes. The study supported the theory of gravitational dependence in the idealized model. This paper was followed up by studying the influence of lung weight and pleural cavity shape change on regional stresses in an idealized finite element lung model [68]. The result of the follow-up study supported the notion that gravity was primarily responsible for regional distributions in lung stresses (volume change) and altering pleural cavity shape had relatively little effect.

The theory behind the influence of pleural cavity shape change on regional ventilation is simple. An isotropically deformed body may have uniform changes in volume (consider the reduction of volume of a body under hydrostatic pressure). However, the pleural cavity does not deform uniformly during breathing. During inhalation, the pleural cavity increases in height more than it increases in cross-sectional diameter as diaphragm displacement is much larger than the chest wall displacement. Vawter *et al.* investigated the role of this type of anisotropic deformation on an idealized lung model. It was determined that this type of anisotropic

deformation played an insignificant role in determining regional ventilation when compared with the influence of gravity [68]. Vawter investigated the influence of global anisotropic deformation by applying a uniform anisotropic deformation to the entire model and it should be noted that lung lobes were not modeled. However, regional anisotropic deformation of the pleural cavity also exists. During inhalation the diaphragm flattens which changes the shape of the inferior pleural cavity alone. Also, during inhalation the lung wraps further around the mediastinum [69] which changes the shape of the ventral pleural cavity alone. Local changes in pleural cavity shape may govern regional variations in ventilation. Companion papers by Margulies *et al.* [69] and Liu *et al.* [62] quantified chest wall shape changes in dog lungs between FRC and TLC and its influence on regional deformation, respectively. To determine the influence on regional ventilation, 2D transverse slices were considered. First, the TLC section was isotropically reduced to the corresponding FRC area. Finite element modeling deformed the shrunk TLC area to match the shape of the FRC area, yielding internal displacement fields and, consequently, an estimate of regional ventilation based on element area changes. Liu concluded that pleural cavity shape change substantially influence regional ventilation, however, the influence of gravity had to be incorporated to match observed regional ventilation in the prone position.

Amelon *et al.* demonstrated a consistent patterns in lobe averaged Jacobians in FRC-TLC human subjects in the supine position [35], see Section 2.1. As expected for supine human subjects, more volume change occurred in the lower lobes than the upper lobes. This follows the gravitational dependent theory as the lower lobes sit inferior and dorsal compared to the upper lobes and middle lobe. Average Jacobian values were calculated from the deformed FE_0 and $FE_{1.5}$ simulations on a lobe basis for comparison with this regional ventilation phenomenon. Figure 43 shows good agreement between trends in regional ventilation between measured lobe Jacobians and FE predicted lobe Jacobians. There is a difference in the magnitudes of lobe Jacobians between measured volume change, FE_0 and $FE_{1.5}$ which may be attributed to geometrical smoothing in the FE models and filling of the segmentation cavity where the pulmonary artery and vein enter the lung, Figure 22. However, differences in lobe Jacobians

between upper and lower lobes quantify the degree of variation in regional ventilation. Volume change in the upper lobes was significantly higher than the corresponding lower lobes for measured volume change, FE_0 and $FE_{1.5}$ ($p<0.001$). On average, measured volume change indicated a 68% percent increase in volume change in a given lower lobe compared to its corresponding upper lobe. On average, FE_0 predicted percent volume change in the lower lobes was 81% greater than the upper lobes while $FE_{1.5}$ predicted a 57% difference in percent volume change. Variation in lobe Jacobians between upper and lower lobes were significantly lower in $FE_{1.5}$ when compared with FE_0 ($p<0.05$) and measured volume change ($p<0.05$). Variation in lobe volume changes between upper and lower lobes was not statistically different between FE_0 and measured volume change ($p=0.057$). FE_0 overestimated the variation in regional ventilation while $FE_{1.5}$ underestimated the variation in regional ventilation. Using regional ventilation as a performance measure suggests the frictional coefficient should have been somewhere between 0 and 1.5.

It must be noted that regional variations in ventilation was found in both FE models without modeling gravity or incorporating lobe weight in any manner. The simulations were also run as quasi-static which prevents effects due to inertia. Homogenous material properties with stiffness nearly independent of strain were used. The results indicate overwhelming evidence that pleural cavity geometry shape change does account for significant regional variations in ventilation. Furthermore, lobe sliding amplified the degree of predicted variation in regional ventilation. We can definitively conclude that the combination of pleural cavity shape change, lobe geometry, and lobe sliding cause significant regional variations in ventilation independent of the inclusion of gravity.

4.5 Conclusion

Limiting success of FE based solely on displacement field accuracy is not prudent use of finite element modeling. Sliding magnitude was quantified from lobe sliding FE models and compared favorably with sliding measured from deformable image registration. Models that

prohibited sliding could not capture the discontinuity in the displacement field. This indicates that the FE_0 more accurately captured the characteristics of lung lobe sliding. Additionally, regional ventilation was quantified and compared at the lobe level between lobe sliding FE, FE prohibiting lobe sliding, and regional volume change measured from CT scans. The variation in lobe ventilation measured from CT scans was substantial and remarkably consistent across subjects. FE_0 overestimated the variation in lobe ventilation while $FE_{1.5}$ underestimated the variation in lobe ventilation. This indicates that lung lobe sliding does influence variations in lobe ventilation. While landmark error cannot distinguish differences between the models, the physiological interpretations are vastly different. Lung FE models should be pursued in the future to help shed light on the mechanisms behind lung deformation.

APPENDIX A: MANUAL LOBE SEGMENTATION PROCESS

The following outlines the steps for manual segmentation of single lobe using Slicer4. Manual segmentation is the masking of the entire lobe where care is taken to accurately segment the fissure. Accuracy on the pleural cavity – lobe boundaries is unimportant as long as the entire lobe is contained within the segmentation. The process is conducted for the right upper lobe, right lower lobe, and left upper lobe.

1. Quickly scan saggittal and coronal views to find in which view the fissures are most distinguishable. Pay particular attention to the right horizontal fissure as this is often the most difficult to identify.
    i. Once the best view is selected (call ViewA), switch to the view not chosen (call ViewB). Identify 6-8 slices, roughly evenly spaced and spanning a large majority of the volume, where confident segmentation may occur. Segment the lobe on these slices.
    ii. Switch back to ViewA. The segmentation in ViewB will appear as a guide for segmenting in ViewA. Segment slice-by-slice in ViewA while confident in fissure segmentation accuracy.
    iii. For all remaining slices in ViewA, where confident segmentation cannot occur, revert back to ViewB. Select slices in ViewB where the segmentation will appear in the un-segmented slices of ViewA. If the fissure cannot be identified, use ViewA as a guide for segmentation and visually interpolate the boundary when necessary. Often, enough of ViewA will be segmented such that segmentation in ViewB is trivial.
    iv. Switch back to ViewA and continue segmenting. Continue to switch between ViewA and ViewB until all slices in ViewA are segmented.

b. Post-processing manual lobe segmentation
    i. These steps occur after the RUL, RLL and LLL have been segmented.
    ii. Subtract the RUL, RLL and LLL from the whole lung mask. Perform two simple region grows in the right and left lungs to obtain the RML and LUL, respectively.
    iii. The masks will be very noisy in ViewB. To remove the noise, perform the following protocol on each lung lobe (five total). Dilate one voxel, erode 2 voxels, dilate 1 voxel.
    iv. Renumber the lobe mask ID according to the following convention: RLL=1, RUL=2, RML=3, LLL=4, LUL=5. Combine the lobe masks into a single image using ‘image label combine’ within Slicer. If there is overlap between individual lobe masks then assign based on the following priority (RML, RUL, RLL, LUL, LLL). This priority is based roughly on lobe size, small to large.

v. There will be voxels occupied by the whole lung mask that are not occupied by the complete lobe mask. To fix this, the following pseudo-code is used to fill the unclaimed voxels, programmed in Matlab.
    1. Cycle through all voxels within the whole lung mask that are not claimed by any lobe.
    2. Look at the neighboring 6 voxels. If one lobe occupies more of the neighbors than any other lobe then that voxel is assigned to the corresponding lobe. If there is a tie, then leave the voxel unclaimed. If no neighbors are claimed by lobes then leave voxel unclaimed.
    3. Continue to cycle through all unclaimed voxels until no change is made for a given iteration.
    4. Cycle through the remaining unclaimed voxels an additional time. This time, if there is a tie then assign based on the following priority (RML, RUL, RLL, LUL, LLL). Repeat until no unclaimed voxels exist.

APPENDIX B: MESH CONSTRUCTION FROM IMAGE SEGMENTATION

Each lung half will be simulated separately. Therefore, the mesh construction protocol was repeated separately for the left and right lungs. To obtain all meshes required for a complete lung (both halves) 7 independent bodies must be meshed corresponding to the right pleural cavity (RPC), the left pleural cavity (LPC), and the five lobe meshes. Mimics was used to construct surface models from the image masks. The surface models were then meshed in Gambit. The following lays out the steps to go from an image mask to an acceptable finite element mesh.

To simplify the process within Mimics, and to reduce memory usage, only one lung half is loaded at a time. The following process is described for the right lung. The process is identical with the left lung, but with one fewer lobes.

1. Load the image mask into Mimics. Since each lobe has a different value, threshold to obtain a mask for the RUL, RML, RLL and entire right lung. The entire right lung mask will herein be referred to as the right pleural cavity (RPC) mask.
2. For each lobe, use the open operation with size of 1 voxel (26-connectivity). Confine the open operation to the RPC mask.
3. Create a 3D surface model of each lobe. Enter the Remesh Module.
4. Remeshing occurs in several steps. During remeshing, set the element quality to a low value (0.2) and set the geometrical approximation to 0.3.
    vi. Smoothing process for the RPC
        1. Remesh to max element size of 6.
        2. Smooth with Lagrangian smoothing (non-shrinking), 20 iterations.
        3. Remesh to max element size of 6.
        4. Smooth with Lagrangian smoothing (non-shrinking), 20 iterations.
        5. Remesh to max element size of 6.
        6. Smooth with Lagrangian smoothing, 3 iterations.
        7. Remesh to max element size of 12.
        8. Smooth with Lagrangian smoothing (non-shrinking), 20 iterations.
    vii. Smoothing process for individual lobes
        1. Remesh to max element size of 3.
        2. Smooth with Lagrangian smoothing (non-shrinking), 20 iterations.
        3. Remesh to max element size of 6.
        4. Smooth with Lagrangian smoothing (non-shrinking), 20 iterations.
        5. Remesh to max element size of 6.
        6. Smooth with Lagrangian smoothing, 3 iterations.
        7. Remesh to max element size of 12.
        8. Smooth with Lagrangian smoothing (non-shrinking), 20 iterations.

1. Exit the Remesh Module. The lobes will now be overlapping from smoothing; gaps between lobes may also exist. The following procedure helps to minimize the overlap and fill gaps.
    c. Create a 3D mask from all the remeshed surface models.
    d. This following procedure is conducted on each lobe in the following order (RML, RUL, RLL)
    e. Dilate the mask 1 voxel (dilation confined to RPC mask)
    f. Subtract each other mask from the newly dilated mask
    g. Repeat steps e-f for 3 total iterations. On the fourth iteration dilate 2 voxels instead of one. This helps ensure the lobes collectively occupy a similar volume as the RPC. Then, conduct a region grow on each lobe to ensure there are no stray points.
2. Create 3D models of the RPC, RLL, RUL and RML.
3. Remesh the RPC, RLL, RUL and RML by entering the Remesh Module. Smoothing at this stage is necessary to remove voxelation, but also helps obtain a slightly smoother geometry.
    h. For the RPC
        i. Remesh to max element size of 6.
        ii. Smooth with Lagrangian smoothing (non-shrinking), 20 iterations.
        iii. Remesh to max element size of 6.
        iv. Smooth with Lagrangian smoothing (non-shrinking), 20 iterations.
        v. Remesh to max element size of 6.
        vi. Smooth with Lagrangian smoothing, 3 iterations.
    i. For each lobe model
        i. Remesh to max element size of 3.
        ii. Smooth with Lagrangian smoothing (non-shrinking), 20 iterations.
        iii. Remesh to max element size of 6.
        iv. Smooth with Lagrangian smoothing (non-shrinking), 20 iterations.
        v. Remesh to max element size of 6.
        vi. Smooth with Lagrangian smoothing, 3 iterations.
4. Exit the Remesh Module and export the remeshed RPC, RLL, RUL and RML surface models in *.stl format.
    a. Load the *.stl surface models into Gambit
    b. For the RPC
        i. Remesh the surface using triangles of element size 6
    c. For each lobe
        i. Create a virtual volume by stitching the mesh faces. There should only be 1 face. If multiple faces exist then there was a problem in the surface model
        ii. Mesh the surface using triangles of size 6.
        iii. Mesh the virtual volume using tetrahedrals of element size 6.
    d. Export all meshes.

REFERENCES

1. West, J.B., *Respiratory physiology : the essentials*. 8th ed. 2007, Philadelphia: Lippincott Williams & Wilkins. p.

2. Wiener-Kronish, J.P., M.A. Gropper, and S.J. Lai-Fook, *Pleural liquid pressure in dogs measured using a rib capsule.* J Appl Physiol, 1985. **59**(2): p. 597-602.

3. Lai-Fook, S.J., D.C. Price, and N.C. Staub, *Liquid thickness vs. vertical pressure gradient in a model of the pleural space.* J Appl Physiol, 1987. **62**(4): p. 1747-54.

4. Ding, K., et al., *Evaluation of lobar biomechanics during respiration using image registration.* Med Image Comput Comput Assist Interv, 2009. **12**(Pt 1): p. 739-46.

5. Cai, J., et al., *Direct measurement of lung motion using hyperpolarized helium-3 MR tagging.* Int J Radiat Oncol Biol Phys, 2007. **68**(3): p. 650-3.

6. Lai-Fook, S.J., et al., *Elastic constants of inflated lobes of dog lungs.* J Appl Physiol, 1976. **40**(4): p. 508-13.

7. Lai-Fook, S.J., R.E. Hyatt, and J.R. Rodarte, *Elastic constants of trapped lung parenchyma.* J Appl Physiol, 1978. **44**(6): p. 853-8.

8. Debes, J.C. and Y.C. Fung, *Effect of temperature on the biaxial mechanics of excised lung parenchyma of the dog.* J Appl Physiol, 1992. **73**(3): p. 1171-80.

9. Salerno, F.G., P. Pare, and M.S. Ludwig, *A comparative study of elastic properties of rat and guinea pig parenchymal strips.* Am J Respir Crit Care Med, 1998. **157**(3 Pt 1): p. 846-52.

10. Zeng, Y.J., D. Yager, and Y.C. Fung, *Measurement of the mechanical properties of the human lung tissue.* J Biomech Eng, 1987. **109**(2): p. 169-74.

11. Al-Mayah, A., J. Moseley, and K.K. Brock, *Contact surface and material nonlinearity modeling of human lungs.* Phys Med Biol, 2008. **53**(1): p. 305-17.

12. Brock, K.K., et al., *Accuracy of finite element model-based multi-organ deformable image registration.* Med Phys, 2005. **32**(6): p. 1647-59.

13. De Wilde, R., et al., *Model of elasticity of the human lung.* J Appl Physiol, 1981. **51**(2): p. 254-61.

14. Sundaram, T.A. and J.C. Gee, *Towards a model of lung biomechanics: pulmonary kinematics via registration of serial lung images.* Med Image Anal, 2005. **9**(6): p. 524-37.

15. Villard, P.F., et al. *Simulation of lung behaviour with finite elements: influence of bio-mechanical parameters*. in *Medical Information Visualisation - Biomedical Visualisation, 2005. (MediVis 2005). Proceedings. Third International COnference on*. 2005.

16. West, J.B. and F.L. Matthews, *Stresses, strains, and surface pressures in the lung caused by its weight.* J Appl Physiol, 1972. **32**(3): p. 332-45.

17. Zhang, T., et al., *Technical note: A novel boundary condition using contact elements for finite element based deformable image registration.* Med Phys, 2004. **31**(9): p. 2412-5.

18. Naini, A.S., R.V. Patel, and A. Samani, *Measurement of Lung Hyperelastic Properties Using Inverse Finite Element Approach.* Biomedical Engineering, IEEE Transactions on, 2011. **58**(10): p. 2852-2859.

19. Schwenninger, D., S. Schumann, and J. Guttmann, *In vivo characterization of mechanical tissue properties of internal organs using endoscopic microscopy and inverse finite element analysis.* J Biomech, 2011. **44**(3): p. 487-93.

20. Cai, J., et al., *Dynamic MRI of Grid-Tagged Hyperpolarized Helium-3 for the Assessment of Lung Motion During Breathing.* Int J Radiat Oncol Biol Phys, 2009.

21. Napadow, V.J., et al., *Determination of regional pulmonary parenchymal strain during normal respiration using spin inversion tagged magnetization MRI.* J Magn Reson Imaging, 2001. **13**(3): p. 467-74.

22. Fain, S.B., et al., *Functional lung imaging using hyperpolarized gas MRI.* J Magn Reson Imaging, 2007. **25**(5): p. 910-23.

23. Yin, Y., E.A. Hoffman, and C.L. Lin, *Mass preserving nonrigid registration of CT lung images using cubic B-spline.* Med Phys, 2009. **36**(9): p. 4213-22.

24. Brock, K.K., *Results of a multi-institution deformable registration accuracy study (MIDRAS).* Int J Radiat Oncol Biol Phys, 2010. **76**(2): p. 583-96.

25. Cao, K., et al. *Tissue volume and vesselness measure preserving nonrigid registration of lung CT images*. 2010: SPIE.

26. Yin, Y., E.A. Hoffman, and C.L. Lin, *Lung lobar slippage assessed with the aid of image registration.* Med Image Comput Comput Assist Interv, 2010. **13**(Pt 2): p. 578-85.

27. Werner, R., et al., *Patient-specific finite element modeling of respiratory lung motion using 4D CT image data.* Med Phys, 2009. **36**(5): p. 1500-11.

28. Al-Mayah, A., et al., *Sliding characteristic and material compressibility of human lung: Parametric study and verification.* Medical Physics, 2009. **36**(10): p. 4625-4633.

29. Al-Mayah, A., et al., *Toward efficient biomechanical-based deformable image registration of lungs for image-guided radiotherapy.* Phys Med Biol, 2011. **56**(15): p. 4701-13.

30. Chhatkuli, S., S. Koshizuka, and M. Uesaka, *Dynamic Tracking of Lung Deformation during Breathing by Using Particle Method.* Modelling and Simulation in Engineering, 2009. **2009**.

31. Modat M, M.J.a.O.S., *Lung registration using the NiftyReg package*, in *Medical Image Analysis for the Clinic: A Grand Challenge, Workshop Proc. from MICCAI 2010* 2010. p. 33-42.

32. Rietzel, E. and G.T.Y. Chen, *Deformable registration of 4D computed tomography data.* Medical Physics, 2006. **33**(11): p. 4423-4430.

33. Wu, Z., et al., *Evaluation of deformable registration of patient lung 4DCT with subanatomical region segmentations.* Med Phys, 2008. **35**(2): p. 775-81.

34. Keall, P.J., et al., *The management of respiratory motion in radiation oncology report of AAPM Task Group 76*. Vol. 33. 2006: AAPM. 3874-3900.

35. Amelon, R., et al., *Three-dimensional characterization of regional lung deformation.* J Biomech, 2011. **44**(13): p. 2489-95.

36. Olson, L.E. and J.R. Rodarte, *Regional differences in expansion in excised dog lung lobes.* J Appl Physiol, 1984. **57**(6): p. 1710-4.

37. Reinhardt, J.M., et al., *Registration-based estimates of local lung tissue expansion compared to xenon CT measures of specific ventilation.* Med Image Anal, 2008. **12**(6): p. 752-63.

38. Rodarte, J.R., et al., *Regional lung strain in dogs during deflation from total lung capacity.* J Appl Physiol, 1985. **58**(1): p. 164-72.

39. van Beek, E.J. and E.A. Hoffman, *Functional imaging: CT and MRI.* Clin Chest Med, 2008. **29**(1): p. 195-216, vii.

40. Reinhardt, J.M., et al., *Registration-derived estimates of local lung expansion as surrogates for regional ventilation.* Inf Process Med Imaging, 2007. **20**: p. 763-74.

41. Keall, P.J., et al., *Four-dimensional radiotherapy planning for DMLC-based respiratory motion tracking.* Med Phys, 2005. **32**(4): p. 942-51.

42. Zingg, T., *Beitrag zur Schotteranalyse.* Schweizerische Mineralogische und Petrologische Mitteilungen, 1935. **15**: p. 39-140.

43. Flinn, D., *On the Deformation of the Funzie Conglomerate, Fetlar, Shetland.* Journal of Geology, 1956. **64**(5): p. 480-505.

44. Flinn, D., *On folding during three-dimensional progressive deformation.* Quarterly Journal of the Geological Society, 1962. **118**(1-4): p. 385-428.

45. Hu, S., E.A. Hoffman, and J.M. Reinhardt, *Automatic lung segmentation for accurate quantitation of volumetric X-ray CT images.* IEEE Trans Med Imaging, 2001. **20**(6): p. 490-8.

46. Ukil, S. and J.M. Reinhardt, *Anatomy-guided lung lobe segmentation in X-ray CT images.* IEEE Trans Med Imaging, 2009. **28**(2): p. 202-14.

47. Masutani, Y., H. MacMahon, and K. Doi, *Automated segmentation and visualization of the pulmonary vascular tree in spiral CT angiography: an anatomy-oriented approach based on three-dimensional image analysis.* J Comput Assist Tomogr, 2001. **25**(4): p. 587-97.

48. Quinn, D.A., et al., *Interactions of lung stretch, hyperoxia, and MIP-2 production in ventilator-induced lung injury.* J Appl Physiol, 2002. **93**(2): p. 517-25.

49. Matthay, M.A., et al., *Ventilator-induced lung injury: in vivo and in vitro mechanisms.* Am J Physiol Lung Cell Mol Physiol, 2002. **283**(4): p. L678-82.

50. Bailey, T.C., et al., *High oxygen concentrations predispose mouse lungs to the deleterious effects of high stretch ventilation.* J Appl Physiol, 2003. **94**(3): p. 975-82.

51. Chu, E.K., T. Whitehead, and A.S. Slutsky, *Effects of cyclic opening and closing at low- and high-volume ventilation on bronchoalveolar lavage cytokines.* Crit Care Med, 2004. **32**(1): p. 168-74.

52. Simon, B.A., *Regional ventilation and lung mechanics using X-Ray CT.* Acad Radiol, 2005. **12**(11): p. 1414-22.

53. Marcucci, C., D. Nyhan, and B.A. Simon, *Distribution of pulmonary ventilation using Xe-enhanced computed tomography in prone and supine dogs.* J Appl Physiol, 2001. **90**(2): p. 421-30.

54. Ding, K., *Registration-based regional lung mechanical analysis.* Master's thesis, University of Iowa, 2008.

55. Amelon, R., et al. *Estimation of lung lobar sliding using image registration*. 2012: SPIE.

56. Hubmayr, R.D., et al., *Regional ventilation during spontaneous breathing and mechanical ventilation in dogs.* J Appl Physiol, 1987. **63**(6): p. 2467-75.

57. Cao, K., et al., *Unifying Vascular Information in Intensity-Based Nonrigid Lung CT Registration Biomedical Image Registration*, B. Fischer, B. Dawant, and C. Lorenz, Editors. 2010, Springer Berlin / Heidelberg. p. 1-12.

58. Sheng, K. and J. Cai. *TH-C-AUD C-01: Lung Mechanical Modeling Based On the 3He MR Tagging and Lobar Segmentation*. 2008: AAPM.

59. Du, K., et al., *Reproducibility of registration-based measures of lung tissue expansion.* Medical Physics, 2012. **39**(3): p. 1595-1608.

60. *Abaqus User Manual - version 6.11*. 2011.

61. Murphy, K., et al., *Semi-automatic construction of reference standards for evaluation of image registration.* Medical Image Analysis, 2011. **15**(1): p. 71-84.

62. Liu, S., S.S. Margulies, and T.A. Wilson, *Deformation of the dog lung in the chest wall.* J Appl Physiol, 1990. **68**(5): p. 1979-87.

63. Guerrero, T., et al., *Quantification of regional ventilation from treatment planning CT.* Int J Radiat Oncol Biol Phys, 2005. **62**(3): p. 630-4.

64. Christensen, G.E., et al., *Tracking lung tissue motion and expansion/compression with inverse consistent image registration and spirometry.* Med Phys, 2007. **34**(6): p. 2155-63.

65. Al-Mayah, A., et al., *Deformable image registration of heterogeneous human lung incorporating the bronchial tree.* Med Phys, 2010. **37**(9): p. 4560-71.

66. Eom, J., et al., *Modeling respiratory motion for cancer radiation therapy based on patient-specific 4DCT data.* Med Image Comput Comput Assist Interv, 2009. **12**(Pt 2): p. 348-55.

67. Werner, R., et al. *Validation and comparison of a biophysical modeling approach and non-linear registration for estimation of lung motion fields in thoracic 4D CT data*. 2009: SPIE.

68. Vawter, D.L., F.L. Matthews, and J.B. West, *Effect of shape and size of lung and chest wall on stresses in the lung.* J Appl Physiol, 1975. **39**(1): p. 9-17.

69. Margulies, S.S. and J.R. Rodarte, *Shape of the chest wall in the prone and supine anesthetized dog.* J Appl Physiol, 1990. **68**(5): p. 1970-8.